

PRIMARY INSTABILITY AND
SUBSEQUENT DYNAMICS OF LIQUID
FILM FLOW ALONG PERIODIC
CORRUGATIONS



Zhehui Cao

Department of Mechanical Engineering

University of Thessaly

A thesis submitted for the degree of

Doctor of Philosophy

January 2013

Members of examination committee

Professor V. Bontozoglou (Supervisor)

Department of Mechanical Engineering, University of Thessaly

Associate Professor N. Andritsos (Members of Advisory Committee)

Department of Mechanical Engineering, University of Thessaly

Professor M. Vlachogiannis (Members of Advisory Committee)

Department of Mechanical Engineering, TEI Larissa

Associate Professor A. Papathanasiou

Department of Mechanical Engineering, University of Thessaly

Professor A. Stamatelos

Department of Mechanical Engineering, University of Thessaly

Associate Professor A. Stamatis

Department of Mechanical Engineering, University of Thessaly

Associate Professor Th. Panidis

Department of Mechanical Engineering and Aeronautics, University
of Patras

I would like to dedicate this thesis to my wife, Xiaolei, and my parents, Qun and Aiqing, for their unconditional support.

Acknowledgements

First and foremost, I would like to express my heartfelt gratitude to my supervisor, Prof. V. Bontozoglou, not only for his patient guidance and constant supports on the project, but also his perpetually enthusiastic attitude towards research and life which encouraged me a lot. I would also like to thank Prof. M. Vlachogiannis (in TEI Larissa) and Prof. Andritsos for all their help and advise on the experiments. Without their support, the experiments would not have been successful.

I wish to take the opportunity to express appreciation to two secretaries in the department, Nicoletta and Zoe, for their abundant help in dealing with the administrative issue with the university and Greek public sectors. My sincere thanks to Anna, who kept me accompanied in the lab and also provided plenty of advise of living in Greece. I would also like to thank Khanh and Judith for their help during the time in Volos. Without their help, the life in Greece would not be so comfortable and colourful.

I gratefully acknowledge the financial support of the EU-FP7- Marie-Curie Initial Training Network “MULTIFLOW” (GA no :214919-2), which give me opportunity to participate a number of scientific trainings, workshops, conferences and collaborations. Thanks to the network, I met many good friends and had very fruitful discussions. I would like to convey my thanks to Prof. A. Oron in Technion to provide me his code to perform numerical simulations.

Last but not least, I would like to express my gratitude to my parents for their support and encouragement during the study. Finally, I would like to thank my wife Xiaolei, for her understanding and patience. Without her support, this thesis would never have turned into reality.

Abstract

This work is an experimental study of gravity-driven liquid film flow along corrugated substrates. Thin liquid films appear in important industrial, environmental and biomedical flows. The modifications, resulting from the substitution of the flat substrate on which the film flows by one with topography, are presently not well understood. In particular, there is little experimental evidence about the effect of periodic corrugations on the primary instability of the flow, and the relevant theoretical predictions appears contradictory. This problem is of significant interest, because of the potential for instability control in such flows through the development of appropriately tailored substrates.

Systematic experiments were performed with water-glycerol solutions, in two flow facilities spanning a wide range of inclination angles. Substrates with different shapes (sinusoidal and rectangular) and various wavelengths and amplitudes were examined. The temporal variation of liquid film thickness was measured by conductance probes at multiple locations along the flow. A photographic technique was developed to record the spatial variation of the free surface in the streamwise direction. Using these techniques, the primary instability threshold was reliably determined, and the characteristics of traveling waves in the unstable regime were recorded.

A major finding of the thesis is that, for intermediate and high inclinations, steep enough corrugations trigger a new instability mode

of finite wavelength, while they delay significantly the occurrence of the classical, convective, long-wave instability. The new mode is a short, traveling wave, which is highly regular and persistently two-dimensional, and appears to be a global mode. Transition from long- to short-wave instability is observed to occur with increasing inclination angle, and the exact location of the transition varies with the corrugation shape. The parametric effects of liquid viscosity and of corrugation wavelength and amplitude are examined, and the important special case of a vertical wall is investigated using a cylindrical flow geometry. Finally, an unexpected oscillatory instability is documented, specific to steep, rectangular substrates, which appears and intensifies when decreasing the liquid flow rate. It is speculated that this counter-intuitive behaviour is related to the specific separation characteristics of the rectangular substrate, and is triggered when the backflow velocity exceeds a percentage of the forward stream.

ΠΡΩΤΟΓΕΝΗΣ ΑΣΤΑΘΕΙΑ ΚΑΙ ΚΑΤΑΝΤΗ ΔΥΝΑΜΙΚΗ ΤΗΣ
ΡΟΗΣ ΥΓΡΟΥ ΥΜΕΝΑ ΣΕ ΠΕΡΙΟΔΙΚΑ ΔΙΑΜΟΡΦΩΜΕΝΟ
ΥΠΟΣΤΡΩΜΑ

ZHENHUI CAO

Πανεπιστήμιο Θεσσαλίας, Τμήμα Μηχανολόγων Μηχανικών, 2013

Επιβλέπων Καθηγητής : Δρ. Μποντόζογλου Βασίλειος, Καθηγητής

ΠΕΡΙΛΗΨΗ

Η παρούσα εργασία είναι μία πειραματική μελέτη της βαρυτικής ροής υγρού υμένα πάνω σε υπόστρωμα με περιοδική διαμόρφωση. Λεπτοί, υγροί υμένες εμφανίζονται σε σημαντικές βιομηχανικές, περιβαλλοντικές και βιο-ιατρικές ροές. Οι διαφοροποιήσεις που προκαλούνται στη ροή από την αντικατάσταση του επίπεδου υποστρώματος από άλλο με τοπογραφία, δεν είναι σήμερα πλήρως κατανοητές. Ιδιαίτερα, υπάρχουν λίγες πειραματικές μελέτες σχετικά με την επίδραση περιοδικής διαμόρφωσης στην πρωτογενή αστάθεια της ροής, και οι σχετικές θεωρητικές προβλέψεις εμφανίζονται αντιφατικές. Το πρόβλημα αυτό έχει αξιόλογο ενδιαφέρον, λόγω της δυνατότητας ελέγχου της αστάθειας αυτών των ροών με την ανάπτυξη κατάλληλα διαμορφωμένων υποστρωμάτων.

Στην εργασία εκπονήθηκαν συστηματικά πειράματα, χρησιμοποιώντας ως υγρό διαλύματα νερού-γλυκερίνης, σε δύο διατάξεις ροής και για μεγάλο εύρος κλίσεων του υποστρώματος. Εξετάστηκαν ημιτονοειδείς και ορθογωνικές διαμορφώσεις, με διάφορα μήκη κύματος και πλάτη διαταραχής. Μετρήθηκε με αγωγιμομετρικούς αισθητήρες, και σε διάφορες θέσεις κατά μήκος της ροής, η χρονική μεταβολή του στιγμιαίου πάχους υγρού υμένα. Αναπτύχθηκε επίσης μία φωτογραφική τεχνική που καταγράφει την χωρική διακύμανση της θέσης της ελεύθερης επιφάνειας στη

διεύθυνση ροής. Χρησιμοποιώντας τις τεχνικές αυτές, εντοπίστηκε το όριο πρωτογενούς αστάθειας και καταγράφηκαν τα χαρακτηριστικά των οδευόντων κυμάτων στην ασταθή περιοχή.

Ένα κύριο εύρημα της εργασίας είναι, ότι, σε μεσαίες και υψηλές κλίσεις, η διαμόρφωση του τοιχώματος διεγείρει έναν νέο τύπο αστάθειας πεπερασμένου μήκους κύματος, ενώ ταυτόχρονα καθυστερεί σημαντικά την ανάπτυξη της κλασσικής, συναγωγικής αστάθειας άπειρου μήκους κύματος. Ο νέος τύπος αστάθειας συνίσταται από σχετικά μικρού μήκους οδύοντα κύματα, με υψηλή κανονικότητα και διδιάστατη δομή, και εμφανίζεται ως ιδιομορφή που επηρεάζεται από τη ροή συνολικά, και όχι από τα τοπικά χαρακτηριστικά της (global mode). Με αύξηση της γωνίας κλίσης του καναλιού, παρατηρείται μετάπτωση από τον κλασσικό στον νέο τύπο αστάθειας, και οι ακριβείς συνθήκες μετάπτωσης εξαρτώνται από το σχήμα της διαμόρφωσης. Εξετάστηκαν επίσης η επίδραση του ιξώδους του υγρού, του μήκους κύματος και του ύψους του περιοδικού τοιχώματος. Η ιδιαίτερης σημασίας περίπτωση του κάθετου τοιχώματος, μελετήθηκε με ξεχωριστά πειράματα ροής υγρού υμένα στην εξωτερική επιφάνεια ενός κυλίνδρου. Τέλος, εντοπίστηκε μία απρόβλεπτη ταλαντωτική αστάθεια, η οποία εμφανίζεται ειδικά σε ορθογωνική διαμόρφωση και υψηλές κλίσεις υποστρώματος, και η οποία ισχυροποιείται με μείωση της παροχής υγρού. Πιθανολογείται ότι η συμπεριφορά αυτή σχετίζεται με τα χαρακτηριστικά της αποκόλλησης της ροής στην ορθογωνική γεωμετρία, και εμφανίζεται όταν -με την μείωση της παροχής υγρού- η ταχύτητα ανακυκλοφορίας γίνεται σημαντικό κλάσμα της ταχύτητας στη διεύθυνση ροής.

Contents

Contents	ix
List of Figures	xii
Nomenclature	xxii
1 Introduction	1
1.1 Motivation of the project	1
1.2 Objectives and novelties of current project	3
1.3 Structure of the dissertation	4
2 Literature Review	6
2.1 Falling films over flat substrate	6
2.1.1 Evolution of film over flat wall	7
2.1.2 Steady-state laminar flow	10
2.1.3 Primary instability	12
2.1.4 Convective characteristics	14
2.1.5 Mechanism of the long-wave instability	16
2.2 Film flow over corrugated substrates	16
2.2.1 Laminar film flow over corrugated substrates (steady solution)	17
2.2.2 Separations in film flow over corrugation	19
2.2.3 Effect of wall corrugation on instability properties	20

2.3	Overview of techniques for film thickness measurement	28
2.3.1	Contact Method (Need-contact method)	30
2.3.2	Conductance Probe Technique	30
2.3.3	Fluorescence imaging method	32
2.3.4	Laser-induced fluorescence method	33
2.3.5	Photographic image processing	34
3	Experimental Setup and Problem Definition	36
3.1	Experimental facilities	36
3.1.1	Description of the inclined film setup	36
3.1.2	Description of the falling film set-up	38
3.2	Conductance Probe Method	40
3.2.1	Description of the technique	40
3.2.2	Probe geometry	41
3.2.3	Calibration method	43
3.2.4	Determination of marginal stability	44
3.3	Photographic image processing methods	48
3.4	Problem definition	50
4	Short wave instability	54
4.1	Introduction	54
4.2	Experiment Methodology	55
4.3	Result	56
4.3.1	Fundamental difference between flat and corrugated walls .	56
4.3.2	Characteristics of the short-wave mode	59
4.3.3	Investigation of the primary instability threshold	67
4.4	Concluding remarks	73
5	Effect of corrugated wall steepness	76
5.1	Introduction	76

CONTENTS

5.1.1	Experimental conditions	76
5.2	Results of sinusoidal substrate	77
5.2.1	Effect of wall steepness	77
5.2.2	Preliminary results of effect of liquid properties	80
5.3	Results on orthogonal substrate	85
5.4	Conclusion and discussion	86
6	Film flow around a vertical cylinder	92
6.1	Introduction	92
6.1.1	Experimental conditions	94
6.2	Experiment Results	94
6.3	Photographic image processing	100
6.3.1	Principles	100
6.3.2	Image processing procedure	106
6.3.3	Restriction of methods	110
6.4	Summary and discussion	110
7	An oscillatory behaviour at low Re	112
7.1	Introduction	112
7.2	Characteristic of the oscillatory instability	113
7.3	Occurrence of oscillation	122
7.4	Conclusion and discussion	127
8	Conclusions	132
8.1	Conclusion	132
8.2	Future work	134
	Appendix A	136
	Appendix B	140
	References	143

List of Figures

2.1	Schematic diagram of film flow over flat wall	7
2.2	Shadow image of waves naturally occurring on a film of water falling along a vertical plate at Reynolds number $Re = 33$. (Park & Nosoko, 2003)	8
2.3	Schematic of four wave regimes and corresponding wave spectra in a naturally excited evolution on a falling film from a slit (Chang, 1994).	9
2.4	Schematic diagram of Nusselt film flow over flat wall	10
2.5	Schematic of the development of a wave packet in the laboratory frame for convective/absolute instability (Kalliadasis <i>et al.</i> , 2012) .	15
2.6	Schematic diagram of film flow over corrugated substrate	17
2.7	Comparison of the free surface amplification predicted by laminar and by creeping-flow theory for $l_b = 0.002$ m and $\varphi = 60^\circ$. Circles correspond to results using a discretization of $N = 41$ points across the film (Bontozoglou & Papapolymerou, 1997).	18
2.8	Pictures of the path lines in the film flow at different flow rates together with numerical streamlines (Wierschem <i>et al.</i> , 2010). a, b, c and d corresponding to four Re , which are respectively 9, 16, 31 and 48.	20

LIST OF FIGURES

2.9	The critical Reynolds number, measured as a function of inclination angle for orthogonal corrugated wall. \square , $Ka = 3365$; \bullet , $Ka = 1102$; —, the neutrally stable Re for a flat wall (Vlachogiannis & Bontozoglou, 2002)	21
2.10	Minimum critical Reynolds number as function of the inclination angle obtained by Wierschem <i>et al.</i> (2005)	22
2.11	The ratio of the critical Re for a corrugated wall to the critical Re for a flat wall at the same inclination, as a function of wall steepness (Argyriadi <i>et al.</i> , 2006): (\times) $\varphi = 1.3^\circ$, (\blacktriangle) $\varphi = 2.6^\circ$ (Δ) $\varphi = 3.4^\circ$ (\blacksquare) $\varphi = 5.4^\circ$ (\square) $\varphi = 7.4^\circ$	23
2.12	Critical Reynolds number VS bottom amplitude with $\cot\varphi = 0.5$ and $\delta = h_N/l_b = 0.1$ (from D'Alessio <i>et al.</i> , 2009)	25
2.13	Neutral stability curves for the case with $\cot\varphi = 0.5$, $We = 5$, and $\delta = h_N/l_b = 0.1$ (from D'Alessio <i>et al.</i> , 2009)	25
2.14	Critical Reynolds number VS free surface amplitude ($A = a/d$) at different inverse Bond numbers. $\cot\varphi = 1$ and $\delta = 0.2$ Heining & Aksel (2009)	26
2.15	Critical Reynolds number Re_{crit} as a function of the waviness, ζ (Häcker & Uecker, 2009)	28
2.16	Sketch of the experimental apparatus: 1, overflow tank; 2, image grabbing system; 3, corrugated wall; 4, UV light source (Vlachogiannis & Bontozoglou, 2002)	33
2.17	A example of test section for PLIF measurements from Schubring <i>et al.</i> (2010)	34
2.18	A sketch of experiment apparatus from Wierschem <i>et al.</i> (2002)	35
3.1	Schematic diagram of inclined film flow channel	37
3.2	Schematic diagram of the falling film set-up	39
3.3	Schematic diagram of conductance probe method	40

LIST OF FIGURES

3.4	Schematic diagram of main types of conductance probes (Kang & Kim, 1992)	42
3.5	Calibration data of 60% glycerol on a corrugated wall ($\varphi = 3^\circ$, $l_b = 12$ mm, $a_b = 1.6$ mm)	43
3.6	Time series of film height for a 60 wt % glycerol solution at various Re ($l_b = 24$ mm, $a_b = 0.8$ mm, $\varphi = 25^\circ$).	46
3.7	Determination of marginal stability ($l_b = 24$ mm, $a_b = 0.8$ mm, $\varphi = 25^\circ$, 60 % Glycerol solution)	47
3.8	A example of raw image taken from the CCD camera.	49
3.9	Schematic diagram of film flow over flat wall	51
4.1	Schematic diagram of the film flow test section, with the geometric characteristics of the two corrugated walls (— — —, orthogonal wall; ·····, sinusoidal wall), and the typical location of a conductance probe.	55
4.2	Typical time series of liquid film height (·····, upstream signal; —, downstream signal, probe separation 500 mm) on a flat substrate at inclination $\varphi = 5^\circ$, resulting from an inlet disturbance of frequency $f = 0.167$ Hz. The three plots correspond to Re : 8.1, 15.6 and 19.3. The critical Reynolds is determined as $Re_{flat} = 13.1$	57
4.3	Time series of liquid film height (·····, upstream signal; —, downstream signal, probe separation 500 mm) on the sinusoidal substrate at inclination $\varphi = 10^\circ$, resulting from an inlet disturbance of frequency $f = 0.167$ Hz. The three plots correspond to Re : 5.3, 7.7 and 8.9. The onset of the high-frequency oscillation is determined—by a technique to be discussed in the next sub-section—as $Re_{cr} = 7.3$	59

4.4	Time series of liquid film height ($\cdots\cdots$, upstream signal; --- , downstream signal) on the sinusoidal substrate at inclination $\varphi = 10^\circ$, resulting only from ambient noise. The five plots correspond to Re : 5.7, 7.3, 9.1, 10.1 and 12.7. The critical Reynolds is determined as $Re_{cr} = 7.3$	60
4.5	Variation of the standard deviation of time signals with increasing Re at inclination 15° and 25° ((upstream: \square ; downstream: \circ).	61
4.6	Variation of the upstream (a) and downstream (b) standard deviation of time signals with increasing Re at inclination 15° (upstream: \blacksquare , downstream: \square) and 25° (upstream: \bullet , downstream: \circ). (c): log-log plot of STD with $(Re - Re_{cr})$	63
4.7	Fast Fourier Transform of a time signal without (a) and with (b) inlet disturbance, under condition of $Re = 7.0$ and inclination 15°	63
4.8	Time signals taken at the same streamwise distance from the inlet and symmetrically off the channel centreplane. a: $Re = 8.1$, b: $Re = 17.8$. The inclination is 15° and the experimental critical Reynolds is $Re_{cr} = 5.2$	64
4.9	a: cross-correlation, and b: autocorrelation of a time signal at $Re = 8.0$ and inclination 15°	65
4.10	a: Variation of wavelength, l/l_b , and b: variation of phase velocity, c/u_N , of the short-wave mode, as a function of Re/Re_{cr} . u_N is the mean Nusselt velocity. \square , $\varphi = 15^\circ$, \times , $\varphi = 25^\circ$	66
4.11	Wavelength of the short-wave mode at inception, as function of channel inclination. \bullet , sinusoidal, and \square , orthogonal wall.	67
4.12	Fast Fourier Transform of time signals taken along the orthogonal wall, at increasing inclination. a: $\varphi = 15^\circ$ ($Re = 11.2$), b: $\varphi = 20^\circ$ ($Re = 10.0$), c: $\varphi = 25^\circ$ ($Re = 8.6$) d: $\varphi = 30^\circ$ ($Re = 7.6$), e: $\varphi = 35^\circ$ ($Re = 5.6$).	68

4.13	The experimentally observed critical Reynolds, normalized with the theoretical prediction for a flat wall, as function of channel inclination. \bullet , sinusoidal, and \square , orthogonal wall.	68
4.14	Experimentally observed critical Reynolds number, normalized with the theoretical prediction for a flat wall, as function of channel inclination. Measurements taken by (Wierschem <i>et al.</i> , 2005) for silicon oil flowing along a sinusoidal substrate with $l_b = 300$ mm and $a_b = 15$ mm.	71
4.15	Critical Reynolds for the primary instability of liquid film flow along a sinusoidal wall. \square , present data; —, theoretical prediction for disturbances with infinite wavelength; \cdots , theoretical prediction for disturbances with the wavelength of the wall; $-\bullet-$, theoretical prediction for disturbances with the experimentally determined wavelength.	72
5.1	Measured (a) and normalized (b) critical Reynolds for the primary instability of liquid film flow along small sinusoidal corrugation($L_b = 0.82$, $A_b = 0.5$). \square , experimental data; —, theoretical prediction for flat substrate.	79
5.2	Measured (a) and normalized (b) critical Reynolds for the primary instability of liquid film flow along large sinusoidal corrugation($L_b = 20.4$, $A_b = 0.2$). \square , experimental data; —, theoretical prediction for flat substrate.	81
5.3	Measured (a) and normalized (b) critical Reynolds for the primary instability of liquid film flow along an intermediate sinusoidal wall ($L_b = 4.9$, $A_b = 0.167$). \square , experimental data; —, theoretical prediction for flat substrate.	82
5.4	Normalized critical Reynolds for the primary instability of liquid film flow along three sinusoidal corrugations. (\times), $L_b = 0.82$, $A_b = 0.5$; (\square), $L_b = 20.4$, $A_b = 0.2$; (\circ), $L_b = 4.9$, $A_b = 0.167$	83

5.5	Critical Reynolds for the primary instability of liquid film flow along a sinusoidal corrugation($L_b=4.9$, $A_b = 0.167$). $-\bullet-$ and $-\blacksquare-$ are respectively for $Ka=260$ and 110.——, theoretical prediction for disturbances with infinite wavelength.	84
5.6	Measured (a) and normalized (b) critical Reynolds for the primary instability of liquid film flow along an orthogonal corrugation($L_b=9.7$, $A_b = 0.033$). \square , experimental data; ——, theoretical prediction for disturbances with infinite wavelength.	87
5.7	Measured (a) and normalized (b) critical Reynolds for the primary instability of liquid film flow along an orthogonal corrugation($L_b=4.9$, $A_b = 0.067$). \square , experimental data; ——, theoretical prediction for disturbances with infinite wavelength.	88
5.8	Measured (a) and normalized (b) critical Reynolds for the primary instability of liquid film flow along an orthogonal corrugation($L_b=4.9$, $A_b = 0.133$). \square , experimental data; ——, theoretical prediction for disturbances with infinite wavelength.	89
5.9	Normalized critical Reynolds for the primary instability of liquid film flow along three orthogonal corrugations. \blacktriangle , $A_b = 0.033$; $-\bullet-$, $A_b = 0.067$; $-\blacksquare-$, $A_b = 0.133$	90
6.1	Schematic diagram of the film flow test section with the geometric characteristics of the corrugation, and the typical location of a conductance probe.	93
6.2	Time series of liquid film height (green(thick) line: upstream signal; red(thin) line: downstream signal) on the vertical cylinder, resulting only from ambient noise. The seven plots correspond to Re : 1.19, 1.82, 2.15, 2.39, 2.64, 3.39 and 3.86.	95
6.3	Variation of the upstream and downstream standard deviation of time signals with increasing Re	96

LIST OF FIGURES

6.4	Variation of critical Re with Kaptiza number. The three points correspond to $Ka = 10.1, 37.1$ (Zioulis, 2011) and 92.	97
6.5	a: cross-correlation, and b: autocorrelation of time signal at $Re = 4.07$	98
6.6	a: Variation of wavelength, l/l_b , and b: variation of phase velocity, c/u_N , as a function of Re/Re_{cr}	99
6.7	Wavelength of the short-wave mode at inception, as function of channel inclination	100
6.8	A example of raw image taken from the CCD camera (the red line is the mark of a row of pixels, which will be shown in the following text).	101
6.9	The intensity variation along a row of pixels, corresponding to the red line in figure 6.8	103
6.10	The histogram of the raw image	104
6.11	The processed image by applying a window-level contrast stretching function	105
6.12	The processed image after step 1	107
6.13	An example of edge detection. The red line corresponds to the detected edge using Canny method.	108
6.14	Free surface profile obtained by calibration	109
6.15	Spatial film thickness determined by image processing	109
6.16	Auto-correlation of spatial film thickness	110
7.1	Time series of liquid height on an orthogonally corrugated wall ($l_b = 12$ mm $a_b = 1.6$ mm) at inclination $\varphi = 45^\circ$ ($Ka = 137$). Green (thick) and red line are respectively corresponds to upstream and downstream signal	114
7.2	Variation of standard deviation of time signals with Re on an orthogonally corrugated wall ($l_b = 12$ mm $a_b = 1.6$ mm) at $\varphi = 45^\circ$ ($Ka = 137$).	115

LIST OF FIGURES

7.3	Time series of liquid height on an orthogonally corrugated wall ($l_b = 12$ mm $a_b = 2.0$ mm) at $\varphi = 45^\circ$ ($Ka = 169$). Red, blue and green line are respectively 370 mm, 430 mm and 485 mm from the onset of the corrugation.	117
7.4	Time series of liquid height on an orthogonally corrugated wall with low-frequency disturbance ($l_b = 12$ mm $a_b = 2.0$ mm) at $\varphi = 45^\circ$ ($Ka = 134$).	118
7.5	Fast Fourier Transform of a time signal without (a) and with (b) inlet disturbance. ($Ka = 134$, $l_b = 12$ mm $a_b = 2.0$ mm). $Re = 1.83$ (a); $Re = 1.41$ (b)	119
7.6	The frequency of oscillation VS Re at two different orthogonal corrugations	120
7.7	Time series of liquid height with the condition of changing Re from 1.78 to 1.59	121
7.8	Time series of liquid height with a pulse disturbance at $Re = 2.40$.	121
7.9	a: cross-correlation, and b: autocorrelation of a time signal at $Re = 2.06$ ($a_b = 1.6$ mm, $\varphi = 45^\circ$)	122
7.10	The wavelength of oscillation at different Re ($Ka = 181$, $l_b = 12$ mm $a_b = 1.6$ mm).	123
7.11	An example of time series with vanishing flow rate, which oscillation exists ($Ka = 85$, $l_b = 12$ mm $a_b = 1.6$ mm).	124
7.12	An example of time series with vanishing flow rate, which has no oscillation ($Ka = 138$, $l_b = 12$ mm $a_b = 1.6$ mm).	125
7.13	An example of time series with vanishing flow rate (Sinusoidal, $l_b = 12$ mm $a_b = 2.0$ mm).	126
7.14	Time series of liquid height on an orthogonally corrugated wall ($l_b = 12$ mm $a_b = 1.6$ mm) at $\varphi = 45^\circ$ ($Ka = 92$)	128
7.15	Time series of liquid height on an orthogonally corrugated wall ($l_b = 12$ mm $a_b = 1.6$ mm) at $\varphi = 45^\circ$ ($Ka = 85$)	129

LIST OF FIGURES

7.16 Time series of liquid height on an orthogonally corrugated wall ($l_b=12$ mm $a_b=1.6$ mm) at $\varphi=45^\circ$ ($Ka=50$)	130
---	-----

Nomenclature

Roman Symbols

Bo^{-1}	Inverse Bond number
g	Gravitational acceleration
h	Thickness of film flow
h_N	Mean film thickness based on the steady flow Nusselt solution
Ka	Kapitza number
a_b	Amplitude of corrugation
l_b	Wavelength of corrugation
l_c	Capillary length of the liquid
l_ν	Viscous length of the liquid
p	Pressure of the primary flow
P_0	Ambient atmospheric pressure
q	Volumetric flow rate per unit width
Re	Reynolds number
Re_{cr}	Critical Re for film over corrugations

LIST OF FIGURES

Re_{flat} Critical Re of film over flat substrate

u Velocity of film flow

u_{max} Maximum velocity at free surface

We Weber number

Greek Symbols

μ Dynamic viscosity of the fluid

ν Viscosity of the liquid

ρ Density of the liquid

σ Surface tension of liquid

φ Inclination angle of wall substrate

Subscripts

N Based on the Nusselt solution

max Maximum velocity at free surface

Chapter 1

Introduction

1.1 Motivation of the project

Thin liquid films exhibit a variety of intriguing and fascinating dynamic behaviours, which have been studied over decades with increasing interest, due to their broad appearance in both daily life and industry applications. They occur over a wide range of scales, from small scales such as microfluids and nanofluids, to large scale as lava or continental ice sheet. A considerable amount of literature has been published on various aspects of film flow, and the problem has been reviewed extensively (Chang & Demekhin, 2002; Craster & Matar, 2009; Oron *et al.*, 1997).

Falling film flows, which are driven by gravity flowing down an inclined plane or a vertical wall in the presence of free surfaces, are of specific interest of current work. This kind of configuration is encountered in various important applications in the industry: particularly in coating process (Quéré, 1999; Weinstein & Ruschak, 2004) and heat and mass transfer equipment (de Santos *et al.*, 1991; Helbig *et al.*, 2009; Valluri *et al.*, 2005). The interfacial waves are sometimes desirable: for instance, they enhance the heat and mass transfer in heat exchangers or reactors. On the other hand, it may be unpleasant to have interfacial waves in

coating process, since undisturbed flow is crucial for the uniformity of the coating. Since the substrates of film flow are not flat in most cases in reality, it is of obvious interest to investigate how the substrates topography will affect the instability of film flow, which not only presents a fundamental physical interest, but also potentially helps to control the instability in real industrial applications by tailored corrugations.

The available literature for films over topography may be schematically categorized around two complementary cases (i) the reaction of film flow to an isolated topographical feature, such as a step, a protrusion or an intrusion (Bontozoglou & Serifi, 2008; Gaskell *et al.*, 2004; Kalliadasis & Homsy, 2001), and (ii) the reaction to a wall consisting of periodic corrugations. The present contribution deals with the latter case.

In recently years, there has been an increasing number of publications trying to investigate the instability of film flow over corrugations, including a few experimental works (Argyriadi *et al.*, 2006; Vlachogiannis & Bontozoglou, 2002) and more theoretical studies (e.g. Dávalos-Orozco, 2007; Oron & Heining, 2008; Trifonov, 2007). Most previous studies, which are over a limited parameter range, show that the corrugated wall imposes a stabilizing effect on the film flow and expands the stable regime. However, some more recent computational studies (e.g. D'Alessio *et al.*, 2009; Häcker & Uecker, 2009) predict that large corrugations may have a destabilizing effect under certain conditions. Obviously, study of the effect of wall corrugation over a wide parameter range is necessary for comprehensive understanding of the problem. Meanwhile, the majority of studies are based on theoretical analysis or numerical simulation, and experimental data are relatively rare. Thus, motivated by these results, the current study aims to perform an experimental study of the primary instability of film flow along corrugations in a wider range of parameters, to provide an experimental perspective of the problem.

1.2 Objectives and novelties of current project

The objective of current research is to investigate the effect of wall corrugations on the instability properties of film flows, in particular, the mode of instability, and onset of the primary instability, which is the critical Reynolds number (Re) that film flow transits from steady to unsteady regime. The main parameters to be investigated are the shape of corrugations (sinusoidal and orthogonal), geometries of wall corrugations (various wavelengths and amplitudes), inclination angles as well as two distinct configurations of set-up (channel flow and vertical cylinder). The experiments were performed over two experimental apparatuses (an inclined film flow channel and a vertical cylinder system) at Transport Processes & Process Equipment Laboratory in University of Thessaly.

In the current dissertation, the most remarkable observation is a new instability mode of film flow, which is referred to as short-wave mode. It is found that, under certain conditions (for specific inclination angles or beyond specific steepness), the short-wave instability mode occurs before the classical, convective, long-wave one. The short-wave mode is highly regular and persistently two-dimensional. The inclination angle, exact shape (sinusoidal or orthogonal) and wall steepness has a leading-order effect on the mode of primary instability, which was documented in the current dissertation.

Next, the effect of wall corrugations on the onset of primary instability was tested over a wide range of wall geometries. Compared to the behaviour of film flow on a flat substrate, the tested walls are found having a stabilizing effect under majority conditions, except for steep orthogonal corrugations at high inclinations, when an oscillatory behaviour is observed at very low Re . Moreover, the extent of the stabilizing effect varies significantly with wall geometry and inclination angles.

An interesting oscillatory behaviour, which occurs at low Re , is also reported in the dissertation. The oscillation is found more remarkable at lower Re , and exists till the flow rate approaching zero. This counter-intuitive behaviour may

be related to absolute instability caused by separations in the trough of the corrugations, and is also an evidence of destabilizing effect imposed by orthogonal wall corrugations.

The main technique employed in the current project, is conductance probes method, which is used for measurement of the temporal variation of film thickness at specific locations. A new approach, which is based on the standard deviation of the time signal from the conductance probe, is developed and proved sufficient for detection of onset of instability. For film over vertical cylinder, an alternative technique based on direct photography, is developed, which is able to capture the free surface profile and measure the spatial variation of film thickness.

1.3 Structure of the dissertation

This dissertation is presented with the following structure:

In Chapter 2, a brief literature review of film flows over flat and corrugated substrates is provided, including the steady solution, primary instability and transition mechanism. Moreover, some widely used techniques for film thickness measurement are also introduced.

Chapter 3 is devoted to descriptions of experimental methodology in the current study. The experimental apparatus, including an inclined film flow channel and a vertical cylindrical film flow rig are described. Moreover, the measurement techniques for liquid properties, flow rate and film thickness are presented. Since the film thickness is the most important parameter in film flow, the design and calibration of conductance probe technique are discussed in details. In addition, the determination method of the typical long-wave instability is provided.

Chapters 4, 5, 6 and 7 are concerned with experimental results of the current project. Chapter 4 concentrates on the new short-wave instability, which is the main observation in current dissertation. In Chapter 5, the main results regarding the effect of wall corrugations on the onset of primary instability of film flow are

discussed. Chapter 6 presents the results of film flow over the vertical cylinder, as well as the applicaiton of a new technique for film thickness measurement based on direct photography. Results of interesting low- Re instability, which occurs specifically on steep corrugations at high inclination, are presented and discussed in Chapter 7.

Finally, the last chapter, the conclusions, gives a brief summary of the main findings in the project as well as some recommendations for further work.

Chapter 2

Literature Review

2.1 Falling films over flat substrate

Film flow over flat substrate has been studied more thoroughly compared to that over corrugated substrates, and will be discussed first in the following section. The system of interests is an incompressible Newtonian fluid flowing down a flat substrate with an inclination angle, φ , as shown schematically in figure 2.1. Coordinates are chosen as x is the downstream direction, and y is in the normal direction.

The problem is typically defined in two independent dimensionless parameters: (i) the Reynolds number,

$$Re = \frac{q}{\nu} \quad (2.1)$$

where q is volumetric flow rate per unit width, and (ii) the Kapitza number, defined as,

$$Ka = \frac{\sigma}{\rho(g \sin \varphi)^{1/3} \nu^{4/3}} \quad (2.2)$$

where σ , ρ , ν are respectively the surface tension, density, kinematic viscosity of the fluid, and g is the gravitational acceleration. The advantage of using

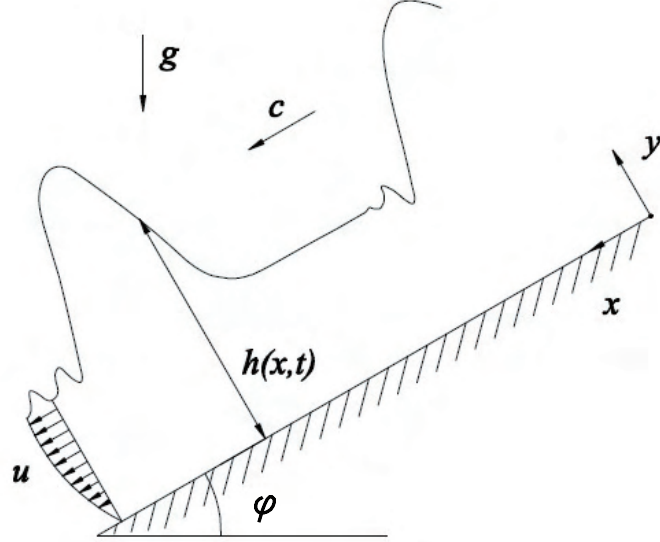


Figure 2.1: Schematic diagram of film flow over flat wall

Kapitza number is that it depends only on physical properties and represents the competition between capillary and viscous phenomena. Some authors use a different scaling, for instance, Re and the Weber number,

$$We = \frac{\sigma}{\rho g^2 h_N \sin \varphi} \quad (2.3)$$

where h_N is the Nusselt film thickness, to be defined in the next paragraph.

2.1.1 Evolution of film over flat wall

The evolution of film flow is usually characterized by Reynolds number, Re . For Re below a critical value, the film is in the stable regime, in which all the disturbances will be damped and eventually disappear, leaving a steady and flat free surface. For Re above the critical value, the flow is in the unstable regime, in which the instability starts to develop. Figure 2.2 depicts an example of waves naturally occurring on a film of water falling along a vertical plate (Park & Nosoko, 2003). As qualitatively shown in the figure, along streamwise direction,

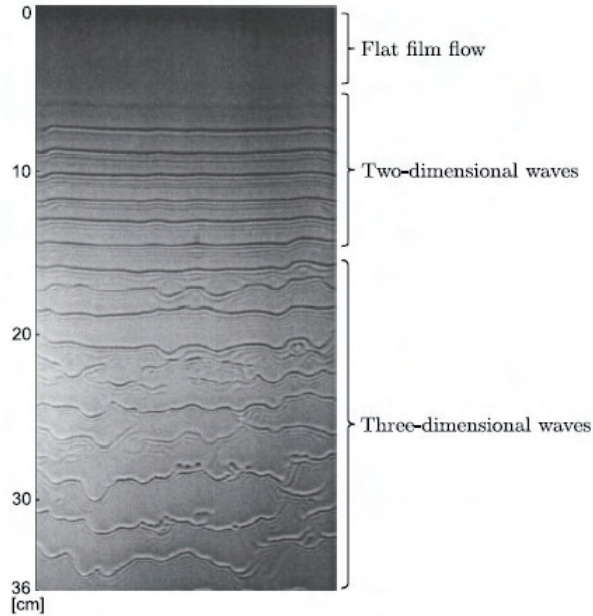


Figure 2.2: Shadow image of waves naturally occurring on a film of water falling along a vertical plate at Reynolds number $Re = 33$. (Park & Nosoko, 2003)

flat film flow first develops a two-dimensional periodic wave train, after which further evolves to solitary waves, and eventually to three-dimensional and complex wave patterns.

More systematic classification of the stages of wave evolution can be found in the review paper by Chang (1994). Four distinct wave regions have been observed, as shown in the schematic of figure 2.3. In the inception region (region I), infinitesimal disturbances at the inlet are amplified downstream to form a monochromatic wave at the end of the region. The amplitude of the monochromatic wave grows exponentially downstream as in all linear excitation processes of convectively unstable systems. Noteworthy is that the transverse disturbances are selectively damped in this region resulting in two-dimensional waves.

The first stage is followed by a second stage (region II) with saturation of the linear growth. In the region II, weakly nonlinear interaction between an unstable fundamental Fourier mode and a stable second harmonic occurs, which

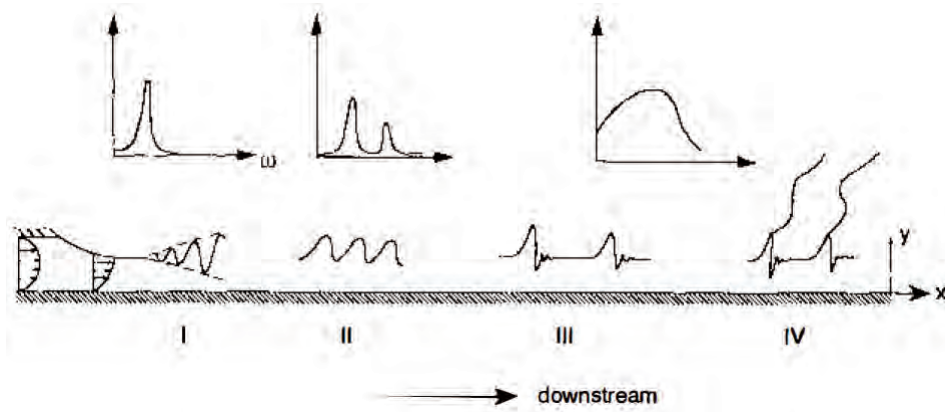


Figure 2.3: Schematic of four wave regimes and corresponding wave spectra in a naturally excited evolution on a falling film from a slit (Chang, 1994).

causes monochromatic wave to develop a finite overtone as its sinusoidal shape steepens downstream. The wave speed in this region is slowed as waves grow, due to a negative nonlinear correction, and the wavelength is also different from the monochromatic wave in region I due to the nonlinear selection mechanism. Moreover, the waves travel a long distance (~ 10 wavelengths) without changing much with their shape and speed.

In region III, due to the interaction of two dominant instabilities, wave coalescence occurs, and leads to some intermittent patches. This process can result when neighbouring waves coalesce at intermittent locations due to a sub-harmonic instability, or when a long-range modulation takes place due to the sideband instabilities. Within the patches, the distorted waves grow in wavelength and amplitude, and further evolve into characteristic spatially localized teardrop humps, which have steep front and a series of front-running ripples of the characteristic wavelength close to the monochromatic waves at inception (Chang, 1994).

In the final region (IV), the instability in the transverse direction starts to develop at the crests of the solitary humps. The increasing amplitude in the direction parallel to the wall causes the adjacent crests to merge at various points and pinch off. The flow appears with a three-dimensional structure.

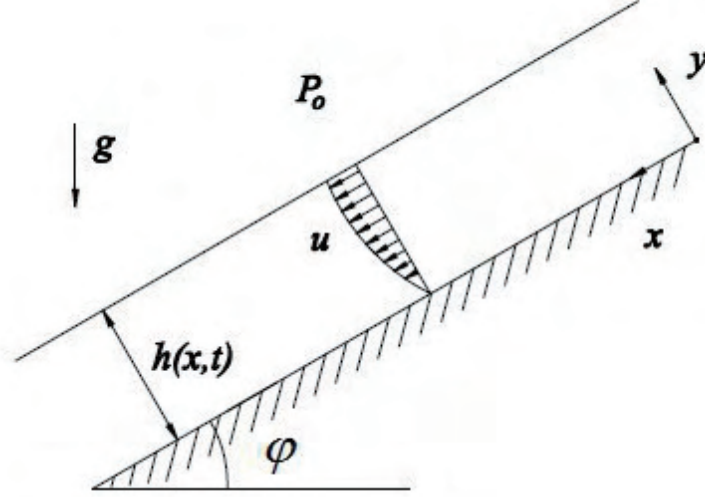


Figure 2.4: Schematic diagram of Nusselt film flow over flat wall

In the current study, we will concentrate on the transition from steady flow to the first stage of wave evolution, which is referred to as primary instability.

2.1.2 Steady-state laminar flow

Prior to discussing the primary instability of film flow, the steady solution for laminar film will be presented here. The first attempt to solve the steady solution is done by Nusselt (1916). As shown in figure 2.4, we consider that a layer of a viscous fluid of thickness h flows down a plate that is inclined by an angle φ to the horizontal surface. Since the flow is steady, the parameters of the film flow are constant and the shear stress force is balanced by the gravitational force. Thus, the Navier-Stokes equation takes a simple form for steady film flow

$$\mu \frac{d^2 u}{dy^2} + \rho g \sin \varphi = 0 \quad (2.4)$$

$$-\frac{dp}{dy} + \rho g \cos \varphi = 0 \quad (2.5)$$

in which μ is the dynamic viscosity of the fluid, p is the pressure of the primary flow. The boundary conditions are

$$u = 0 \text{ at } y = 0 \text{ (no-slip condition)}$$

$$\frac{du}{dy} = 0 \text{ at } y = h \text{ (absence of shear stresses on the free surface)}$$

$$p = P_0 \text{ at } y = h$$

The velocity profile and static pressure can be obtained by integrating the initial system of equations, as following:

$$u = \frac{\rho g \sin \varphi}{\mu} \left(y h - \frac{y^2}{2} \right) \quad (2.6)$$

$$p = P_0 + \rho g \cos \varphi (h - y) \quad (2.7)$$

where P_0 is the ambient atmospheric pressure. From equation 2.6, it is easy to find out that the maximum velocity is at free surface, with its value as:

$$u_{max} = \frac{\rho g \sin \varphi}{2\mu} h^2 \quad (2.8)$$

The flow rate per unit width can be obtained by integrating the velocity across the film:

$$q = \int_0^h u dy = \frac{\rho g h^3}{3\mu} \sin \varphi \quad (2.9)$$

Given the flow rate q and the kinematic viscosity of the liquid, $\nu = \mu/\rho$, The mean film Nusselt thickness h_N , can be calculated as

$$h_N = \left(\frac{3q\nu}{g \sin \varphi} \right)^{\frac{1}{3}} \quad (2.10)$$

And the mean film velocity of Nusselt solution, u_N , can be obtained as following:

$$u_N = \frac{gh_N^2 \sin \varphi}{3\nu} = \frac{2}{3}u_{max} \quad (2.11)$$

2.1.3 Primary instability

A question of evident interest is at which condition will the Nusselt flow deviates from steady-state and enter the unstable regime. The linearization of the Navier-Stokes equation with the condition of two-dimensional infinitesimal perturbation leads to the Orr-Sommerfeld equation, which is further solved by long-wave expansion (Benjamin, 1957; Yih, 1963, 1967). The key finding is that the film flow will first be destabilized by long-waves when above a critical Reynolds number, which is given as:

$$Re_{flat} = \frac{5}{6} \cot \varphi \quad (2.12)$$

where φ is the inclination angle. The early works by Benjamin and Yih are restricted to small Reynolds number. This was further extended to larger Re by some other authors both analytically (Anshus & Goren, 1966; Krantz & Goren, 1971) and numerically (Chin *et al.*, 1986; Pierson & Whitaker, 1977; Whitaker, 1964). The result was verified experimentally by Liu *et al.* (1993), who first proposed an experimental method for detection of onset of the primary instability.

In their studies, the influence of surface tension on the onset of primary instability is negligible, since the most unstable waves are the waves with longest wavelength where the curvature at the free surface is lowest. However, equation 2.12 will not be sufficient to predict the correct threshold, if the disturbance is no longer two-dimensional (side-wall effect). The effect of sidewall on the primary instability of inclined film flow was studied experimentally by Vlachogiannis *et al.* (2010), using conductance probe methods to detect wave evolution. They reported that films flow at small and intermediate inclination angles are significantly more stable with smaller channel width. Based on a fluorescence imaging

method, Georgantaki *et al.* (2011) further demonstrated experimentally that the delay in the primary instability scales with the ratio of capillary to viscous forces (expressed by Kapitza number), which is attributed to a long-range transverse coherence. The sidewall effect on the primary instability with two different contact angles between liquid and the side wall was studied experimental by Pollak *et al.* (2011). The influences of different capillary boundary layer effects at the side walls, on the instability of the free surface, are resolved by varying the crosswise side wall distance of the measurement positions. One of the interesting observations is the coexistence of unstable and stable regions: the flow may be unstable in the center of the channel, but stable in the vicinity of the sidewall.

In order to study the flow evolution subsequent to wave inception, nonlinear stability theories have been developed. Benney (1966) first derived a nonlinear evolution equation for two-dimensional flows on an inclined plate, which is known nowadays as Benney equation. Benney equation successfully predicted the critical Reynolds number and described the dynamics of falling liquid films close to the threshold. It has been studied over the years, and was further developed by a number of authors (e.g. Gjevik, 1970; Lin, 1969; Nakaya, 1975). However, it was found that the solutions of the Benney equation grow without bound in a certain subdomain of the linearly unstable region of the system (Oron & Gottlieb, 2002; Pumir *et al.*, 1983; Rosenau *et al.*, 1992; Scheid *et al.*, 2005)

An alternative model, which is based on boundary-layer theory, was firstly proposed by Shkadov (1967). This approach can describe the dynamics of falling films over vertical and inclined substrates for intermediate Reynolds number ($Re < 300$). However, it fails to recover the correct threshold of primary instability as equation 2.12. This drawback was overcome by Ruyer-Quil & Manneville (2000, 2002) by combining a systematic gradient expansion with weighted residual techniques using polynomials as test functions. By applying a Galerkin method, a two-equation model, which involves local flow rate q and local thickness h of the film, is obtained, known as weighted-residual integral boundary layer (WRIBL)

model. The linear stability analysis of this model leads to an instability threshold that matches the Orr-Sommerfeld results, at least up to moderate Reynolds numbers ($Re \sim 50$). Moreover, in the strongly nonlinear regime, the spatial evolution that produced by the model in the presence of the noise or periodic forcing compares quantitatively to the previous experimental and numerical evidences (Liu & Gollub, 1994; Ramaswamy *et al.*, 1996). Thereafter, the WRIBL model was studied by a number of authors under various conditions (e.g. Mudunuri & Balakotaiah, 2006; Scheid *et al.*, 2005). More recently, Oron *et al.* (2009) studied vertical falling film in the framework of the first-order time-dependent WRIBL equation with periodic boundary condition. In his study, the critical Reynolds number based on linear analysis of the model is presented as following:

$$Re_{flat} = \frac{5}{6} \left[\cot \varphi + Ka \left(\frac{2\pi l_\nu}{L} \right) \right] \quad (2.13)$$

where L is the wavelength of the imposed disturbance, Ka and l_ν are respectively the Kapitza number and the viscous length-scale. This expression contains the first-order effect of disturbances of finite length.

2.1.4 Convective characteristics

An important character of instability of film flow is whether the instability is absolute or convective. This concept was originally developed in plasma physics (Briggs, 1964) and later applied to hydrodynamics (Huerre & Monkewitz, 1985). A flow is said to be convectively unstable, when a perturbation grows with respect to coordinates moving with the disturbance but decay in the laboratory frame of reference. The flow responds to upstream perturbations as a noise amplifier. On the other hand, in an absolutely unstable system, the perturbations grow at a fixed laboratory frame, i.e. they are able to move upstream. In this case, the flow behaves as an oscillator having its own intrinsic dynamics. The schematic diagram of the development of wave packet in the laboratory frame for convective/absolute

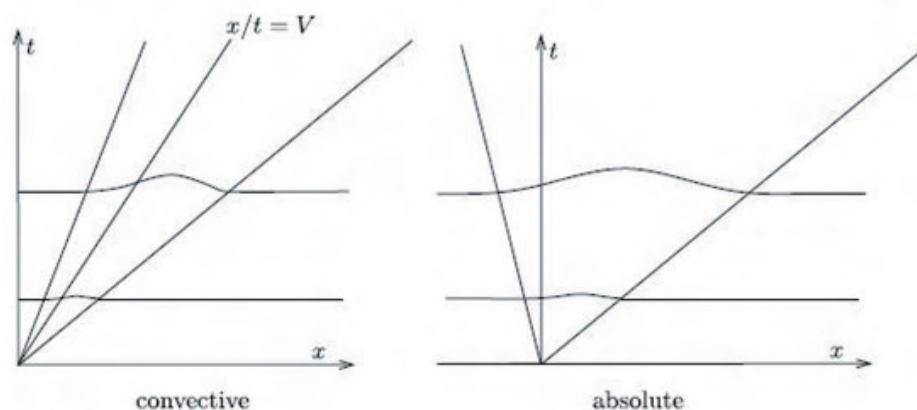


Figure 2.5: Schematic of the development of a wave packet in the laboratory frame for convective/absolute instability (Kalliadasis *et al.*, 2012)

instability is shown in figure 2.5.

An important characteristic associated with the distinction is that a convective instability is extremely sensitive to the external perturbation at inlet. The resulting wave patterns at downstream are in fact “noise-sustained structures” whose amplitudes can depend on the amount of external noise. In contrast, the patterns resulting from absolute instability are less sensitive to the external noise, except during their initiation (Liu *et al.*, 1993).

For film flow over flat plane, it was first noted by Benjamin (1961) that a localized disturbance is transported downstream. Linear analysis, which is based on long-wave expansion equation of Benney (1966), predicts that the primary instability of film flows is convective, rather than absolute, near the critical Reynolds number (Joo & Davis, 1992; Liu *et al.*, 1992). The analysis also predicts a convective-absolute instability transition at high Reynolds number. However, this prediction is not reliable since the dominant wavenumbers at corresponding Re is out of validity domain of long-wave expansion. Experimentally, Liu *et al.* (1993) investigated the character of the instability of film flow, and demonstrated that film flows are convectively unstable over the entire range of their measurement (up to $Re = 200$ for $\varphi < 10^\circ$).

2.1.5 Mechanism of the long-wave instability

Some researchers have attempted to investigate the physical mechanism of the long-wave instability. Kelly *et al.* (1989) conducted energy analysis of the film flow on an inclined plane for disturbance with arbitrary wavelength, and identified the various contributions to the disturbance energy. The main conclusion is that energy of disturbance of a falling film increases at moderate Reynolds number attributed to the work done by the perturbation shear stress at the surface of the film.

An alternative mechanism for the long-wave instability is proposed by Smith (1990). In his study, the complete detailed mechanism is composed of an initiating mechanism that produces dominant motion in the film and a growth mechanism which produces the unstable motion of the interface. The initiating mechanism is further classified into stress-induced and velocity-induced instability. A liquid film on a rigid inclined plane bounded above by a free surface is dominated by stress-induced instability.

2.2 Film flow over corrugated substrates

The literature regarding film over corrugated substrate, will be discussed in the following section. Key lengthscales of the problem are the wavelength, l_b , and the height, a_b , introduced by the wall (figure 2.6). In the literature (e.g. Nguyen & Bontozoglou, 2011; Trifonov, 2007), l_b is usually normalized with the capillary length of the liquid, $L_b = l_b/l_c$. l_c is defined as:

$$l_c = \left(\frac{\sigma}{\rho g}\right)^{0.5} \quad (2.14)$$

The height, a_b , is normalized as the steepness, $A_b = a_b/l_b$.

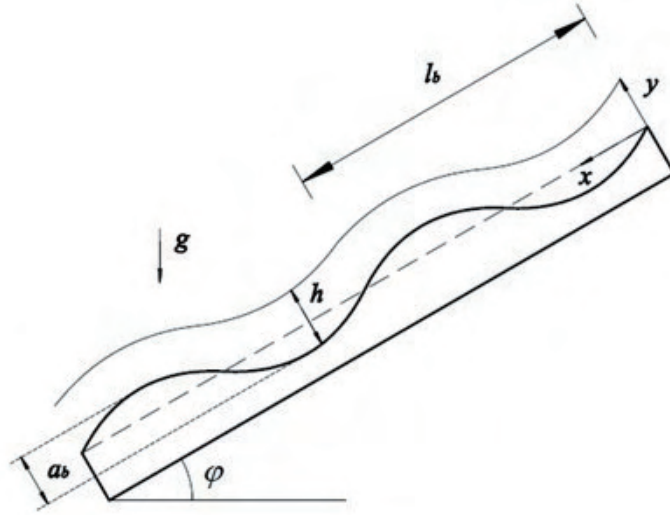


Figure 2.6: Schematic diagram of film flow over corrugated substrate

2.2.1 Laminar film flow over corrugated substrates (steady solution)

Gravity-driven films along a periodic wall were initially studied in the special case of creeping flow (Pozrikidis, 1988; Shetty & Cerro, 1993; Wang, 1981). Wang (1981) first performed an asymptotic analysis for sinusoidal wall with small-amplitude variations, in which the velocity profile and free surface profile were determined at condition of small Reynolds number. The analysis was further extended to the separated flow of two fluids by some other authors (e.g. Dassori *et al.*, 1984; Kang & Chen, 1995). Later, a more detailed examination was carried out by Pozrikidis (1988), who applied boundary-integral method to creeping flow. In his work, the free surface profile and flow structures were investigated numerically with varying flow rates, inclination angles, surface tensions and arbitrary wall geometries. Shetty & Cerro (1993), using asymptotic analysis, demonstrated that the flow of a viscous liquid down a wavy surface follows a local Nusselt solution in the limit of negligible inertia and capillary effects.

The effect of inertia was considered more recently, and led to the conclusion

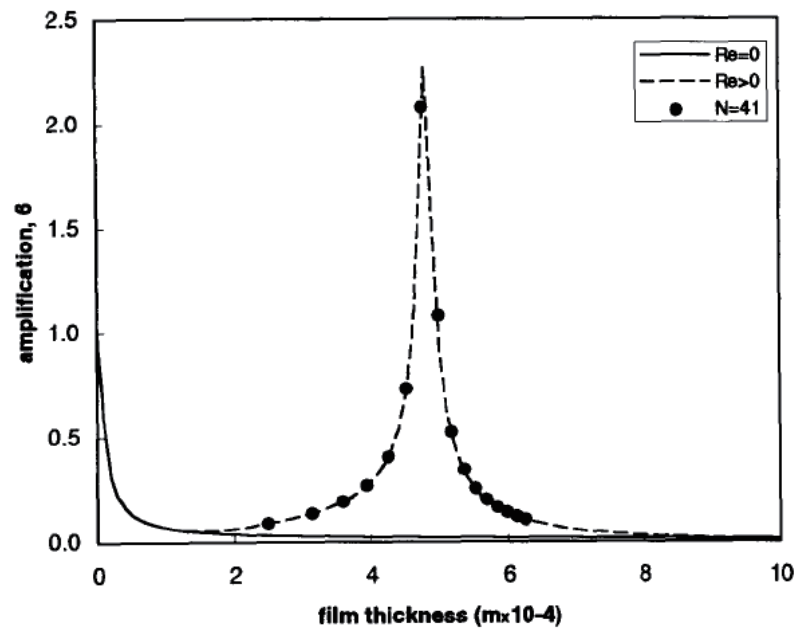


Figure 2.7: Comparison of the free surface amplification predicted by laminar and by creeping-flow theory for $l_b = 0.002$ m and $\varphi = 60^\circ$. Circles correspond to results using a discretization of $N = 41$ points across the film (Bontozoglou & Papapolymerou, 1997).

that even a wall with small-amplitude corrugations can affect the mean liquid flow in a non-trivial way (Bontozoglou & Papapolymerou, 1997; Luo & Pozrikidis, 2006; Trifonov, 1999; Wierschem *et al.*, 2008). This was first observed by Bontozoglou & Papapolymerou (1997), who carried out a linear analysis and predicted a resonance interaction between the free surface and bottom undulation, in case of intermediate range of Re . The resonance phenomena are manifested as a significant amplification of the wall deformation at the free surface. As shown in figure 2.7, as the thickness of the film increases (corresponding to higher Re), the amplification of free surface deformation changes drastically, which is reminiscent of the resonance of horizontal inviscid flow. This phenomenon has been further investigated numerically (Bontozoglou, 2000) and confirmed experimentally (Vlachogiannis & Bontozoglou, 2002; Wierschem & Aksel, 2004). A more recent study is published by Wierschem *et al.* (2008), which provided systematic investigation with arbitrary thickness and further demonstrated that resonance is associated with an interaction of deformed film with capillary-gravity waves that are travelling against the mean flow direction.

2.2.2 Separations in film flow over corrugation

Another manifestation of film flow over corrugation is the possible appearance of separations (eddies) in the trough of wall corrugation. For sufficient wall steepness, eddies could be induced both kinematically and inertially, which occur at relative low and high Reynolds number respectively.

For low Reynolds number, an experimental study carried out by Wierschem *et al.* (2003) shows that the eddy will be generated and developed beyond a critical film thickness, which are consistent with later analytical investigation by Scholle *et al.* (2004). The work which takes into account of inertial effect includes the theoretical analysis of film over vertical undulated surface with a wide range of Reynolds number by Trifonov (1999) and a recent systematic study by Scholle *et al.* (2008) and Nguyen & Bontozoglou (2011), who provided a detailed

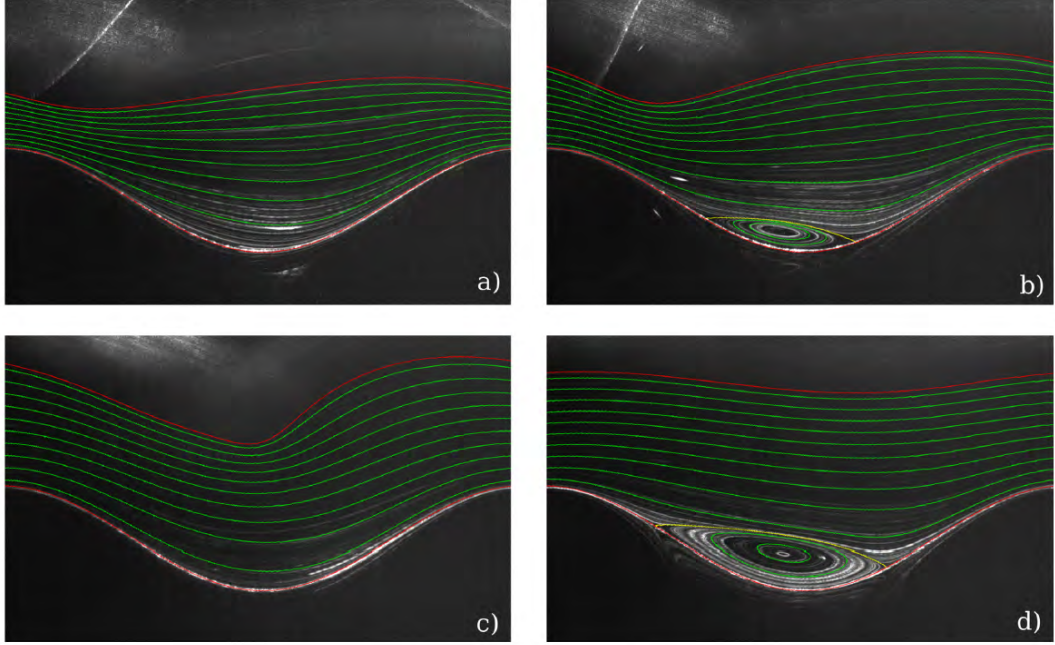


Figure 2.8: Pictures of the path lines in the film flow at different flow rates together with numerical streamlines (Wierschem *et al.*, 2010). a, b, c and d corresponding to four Re , which are respectively 9, 16, 31 and 48.

investigation of formation and presence of eddies with varying geometry and inertia and also defined a critical steepness of transition from kinematically to inertially induced local eddy flow structure.

Wierschem *et al.* (2010) performed numerical and experimental studies on the film over undulated topography, and indicated that eddies created in the troughs of the substrate by an increase of inertia can disappear in an interval of Reynolds numbers. Moreover, it has been shown that eddies are specifically suppressed where the fundamental harmonic of the free-surface contour is sufficiently amplified by resonance of the free surface with the bottom undulation (figure 2.8).

2.2.3 Effect of wall corrugation on instability properties

It is already known that, in the case of a flat wall, linear stability analysis predicts a long-wave instability with critical Reynolds number, Re_{flat} , proportional to the

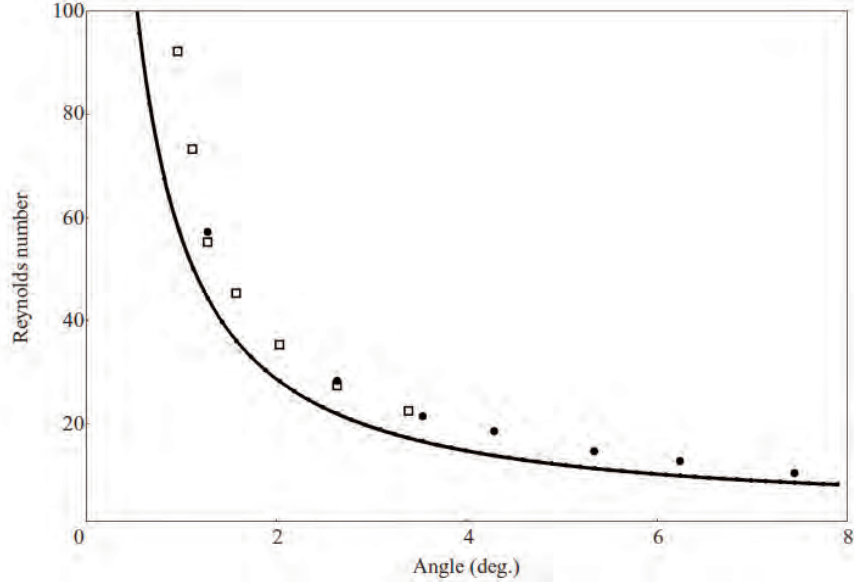


Figure 2.9: The critical Reynolds number, measured as a function of inclination angle for orthogonal corrugated wall. \square , $Ka = 3365$; \bullet , $Ka = 1102$; —, the neutrally stable Re for a flat wall (Vlachogiannis & Bontozoglou, 2002)

cotangent of inclination angle, $Re_{flat} = (5/6)cot\varphi$. Thus, a question of evident interest is the effect of a periodically corrugated wall on the primary instability of film flow, as expressed by the critical Reynolds number, Re_{cr} .

Indeed, there is growing evidence in the literature that such a wall affects the stability characteristics of the film, to an extent that makes this modification potentially attractive for applications (Dávalos-Orozco, 2007). Evidence comes mostly from the analysis of models of reduced dimensionality that exploit a long-wave expansion, whereas the available data are relatively scarce. Most importantly, given the multi-parameter nature of the problem, the extent and the parametric variation of such an effect is presently unclear, and in some cases evidence appears contradictory. The problem may become even more intriguing by consideration of other physical effects, resulting from the addition of surfactants (Pozrikidis, 2003) or the application of electric fields (Tseluiko & Blyth, 2009; Tseluiko *et al.*, 2008), but these are beyond the scope of the present work.

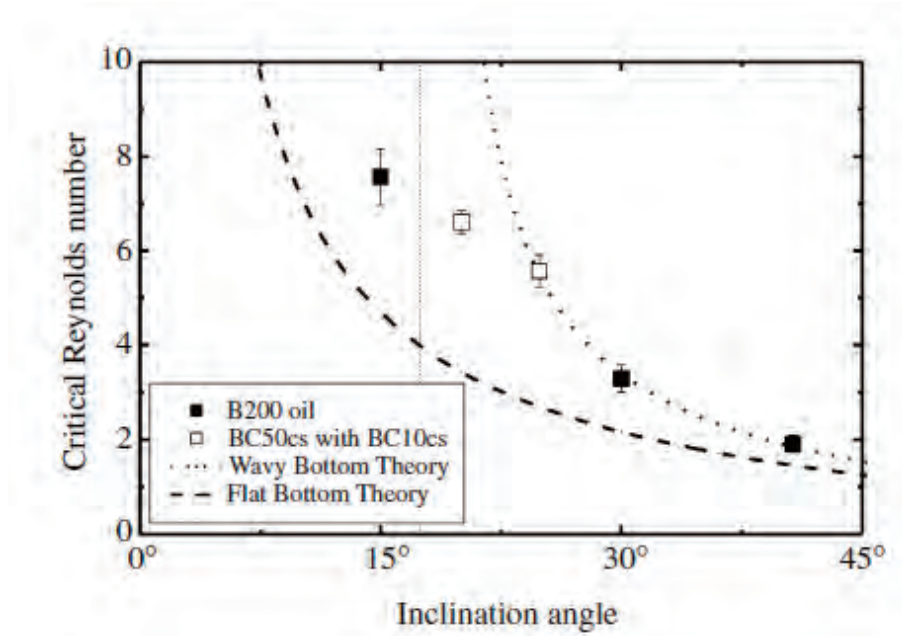


Figure 2.10: Minimum critical Reynolds number as function of the inclination angle obtained by Wierschem *et al.* (2005)

The first prediction of a stabilizing effect refers to a vertical wall with sinusoidal corrugations (Trifonov, 1998), and is based on a long-wave model derived by integrating in the normal direction an ad-hoc velocity profile (Integral Boundary Layer—IBL equation). Sometime later, based on experiments on a wall of orthogonal shape (consisting of symmetric step-ups and step-downs) with wavelength $l_b = 12$ mm and height $a_b = 0.4$ mm, Vlachogiannis & Bontozoglou (2002) reported that corrugation expands the stable regime by 20–30 % at small inclinations (1–8°) (figure 2.9).

A local linear stability analysis was carried out for film flow over moderate bottom steepness, which also shows a stabilizing effect (Wierschem *et al.*, 2003). However, the analysis is incapable to reproduce the resonance between the excited waves and the periodic bottom predicted by Bontozoglou & Papapolymerou (1997). Systematic experimental data were provided by Wierschem *et al.* (2005), for silicon oils flowing along a sinusoidal wall with wavelength of $l_b = 300$ mm and

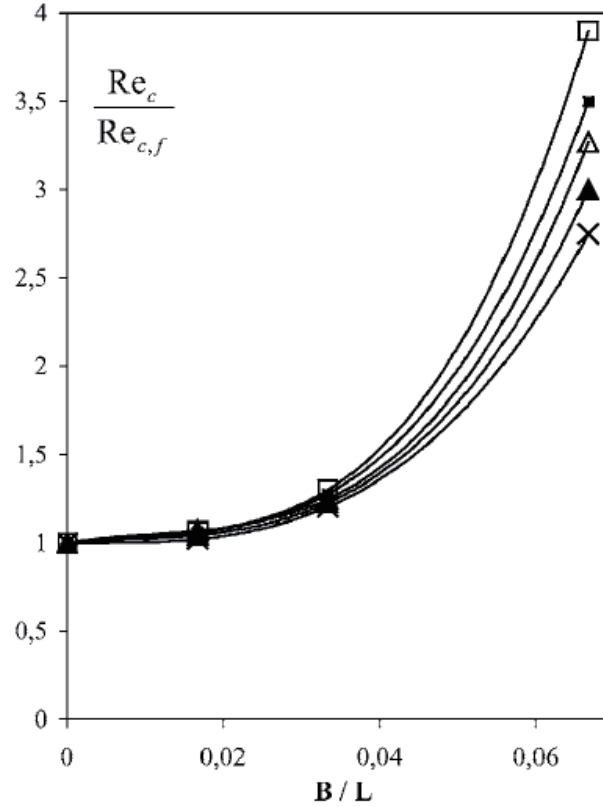


Figure 2.11: The ratio of the critical Re for a corrugated wall to the critical Re for a flat wall at the same inclination, as a function of wall steepness (Argyriadi *et al.*, 2006): (\times) $\varphi = 1.3^\circ$, (\blacktriangle) $\varphi = 2.6^\circ$ (\triangle) $\varphi = 3.4^\circ$ (\blacksquare) $\varphi = 5.4^\circ$ (\square) $\varphi = 7.4^\circ$

amplitude of $a_b = 15$ mm. These authors tested inclinations $15\text{--}45^\circ$ and showed that the sinusoidal wall always has a stabilizing effect in the experiment range. Their data, at high inclination angles, were in good agreement with the prediction by stability analysis of a pseudo-steady base flow (Nusselt solution at the local inclination), which is restricted to monotonously falling bottoms. It is interesting to note that the measured effect of inclination on the relative stabilization (Re_{cr}/Re_{flat}) exhibits in these data a discontinuity in slope: this ratio increases with inclination, until a maximum of the order of 100 % at $\varphi = 25^\circ$, and then drops again, forming a cusp at the maximum (figure 2.10).

Argyriadi *et al.* (2006) extended the experiments for their orthogonal wall

to cover three different heights in order to study the effect of wall steepness, $A_b = a_b/l_b$. The stabilizing effect, which can be expressed as ratio Re_{cr}/Re_{flat} , was found to increase with inclination in the range tested ($1-8^\circ$), and to grow as the cubic power of A_b , exhibiting for the highest wall an increase in the order of 200–300 % (figure 2.11). The above represent practically all the experimental evidence that is presently available.

More recently, there has been an outburst of numerical and mainly theoretical work on the problem. The paper by Trifonov (2007) is unique, in which it solves full Navier-Stokes equations for a vertical sinusoidal wall, and uses Floquet theory to predict the linear stability of these solutions. In his paper, stabilities of steady flows with respect to spatial perturbation of various wavelengths are investigated. An interesting prediction is that the flow may remain stable even up to $Re = 10-20$ with sufficiently steep corrugations in a range $L_b = 1-5$, and that stability also depends on surface tension (Kapitza number). Though not thoroughly discussed by the author, his calculated eigenvalues indicate the possibility of unstable short-wave modes.

Evolution equations for film over corrugation are stemmed from those of flat substrate. Dávalos-Orozco (2007) derived a Benney-type equation and investigated numerically its temporal behaviour by introducing local pressure fluctuations of desired frequency on the free surface. He predicted that, with appropriate choice of the wall wavelength, traveling disturbances decline and even disappear, under conditions that would lead to growth had the wall been flat.

Oron & Heining (2008) derive a first-order, long-wave model by substituting the ad-hoc imposition of a parabolic velocity profile by the systematic weighted-residual technique originally advocated by Ruyer-Quil & Manneville (2000) (Weighted Residual Integral Boundary Layer—WRIBL equation). They predict that, with increasing Re , the steady free surface deformation first gives in to a time-periodic oscillation in amplitude and phase, and later to traveling waves.

Although most studies show that wall corrugations will impose a stabilizing

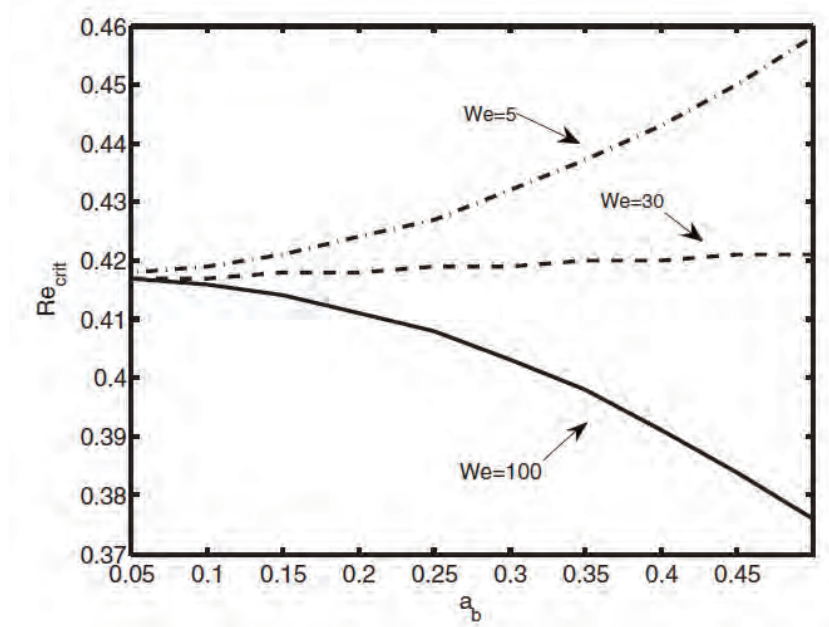


Figure 2.12: Critical Reynolds number VS bottom amplitude with $\cot\varphi = 0.5$ and $\delta = h_N/l_b = 0.1$ (from D'Alessio *et al.*, 2009)

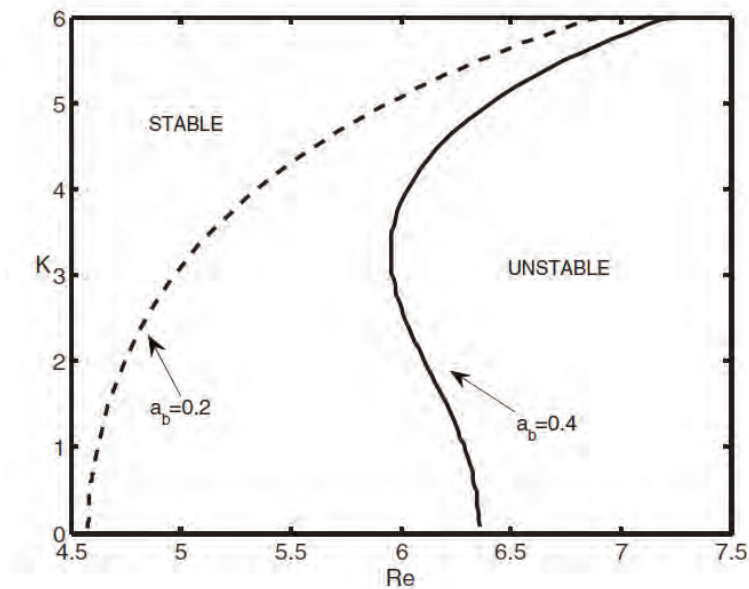


Figure 2.13: Neutral stability curves for the case with $\cot\varphi = 0.5$, $We = 5$, and $\delta = h_N/l_b = 0.1$ (from D'Alessio *et al.*, 2009)

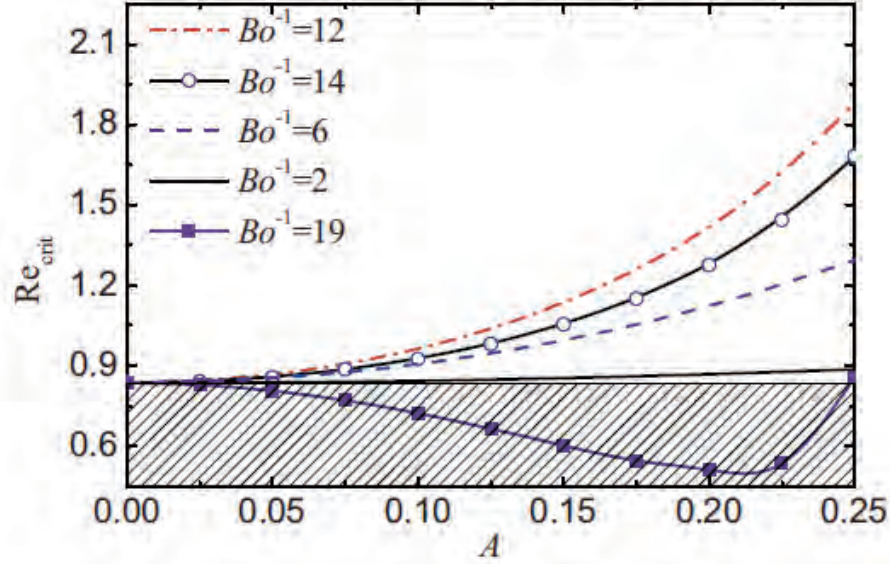


Figure 2.14: Critical Reynolds number VS free surface amplitude ($A = a/d$) at different inverse Bond numbers. $\cot\varphi = 1$ and $\delta = 0.2$ Heining & Aksel (2009)

effect and expand the stable regime, there are some computation work predict a destabilizing effect at some conditions. D'Alessio *et al.* (2009) derived a second-order, WRIBL model. They predict for the first time that a corrugated wall may destabilize the flow when the Weber number is large enough ($We \sim 10^2$) and at the same time the film is thick enough (Nusselt film thickness, $h_N > 0.1 l_b$). In his study, the role of surface tension on instability was investigated: bottom topography tends to stabilize the flow under condition of moderate surface tension; however, for relatively strong surface tension, bottom undulation may destabilize film flow if the wavelength is sufficiently short (figure 2.12). Another interesting prediction is concerned with the wavelength of the perturbation. It is well know that film flow is first destabilizing by long-wave disturbance for flat substrate. However, when above undulated substrate, film flow can first be destabilized by shorter wavelength of disturbance if film thickness is sufficient small compared with amplitude of wall corrugation (figure 2.13).

According to the prediction by D'Alessio *et al.* (2009), the effect of the cor-

rugation height however remains monotonic, and always enhances the deviation from the flat wall prediction. These results are strengthened by similar predictions from Heining & Aksel (2009), who investigated the problem reversely, seeking for the corresponding wall substrate for a given free surface shape by weighted-residual integral boundary-layer method. The instability of film flow is studied by treating the computed wall substrate profile as a starting point of direct problem. The result of critical Re changing with the free surface deformation at various Bo^{-1} was shown in figure 2.14. The Bo^{-1} is inverse Bond number, which is defined as:

$$Bo^{-1} = \left(\frac{2\pi d}{l}\right)^2 \left(\frac{\sigma}{\rho g d^2 \sin\varphi}\right) \quad (2.15)$$

Here, l and d correspond to the wavelength of the free surface and mean film thickness respectively. In the range of small and moderate surface tensions ($Bo^{-1} \leq 14$), increasing surface amplitude results in a monotonic increase of critical Re . However, under the condition of strong surface tension ($Bo^{-1} = 19$), the effect is more complicated: with increasing free surface deformation, a destabilizing effect with increasing extent was first observed, after which the critical Re starts to increase and end up with a value higher than the theoretical value for flat substrate, indicating a reverse to stabilizing effect.

Häcker & Uecker (2009) derive a WRIBL equation in a curvilinear coordinate system following the wall, and show that their model works satisfactorily even under conditions that correspond to extensive flow separation at the trough. A most interesting prediction is that the effect of wall steepness may be non-monotonic, i.e. it may first stabilize and later destabilize the film (figure 2.15). They also predict that, with increasing steepness, the dominant instability shrinks in wavelength, going from infinite to that of the wall. Nguyen & Plourde (2011) also derive a WRIBL equation working in a coordinate system that follows the wavy wall, and investigate the effect of inclination angle on the ratio of free-surface to solid wall area.

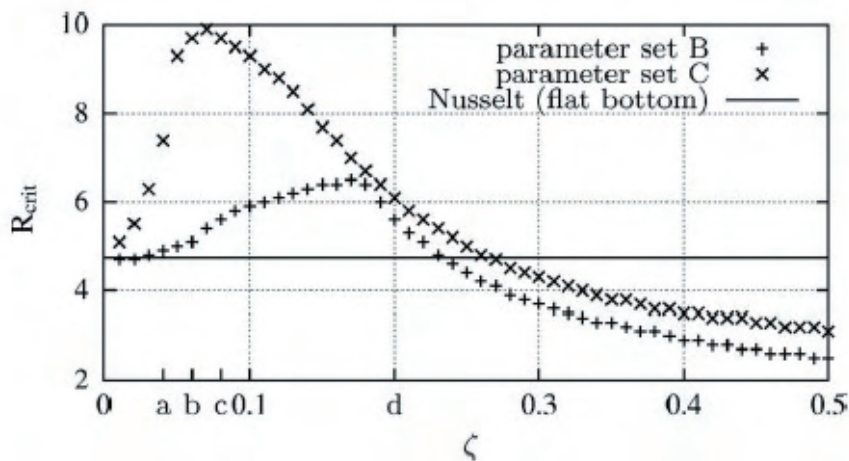


Figure 2.15: Critical Reynolds number R_{crit} as a function of the waviness, ζ (Häcker & Uecker, 2009)

2.3 Overview of techniques for film thickness measurement

The thickness of film is the primary characteristic parameter for film flow. For some circumstances in which the film flows are uniform and steady, the thickness can be readily obtained: For instance, in the case of a steady two-dimensional films over inclined plane, the film thickness can be calculated easily from the average flow rate, which can be determined by hold-up measurement. However, average thickness is insufficient for the non-uniform film or films with interfacial traveling waves. Extensive methods have been developed over the decades, which are reviewed by a number of authors (e.g. Alekseenko *et al.*, 1994; Clark, 2002; Hewitt, 1978). Based on the localization and/time response, the measurement techniques can be classified as film average methods, localized method and spatial method, shown in table 2.1. In the following section, some of the most widely applied techniques for film thickness will be discussed.

2. Literature Review

Table 2.1: Summary of measurement techniques of film thickness

Film Average	Localised (Point)	Spatial
Hold-up Measurement	Conductance(Capacitance) Probes	Photographic Light Absorption
Film Conductance Method	Needle Contact Probe	Multiple Electrode Probes
Weighing Method Radioactive	Absorption (Emission)	Multi-Conductance Probes
	Shadow Method	Pigment Luminance Method
	Acoustic Method	Fluorescent Imaging
	Ultrasonic Pulse-Echo Method	Ultrasonic Transmission
	Fluorescent Techniques	Photographic Image Processing
	Interferometric Methods	
	Laser Scattering Method	
	Light Absorption Techniques	

2.3.1 Contact Method (Need-contact method)

The film thickness is determined by the position of the needle point at the moment of contact with the free surface. The contact moment is registered either visually (observing menisci) or electrically, based on closing the electric circuit between the needle and conducting wall (Alekseenko *et al.*, 1994). Applications of the needle-contact method in film thickness are presented by e.g. Ishigai *et al.* (1972), Takahama & Kato (1980), Nosoko *et al.* (1996). This technique can accurately measure the localized film thickness of a steady flow, but it is incapable to perform measurements of continuous film thickness variation. Therefore, nowadays, it is mainly used as a calibration or comparative device for some other measurement techniques.

However, the contact method can provide statistical information concerning the distribution of instantaneous film thickness. The needle is originally placed above the surface of liquid film, and gradually moved closer to the substrate. At first, the wave in the liquid surface makes discontinuous contact between the probe tip and liquid. The contact will be permanent when the probe tip reaches the minimum film thickness (wave-trough). Thus, the film thickness probability distribution could be obtained by recording the time fraction of the probe tip keep contacting with the film. The accuracy of this method is related to the wettability of the needle. The most serious difficulty in application is the uncertainty of contact hysteresis: It may be possible for the needle to remain in extended contact with the film by “dragging out” a filament of liquid (Alekseenko *et al.*, 1994; Hewitt, 1982).

2.3.2 Conductance Probe Technique

The most widely used measurement technique for film thickness on film flow is conductance probe technique, which is based on the electric conductivity of the liquid. The conductance is measured between two electrodes, which are usually

set flash with the wall. The wall surface between two electrodes has to be insulating, typically of thermosetting resin or Perspex glass. A small amount of salts (NaCl/KCl) is added into the liquid to increase the specific conductivity. In the range of small film thickness (relative inter-electrode distance), the calibrated dependence is linear. The voltage signal received can be converted to film thickness using the calibration data, as following,

$$h = aV + b \quad (2.16)$$

where h is the film thickness, V is the output voltage, a and b are the coefficient to be determined by calibration. The calibration is done by recording the signal for film with known thickness, which is measured by alternative technique or calculated theoretically.

Alternating current (A.C.) signal frequency (1–100 kHz) is supplied to the electrodes of the probes. The lower limit is restricted by the potential polarization effect in a long term and also the phase of the admittance of the electrolyte; while the upper limit is restricted by the effect of stray capacitances (Brown *et al.*, 1978; Kang & Kim, 1992). The value of the voltage at the probe should be below the decomposition potential.

A wide variety of probe geometries have been employed in the literature. Detailed description of considerations in probe design will be presented in Chapter 3. Due to the simplicity and accuracy, the conductance probe is still widely applied in film thickness measurement in film flow or multi-phase flow. Moreover, a number of variations of conductance probes have been developed over the years for their specific purposes (e.g. Fossa, 1998; Kim *et al.*, 2009; Prässer *et al.*, 1998; Rajagopalan *et al.*, 1998).

2.3.3 Fluorescence imaging method

In order to investigate the spatio-temporal dynamics for the film flow, fluorescence imaging method was first employed by Liu *et al.* (1993) and later developed by Vlachogiannis & Bontozoglou (2001, 2002). As shown schematically in figure 2.16, the film flow is illuminated by a UV light source that is placed on the top of the channel and is captured by a CCD camera below the transparent channel. The fluid is doped with a small concentration (about 100–300 ppm) of fluorescence dye (e.g. $C_{20}H_{10}O_5Na_2$), which will fluoresces under UV light and also keeps the physical properties of the fluid unaffected. The CCD camera is typically mounted with optical filters (e.g. green band pass filter) to remove the background UV light and leave only the radiation light from the fluorescence. The light intensity in the image plane $I(x, y, t)$ is proved to be satisfactorily represented as a linear function of film thickness $I(x, y, t)$, as following,

$$I(x, y, t) = a(x, y)h(x, y, t) + b(x, y) \quad (2.17)$$

The two linear coefficients, $a(x, y)$ and $b(x, y)$, depend on the concentration of dye, the fluid solution, the surface roughness of wall plate and light source. Therefore, a and b values have to be calibrated for each pixel of the digitized image.

The calibration is usually performed in situ at the steady state of film flow, when the film thickness is known as the Nusselt film thickness (equation 2.10). An alternative method is to use contact needle method to measure absolute film thickness in the steady state, which can also be applied for verification. The measurement rate depends on the frame grabber, typical of the speed up to 15 frames per second. This method shows reasonably good accuracy in the literature. Vlachogiannis & Bontozoglou (2001) reported that the linear relation is found satisfactory (accurate to within 2–5%) for film thickness in the range of 0.2–2.0 mm. However, when employed to film over corrugated substrate, the technique is straightforward only on orthogonal corrugation. An abnormal reflection was

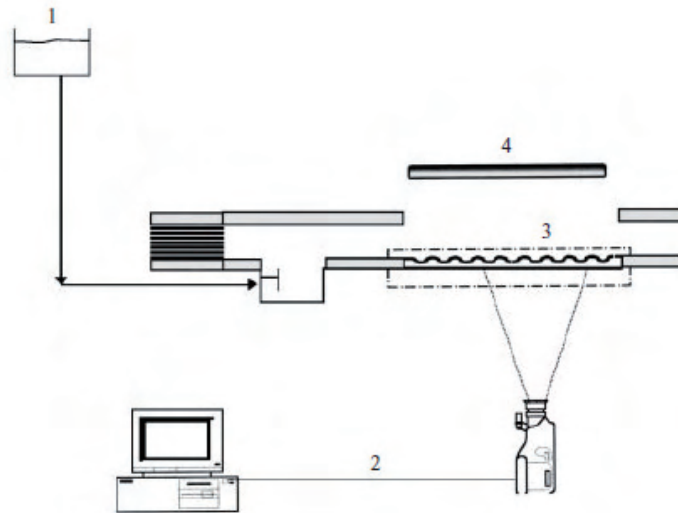


Figure 2.16: Sketch of the experimental apparatus: 1, overflow tank; 2, image grabbing system; 3, corrugated wall; 4, UV light source (Vlachogiannis & Bontozoglou, 2002)

reported, when attempted to perform on sinusoidal corrugation (Vlachogiannis & Bontozoglou, 2002).

2.3.4 Laser-induced fluorescence method

Laser-induced fluorescence method (LIF) has gained popularity as a general-purpose visualization tool for its numerous applications in the recently years. It was also adapted for film thickness measurement by a number of authors (e.g. Desevaux *et al.*, 2002; Hidrovo & Hart, 2001; Schubring *et al.*, 2010). Same as fluorescence imaging method, it is also based on the photo-excitation of fluorescent dye, but has the advantage of capturing movement with much smaller time interval (μs), since the flow can be visible only when the laser is triggered (typically two laser are installed in the system, and can be triggered in small time interval). A small concentration of fluorescence dye, which has an optical resonance wavelength as the laser, is introduced into the liquid. When illuminated by the laser, the dyes will yield fluorescent light of longer wavelength, which can

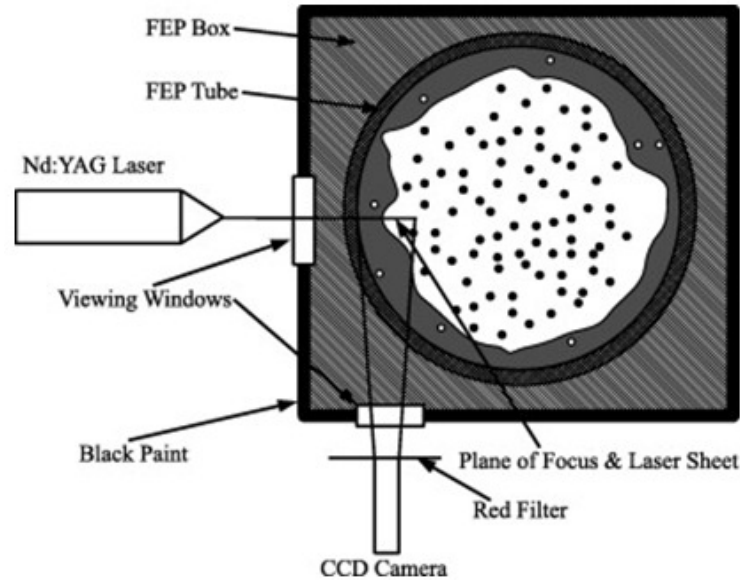


Figure 2.17: A example of test section for PLIF measurements from Schubring *et al.* (2010)

be recorded by a high-speed CCD camera set perpendicularly. A filter, which has same transmission wavelength as the emission light, is mounted on the camera, in order to get rid of spurious light. The illuminated area appears as bright region in the image, which can be further processed to obtain film thickness value. An example of test section is shown in figure 2.17 (Schubring *et al.*, 2010), where the LIF system is employed for film thickness measurement of annular flow in a tube.

2.3.5 Photographic image processing

The measuring principle of photographic image processing is similar to laser-induced fluorescence method: it also based on processing of images of the flow field. The flow is illuminated by a light source (or a laser system), and captured by a CCD camera which is set perpendicular to the flow field. The free surface profile and the film thickness can be readily determined by processing the resulting image, within pixel resolution.

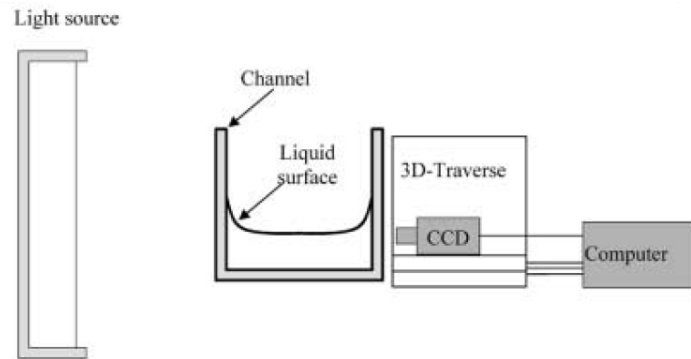


Figure 2.18: A sketch of experiment apparatus from Wierschem *et al.* (2002)

The calibration can be done by counting the number of pixels for a known distance. In order to increase the resolution, usually, a microscope objective is mounted to the camera. This method was employed by Negny *et al.* (2001), for the determination of free surface profile of film over a vertical column, and by Wierschem *et al.* (2002, 2003) for measuring the thickness of film flow over inclined channel (figure 2.18). In the current project, it was also implemented in the study of film over vertical cylinder.

Chapter 3

Experimental Setup and Problem Definition

This chapter mainly presents the experimental apparatuses and measurement techniques employed in the current project. Detailed descriptions of two experimental facilities are provided in section 3.1. As a general tool in the project, conductance probe technique including a classical method of detecting the instability threshold is introduced in section 3.2. In section 3.3, the principles of an alternative measurement technique, photographic image processing, is presented. In the last section, the problem definition, including the main parameters and non-dimensional terms used in the dissertation, are provided.

3.1 Experimental facilities

3.1.1 Description of the inclined film setup

The experiments of inclined film flow over corrugation are performed in an existing apparatus in the lab, which is shown schematically in figure 3.1. The set-up consists of four main components: an elevated overflow tank (1), the main channel (12), a collection tank (7) and data acquisition system. The overflow tank is

3. Experimental Setup and Problem Definition

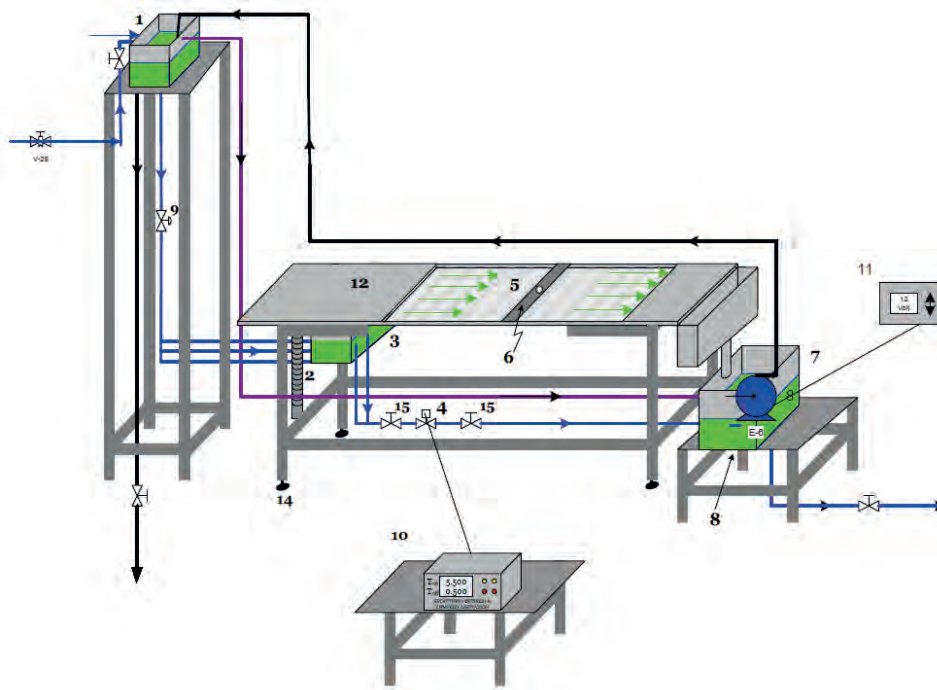


Figure 3.1: Schematic diagram of inclined film flow channel

placed around 2.5 m high, which can provide sufficient pressure to maintain the flow. Flow rate is adjusted by a manually controlled valve (9), and determined by measuring the volume of liquid flowing out of the channel over a known period of time. From the overflow tank, the fluid is directed by three elastic tubes to the distributing head and enters the main channel smoothly. The main channel (12) has a length of 800 mm and width of 250 mm. The bottom part (5) of the main channel is removable, where different wall substrates (length: 500 mm; width: 250 mm) can be accommodated. The whole channel is made of Plexiglas, so that flow visualization can be applied. The collection tank (7), which contains a submersible pump, is isolated from other components of the experimental device, in order to minimize transmission of vibrations. The liquid in the collection tank (7) is pumped back to the elevated overflow tank (1). The entire apparatus is mounted on rubber sheet to reduce the influence of vibration. The inclination of the channel can be adjusted ranging from 0–48°, through a threaded rod (2).

3. Experimental Setup and Problem Definition

A perturbation system was installed in the channel, which controls an on/off electronic valve (4) that is located at a bypass exit below the distributing head. When this valve is closed, the flow that used to exit from the bypass will be added to the main stream and serves as an external disturbance. The magnitude of the disturbance can be adjusted by a valve at bypass, while the extent of each disturbance depends on the time duration of the flow surge, which is varied in the range 0.2–2.0 s. This system can generate disturbances with a range of frequencies up to 4 Hz.

Another important factor worth attention, during the experiments, is the alignment of the channel. This can be checked by introducing a two-dimensional wave at or close to steady state (no three-dimensional wave is developed), and observe the evolution of the wave downstream. The channel is inclined in the transverse direction, if the wave downstream is no longer symmetrical along the centerline. The alignment can be realized by adjusting the supports (12) at bottoms of the legs. The support at each leg can be screwed into the leg, which in turn changes the height at that location. This check has to be done every time after changing inclination angles or occasionally, when someone moves the channel.

3.1.2 Description of the falling film set-up

A new experimental apparatus was built during the project, in order to extend investigation of inclined film flow to a vertical wall. The experimental set-up is a closed hydrodynamic loop consisting of the test section (1), a collection tank (2), a gear pump (3) and a flow distributor (4), as shown in figure 3.2. Liquid from collection tank is pumped to the distributor that is placed at the top of the test section, then supplied into an interior compartment of the test section. The fluid is then supplied on the external surface of the test section by overflow from the interior compartment. Some porous material is used to equalize the resistance to flow circumferentially, and the exterior of the ridge is rounded in order to avoid

3. Experimental Setup and Problem Definition

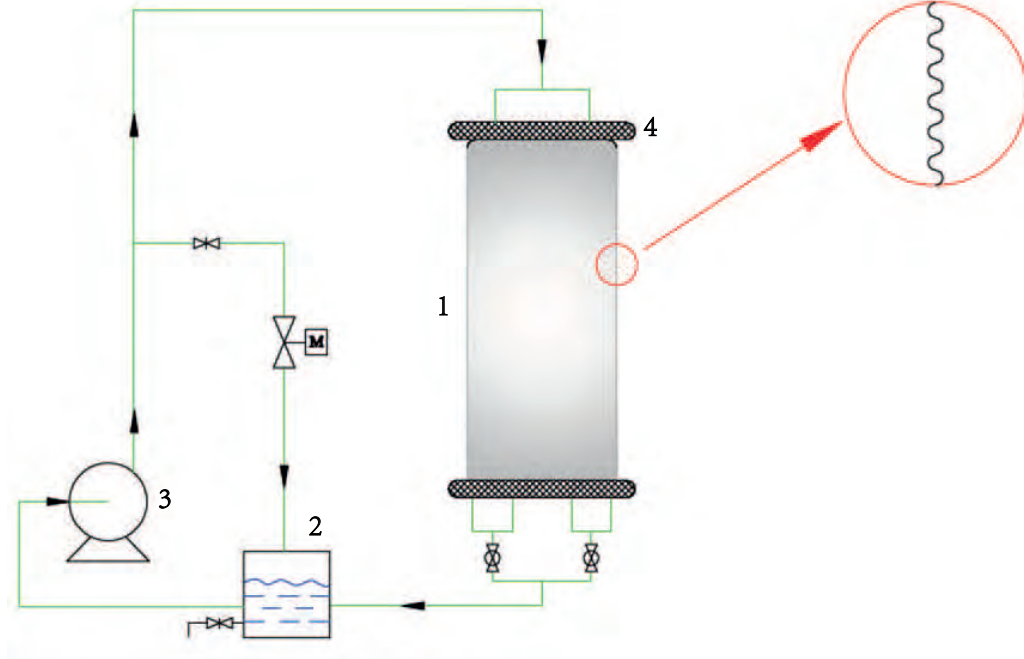


Figure 3.2: Schematic diagram of the falling film set-up

Table 3.1: List of dimensions of available cylinders

Column	Diameter (mm)	Shape	Wavelength (mm)	Height (mm)
1	282	Flat	N/A	N/A
2	282	Sinusoidal	4 mm	1 mm
3	231	Sinusoidal	12 mm	2 mm
4	231	Orthogonal	12 mm	2 mm

perturbation introduced by the sharp corner. The liquid from the test section is collected and flows back to the collection tank.

The test section is a one meter-long cylinder made of polyamide, whose surface has been shaped with periodic corrugations. Test sections with two diameters and various geometries of surface corrugation, were manufactured, as listed in table 3.1. A crucial point regarding experiments is to make sure the column is vertical and achieve circumferential uniformity of the flow. The vertical adjustment can be realized though four screws at bottom of the test section and measured by a

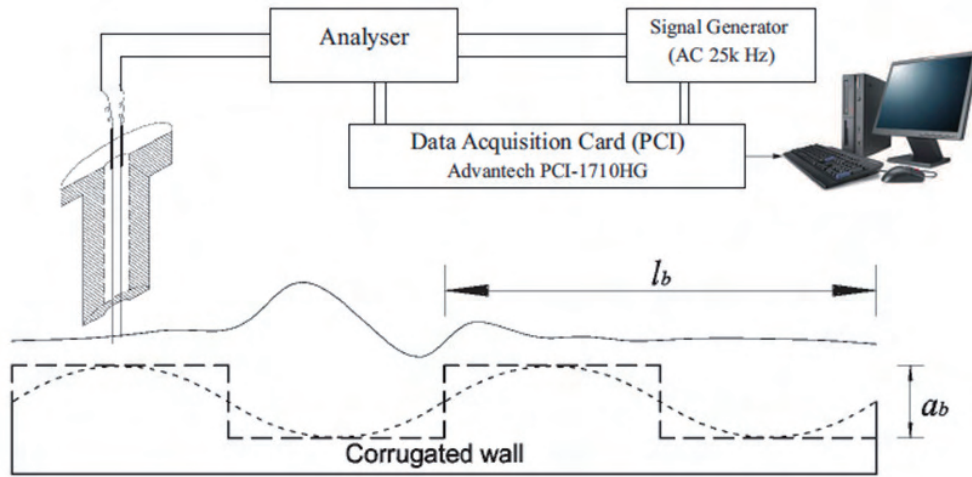


Figure 3.3: Schematic diagram of conductance probe method

cathetometer.

3.2 Conductance Probe Method

The instantaneous thickness is the most important parameter to be measured for film flow. Several measurement techniques have been reviewed in chapter 2. In current study, two measurement techniques are implemented in the experiments: conductance probe method and an optical method based on direct photography. In this section, conductance probe method will be discussed, while the principle of the optical method will be introduced in the next section.

3.2.1 Description of the technique

As discussed in section 2.3.2, this technique is based on the fact that the resistance (conductance) of film is proportional to its thickness. Due to its simplicity, it is one of the most widely applied techniques in film thickness measurement. Figure 3.3 is the schematic diagram of the main components of the technique. The conductance probes are placed at the locations where we plan to measure

3. Experimental Setup and Problem Definition

(typically one at upstream and one at downstream for detection of instability threshold), and are connected to an analyzer circuit. A signal generator produces input sine signal at a frequency of 25 kHz, and the response is converted to an analog signal by the analyzer. This analog signal is then collected and logged by a data acquisition card, converted to digital signal and fed into computer. The data acquisition card used is PCI-1710HG board, which allows 16 channels connection from instruments to the board. The digital signals could be converted to readable data and saved in EXCEL spreadsheets or text file by Labview software in the computer. Using Labview software, it is possible to set the sampling frequency and recording period of the measurement. In the investigation of film flow, the typical sampling frequency were set to 800 Hz, which is sufficient to capture the characteristic of waves ($0 \sim 20$ Hz). The time period of measurement is usually set to 60 s, in which 48 000 values are recorded. Evidently, the liquid has to be conductive in order to apply the method. Thus, a small concentration of salt ($< 1\%$), which will not change the liquid properties, is added to the liquid to increase its conductivity.

3.2.2 Probe geometry

An important consideration in conductance probe technique is the geometry of the probes. Various geometries of conductance probes have been applied in the literature. In general, they can be mainly classified into two large categories: one is a flush-mounted type, the other is parallel-wires conductance probe (figure 3.4). There is an alternative design combining the two types, in which one electrode is set flush with the wall and the other electrode is a wire vertically inserted from the top side (Kang & Kim, 1992).

For the types of flush-mounted and parallel-wire, an important geometric parameter is the distance between the two electrodes, since the measured resistance of the probe is based on a region around the electrodes whose area strongly depends on the spacing of electrodes (e.g. Coney, 1973; Koskie *et al.*, 1989). In case

3. Experimental Setup and Problem Definition

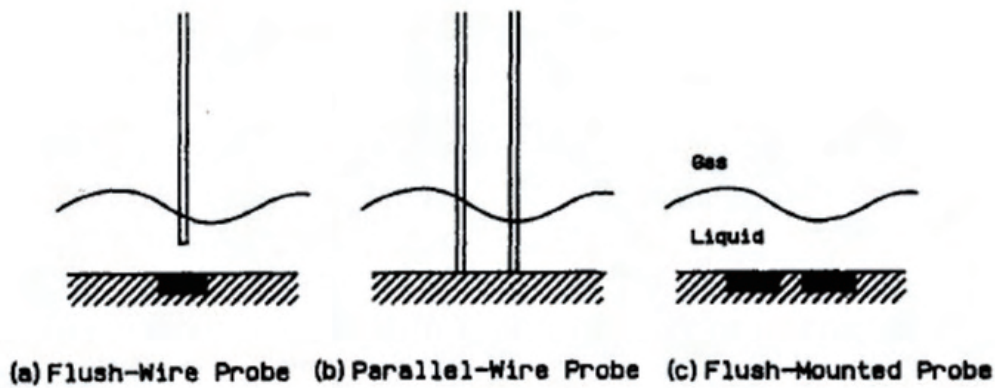


Figure 3.4: Schematic diagram of main types of conductance probes (Kang & Kim, 1992)

of wavy films, in order to increase the locality of measurement, smaller spacing is preferred.

The flush-mounted probes, namely, are set flush with the channel surface. It will be flat on planar channel and curved in a pipe. The advantage of this type is that the probe will not disturb the flow. However, there is a limitation for its application, because, as the film goes sufficiently thick, the probe gradually loses its sensitivity (signal no longer linearly proportional to thickness). Although the measurement range can be extended by increasing the spacing between the electrodes, this is at the cost of losing locality. Since the film thickness measured by the probe is an average value between the electrodes, closely spaced electrodes are preferred in order to obtain more localized response. This point is evidently very important in the case of a wavy film, where film thickness varies according to the steepness of the wave. Some experimental investigations have shown that the conductance probe can detect a wave shape satisfactorily when its wavelength exceeds five times the electrode spacing (Alekseenko *et al.*, 1994). Thus, there is a compromise between localized measurement and measurement range.

The parallel-type has two wires (strips) crossing the film. For probes of this type, there is no saturation in the response signal, which leads to much larger

3. Experimental Setup and Problem Definition

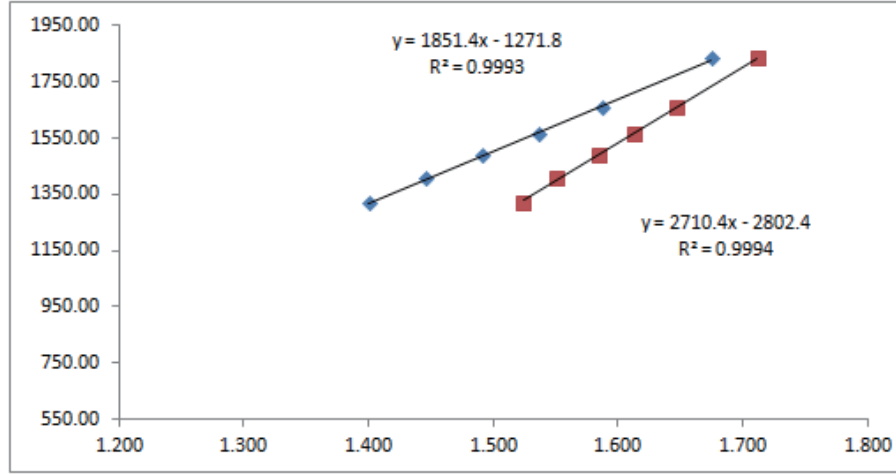


Figure 3.5: Calibration data of 60% glycerol on a corrugated wall ($\varphi = 3^\circ$, $l_b = 12$ mm, $a_b = 1.6$ mm)

measurement range. An obvious disadvantage is that, to some extent, especially when the flow rate is large, the film will be disturbed by the wires. Thus, it is important to use thin wires in order to minimize their effect on the flow. Some researchers have attempted to quantify the effect of the wires, and found out that, if the wires are thin enough, the interfacial phenomena caused by them, such as meniscus, bow waves and wakes, are negligible. On the other hand, the wires cannot go thinner without limitation, since the electric resistance of the wire must be much smaller than that of the liquid. Parallel wires probe, whose design gave reasonably good responses in the past experiments (Vlachogiannis *et al.*, 2010), was selected in the experimental work. Each probe consists of two parallel chromel wires, 0.4 mm in diameter, separated by an axis-to-axis distance of 2 mm.

3.2.3 Calibration method

Some studies are trying to calibrate the probes theoretically, by finding the exact relation between film conductance and thickness. However, in real measurement, this method need to maintain the conditions of liquid and probes precisely, which

3. Experimental Setup and Problem Definition

is very difficult.

In current experiments, the probes are simultaneously calibrated in situ by taking measurements of the output voltage in the stable flow regime (without disturbances) and calculating the film thickness from the Nusselt solution:

$$h_N = \frac{3Re\nu^2}{g\sin\varphi} \quad (3.1)$$

Since output voltage of the probe varies linearly with the Nusselt film thickness, the linear relation can be determined by interpolation of a set of recorded voltages and calculated Nusselt solutions, as shown in figure 3.5. Thus, the voltage signal received can be converted to film thickness using the calibration data, as following expression:

$$h = aV + b \quad (3.2)$$

where h is the film thickness, V is the output voltage, a and b are the coefficient to be determined by calibration.

3.2.4 Determination of marginal stability

An important goal in the project is to investigate the effect of corrugation on the primary instability. Liu *et al.* (1993) first proposed a method for detecting the primary instability of film flow. Time series of local wave slope at two different locations along the flow is measured based on reflection of laser beams by the liquid surface. For a given Reynolds number, which is expected to be above the critical value, disturbances of varying frequency are consecutively introduced until a cutoff frequency is found, beyond which the spectral power of the time series of wave slope detected declines from the first to the second measuring location. This procedure is repeated for different Re , and all those cutoff frequencies are interpolated to determine the theoretical critical Re at zero frequency. Similar technique based on laser beam reflection was implemented by some other authors (Pollak *et al.*, 2011; Wierschem *et al.*, 2005), with simplified procedure

3. Experimental Setup and Problem Definition

of detecting the threshold. They were comparing the amplitude of a traveling disturbance at two locations along the channel: The flow is considered as stable when the amplitude decreases along the channel; in contrast, the flow is unstable when the amplitude of disturbance is observed larger downstream. The critical Re is recognized if the amplitude is the same.

Vlachogiannis *et al.* (2010) developed a less tedious procedure using conductance probe method to detect the onset of interfacial instability with reasonable accuracy (better than 5%). This method was adopted and implemented in current experiment in order to detect threshold of the classic long-wave instability. For the threshold of short-wave instability, which will be discussed detailed in chapter 4, a more appropriate method, based on the standard deviation (STD) of the signal is developed. In the following section, detection of long-wave instability will be presented.

Disturbances with very low frequency ($f = 0.167$ Hz), which practically coincides with theoretical long-wave disturbance, were introduced at inlet of the channel. Multiple conductance probes (at least two) are installed along the centerline of the channel to measure the local film thickness at different locations. By comparing the time-series of film height, the evolution of the low frequency disturbance can be obtained.

A typical example of time-series at various Re is shown in figure 3.6, corresponding to an orthogonal corrugated wall ($l_b = 24$ mm, $a_b = 0.8$ mm) at inclination of $\varphi = 25^\circ$. The green lines represent the signals obtained from the upstream probe, while the red lines represent the signal from downstream. The humps in the time-series are the disturbances, which are introduced periodically at frequency $f = 0.167$ Hz. As can be seen from the figure, for the first five values of Re , the amplitude of disturbance at downstream is smaller than those at upstream, which indicates that the film flow is stable. For the condition $Re \geq 3.69$, which is unstable in this case, the disturbance is amplified downstream, and gradually breaks into shorter waves. Thus, it is natural to infer that the critical Re lies in

3. Experimental Setup and Problem Definition

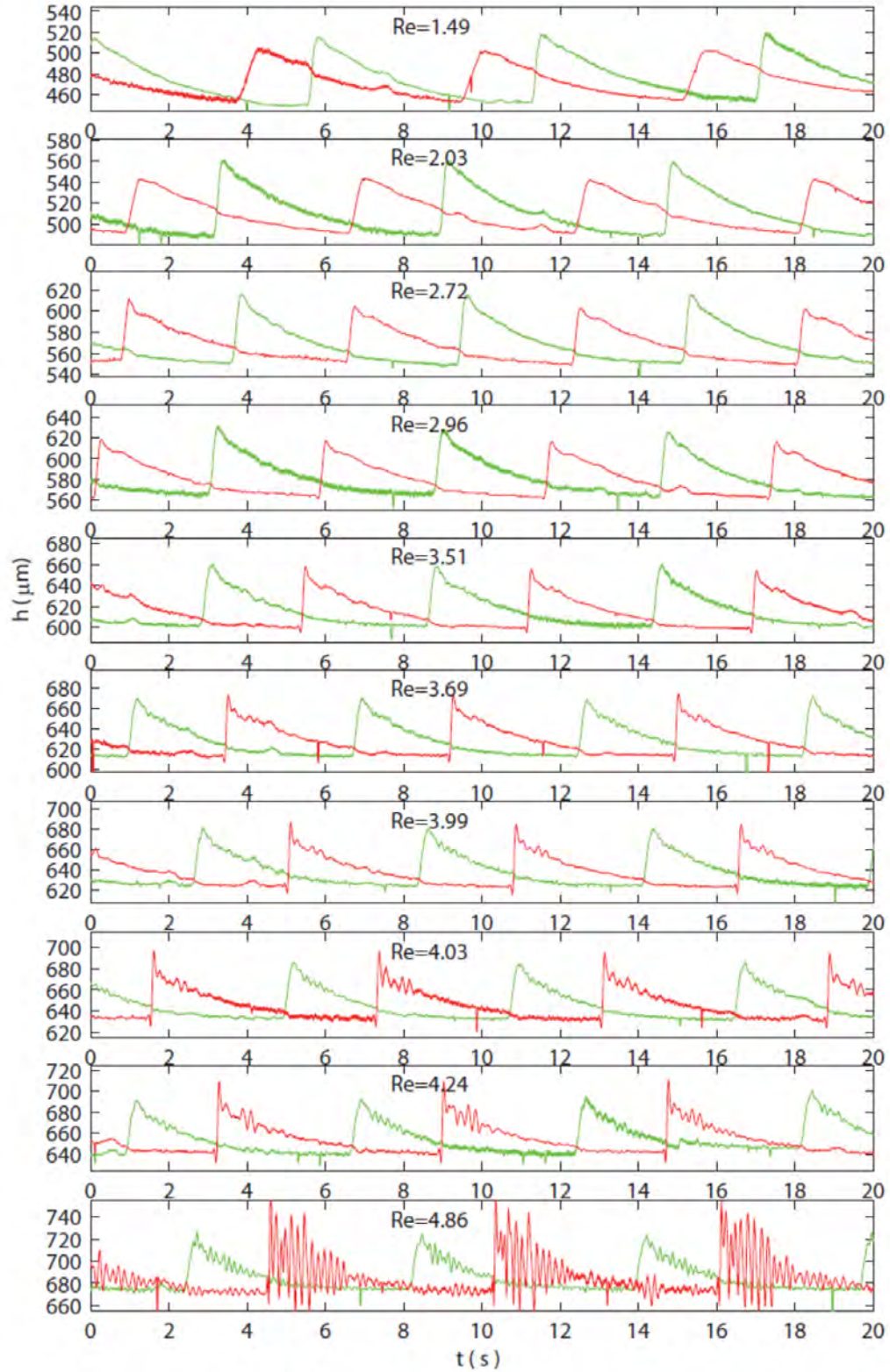


Figure 3.6: Time series of film height for a 60 wt % glycerol solution at various Re ($l_b = 24$ mm, $a_b = 0.8$ mm, $\varphi = 25^\circ$).

3. Experimental Setup and Problem Definition

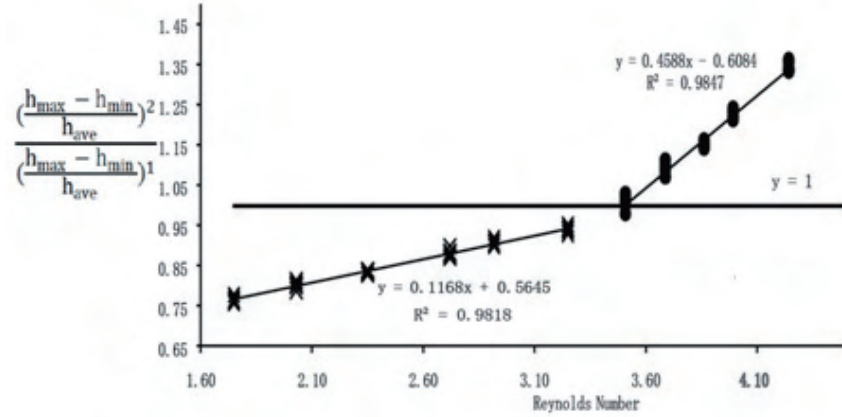


Figure 3.7: Determination of marginal stability ($l_b=24$ mm, $a_b=0.8$ mm, $\varphi = 25^\circ$, 60 % Glycerol solution)

the range of $3.51 < Re < 3.69$.

In order to determine the instability threshold accurately, a quantitative determination method followed by Vlachogiannis *et al.* (2010) is employed. It is based on the observation of the parametric evolution with Re of the ratio of downstream to upstream wave heights. The wave heights are normalized with the measured mean film thickness at respective probe locations. Two characteristics facilitate reliable determination of the threshold: 1) theoretically, the ratio should be lower than one when flow is stable and higher than one when it is unstable; 2) the rate of change with Re exhibits a jump when crossing the stability limit. Thus, the critical Re can be determined by the coincidence of three lines, which are the two linear interpolations before and after transition, and the horizontal line corresponding to ratio of one. In the case that the three lines do not cross at exactly the same point, the interpolation before the transition is neglected since it usually exhibits higher scatter. In the example shown in figure 3.7, the critical Re can be determined as $Re_{cr}=3.6$.

3.3 Photographic image processing methods

Similar to the work by Negny *et al.* (2001), the photographic image processing method is employed for the vertical cylinder. The optic system is originally designed for PIV measurements (TSI), and consists of a pulsed laser, a synchronizer, a CCD camera and a desktop installed with the control programme (Insight 3G). Instead of the laser, a lamp is used in the current study for illumination, since it is sufficient to capture the free surface profile, and at the same time avoids problems associated with stray light that stem from the refraction on the free surface of the laser beam reflected from the wall. Small concentration of fluorescence dye is introduced into the liquid to increase the visibility. The colour of the wall substrate is white, and the fluid is also shown as a bright area when illuminated by the lamp. Thus, in order to increase the contrast, a blackboard, which is placed with a distance from the cylinder (to make sure it is out of focus), is used as background.

The high-resolution CCD camera (Powerview TM Plus 4MP), which has 2048×2048 pixels, is set perpendicular to the edge of the test section of the vertical cylinder. A monochrome frame grabber board (Xcelera-CL PX4) is used to acquire and digitize the images up to a maximum speed of 16 frames per second. The images acquired are digitized at 2048×2048 pixels with 12-bit of resolution (deliver up to 4096 gray levels). A micro lens is used to increase the accuracy of the measurement.

The camera is controlled by the software Insight 3G provided by TSI company. The time interval of camera exposure is set to 500-1000 μs in the experiment, which is sufficient to capture the free surface variation. The image can be saved both in the RAM and hard disk, but usually, storage in the RAM is preferred, because it can increase the grabbing speed. The number of images that can be saved depends on the capacity of RAM. In our system, 242 images can be saved with single mode (one image frame is taken for each capture).

Restricted by the size of the CCD, there is a compromise between the length-

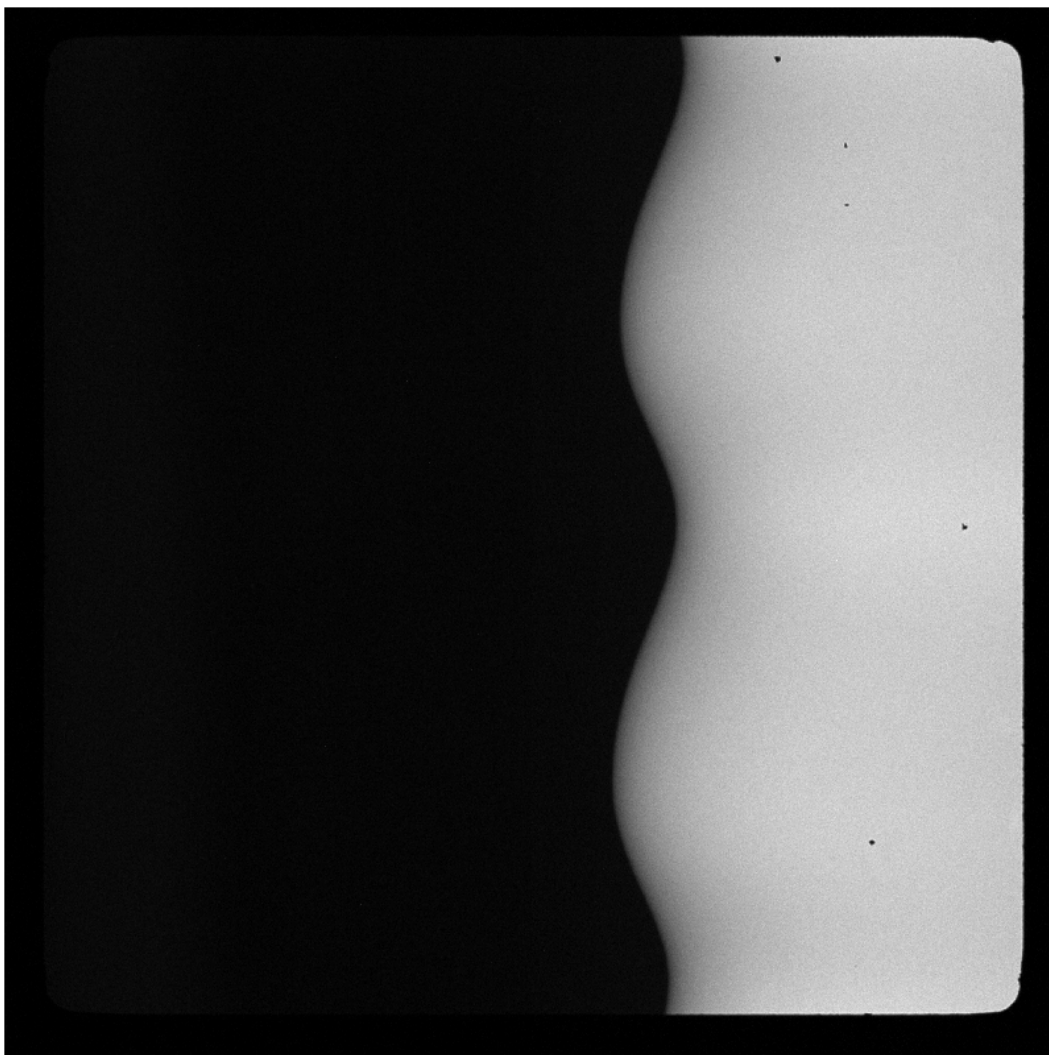


Figure 3.8: A example of raw image taken from the CCD camera.

3. Experimental Setup and Problem Definition

scale of measurement range and accuracy of the thickness measurement. If a relatively long part of the flow is fitted into the image, each pixel corresponds to a large area and leads to lower accuracy. On the contrary, if we focus on the small length, each pixel now corresponds to a smaller physical dimensions, and this improves the accuracy of the measurement.

A raw image, obtained from the system, is shown in figure 3.8. The left part, which shows black in the image, is the aforementioned background. The white area, which has a wavy interface with the background, is the left edge of the vertical cylinder. In this case, the cylinder is covered by a thin film, therefore, the interface of the black and white area is actually the free surface. Thus, the main goal is to detect accurately the location of this edge. The film thickness can be subsequently determined by subtracting in image of the cylinder without film flow. The processing of raw images and edge detection is done by MATLAB, and will be discussed in chapter 6.

3.4 Problem definition

The problem considered in the current dissertation is isothermal film flow over periodic corrugated substrates, including both inclined and vertical cases (figure 3.9).

The liquid used is aqueous glycerol solution. Its pertinent physical properties include kinematic viscosity ν , density ρ and surface tension σ . The advantage is that the viscosity can be adjusted easily according to its concentration, and the density and surface tension vary only slightly. The approximate physical properties of fluid are available as function of glycerol concentration. The latter is obtained by measuring the refractive index of the liquid, and referring to the refractive index-concentration table provided by the supplier (Appendix A).

More accurate values of physical are achieved by direct measurement of each parameter at the experimental conditions. The density of the liquid is measured

3. Experimental Setup and Problem Definition

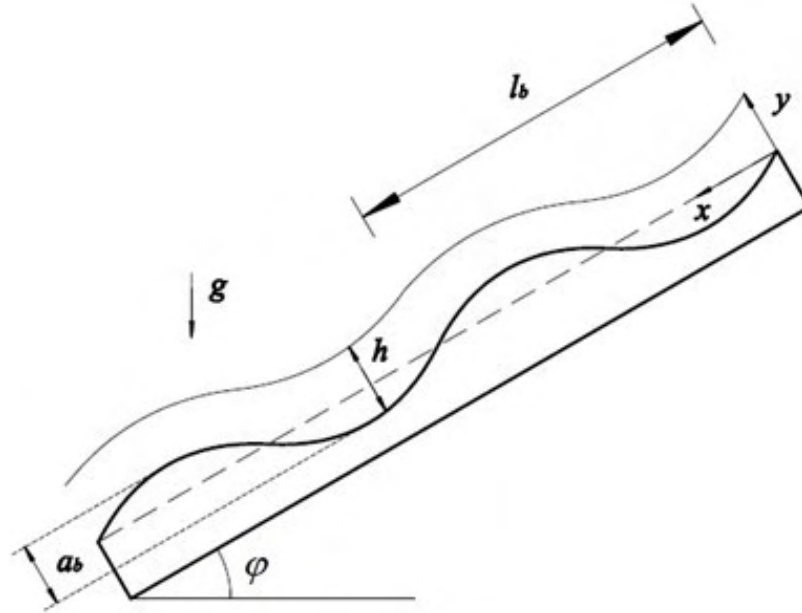


Figure 3.9: Schematic diagram of film flow over flat wall

by a density meter based on the balance of buoyancy force and gravity. The kinematic viscosity is measured by a Cannon-Fenske opaque (reverse-flow) viscometer, and involves multiplying the efflux time and the viscometer constant. The surface tension varies slightly with concentration, and is determined by a tensiometer (SINTERFACE STA-1), whose operation is based on measuring the force acting on a ring when it is pulled out through the liquid surface. All the measurements were taken at the actual temperature of the liquid in the experiment, since the properties of the fluids (especially viscosity) vary significantly with temperature. Temperature is kept constant between each set of experiments, and the properties are to re-measured if there is temperature variation between experimental campaigns.

The main raw variables are channel inclination and flow rate. The inclination angles range from $0^\circ \sim 48^\circ$ for the inclined channel and 90° for the vertical cylinder. It was measured by a digital inclinometer, with an accuracy of $\pm 0.05^\circ$. In terms of the flow rate, an overall measurement is sufficient for the current study.

3. Experimental Setup and Problem Definition

Thus, a simple averaging method, which is based on weighting the fluid that exits from the outlet during a given time interval, is employed for the measurement of mass flow rate. The volumetric flow rate per unit width, q , can be obtained easily by further dividing with the density and the channel width.

The corrugated wall consists of periodic corrugations with two surface shapes, sinusoidal and orthogonal. Key geometric characterizations are the wavelength, l_b , and the height, a_b , introduced by the wall. Following a recommendation in the literature (Nguyen & Bontozoglou, 2011; Trifonov, 2007), we normalize l_b with the capillary length of the liquid. The reasoning is that at small enough $L_b = l_b/l_c$, the free surface will remain roughly flat, whereas at very large L_b it is expected to conform more closely to the shape of a smoothly varying wall. The intermediate values of L_b are of particular interest, in relation to the predicted and observed possibility of resonant-like free surface deformation Bontozoglou & Papapolymerou (1997); Trifonov (1999); Vlachogiannis & Bontozoglou (2002). The height, a_b , of the corrugations also appears to exert a strong influence (Argyriadi *et al.*, 2006; Wierschem *et al.*, 2005), and we normalize it as the steepness, $A_b = a_b/l_b$.

Other characteristic scales of the problem are based on the classical Nusselt solution for films along flat substrate, or on combination of physical properties, and include the Nusselt film thickness, $h_N = (\frac{3q\nu}{g\sin\varphi})^{\frac{1}{3}}$, Nusselt velocity, $u_N = \frac{gh_N^2\sin\varphi}{3\nu}$, capillary length scale, $l_c = (\frac{\sigma}{\rho g})^{1/2}$, viscous length $l_\nu = (\frac{\nu^2}{g})^{\frac{1}{3}}$, and time scale $t_v = (\frac{\nu}{g^2})^{\frac{1}{3}}$. The thickness and velocity are scaled by Nusselt film thickness and Nusselt velocity.

Data are parameterized in terms of two dimensionless numbers: (i) the Reynolds number,

$$Re = \frac{q}{\nu} \quad (3.3)$$

and (ii) the Kapitza number, defined as

$$Ka = \frac{\sigma}{\rho g^{\frac{1}{3}} \nu^{\frac{4}{3}}} \quad (3.4)$$

3. Experimental Setup and Problem Definition

Noteworthy is that the Ka as defined here is different from Kapitza number in some literature (as well in chapter 2), where inclination angle is embedded. The Kapitza number may be re-written as $Ka = (l_c/l_v)^2$. Thus, Ka depends only on physical properties and represents the competition between capillary and viscous phenomena. The values corresponding to the present experiments are low enough to make the recently discovered (Georgantaki *et al.*, 2011) effect of side-walls on the primary instability practically insignificant.

Chapter 4

Short wave instability

4.1 Introduction

This chapter, which is a revised version of a paper by Cao *et al.* (2013), reports on a short-wave instability observed experimentally along the corrugated substrates. Detailed data on the primary instability for two different wall shapes and a wide range of inclinations will be presented. It provides experimental evidence that the instability may indeed occur through a disturbance of finite wavelength (short-wave mode), and documents the parametric effect of inclination angle and wall shape in the transition from a long- to a short-wave mode. For the wall parameters tested, the corrugations prove strongly stabilizing, and a qualitative interpretation of this behaviour is attempted. This chapter will be organized as following:

Section 4.2 describes the experimental setup and methodology.

Section 4.3 presents and discusses the results.

Finally, some concluding remarks will be given in section 4.4.

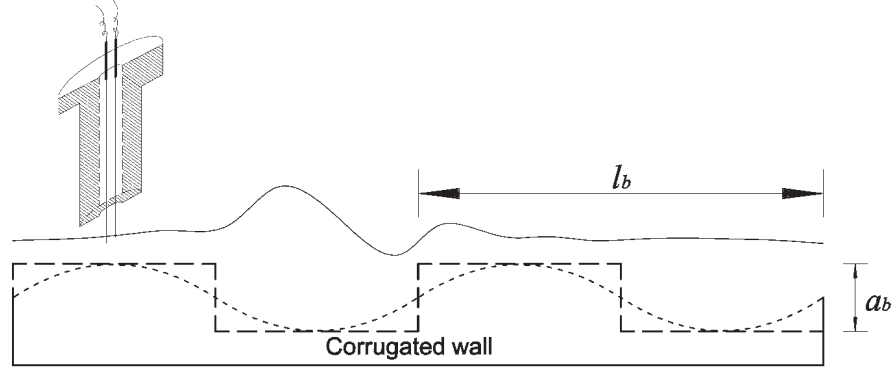


Figure 4.1: Schematic diagram of the film flow test section, with the geometric characteristics of the two corrugated walls (---, orthogonal wall; ·····, sinusoidal wall), and the typical location of a conductance probe.

4.2 Experiment Methodology

The present experiments are performed on the inclined channel, and corrugated walls with two surface shapes are investigated: in one case the corrugations are purely sinusoidal and in the other they consist of symmetric step-ups and step-downs (the latter are referred to as orthogonal corrugations). The two walls, shown schematically in figure 4.1, share the same wavelength, $l_b = 12$ mm, and height, $a_b = 2$ mm. Thus, the effect of exact wall shape on the stability results can be directly interrogated. The normalized wavelength L_b and steepness A_b corresponding to the above walls are $L_b = 4.9$ and $A_b = 0.167$.

The liquid used in the experiments is an aqueous glycerol solution with weight percentage around 68 % ($\rho = 1.17$ g/cm³). The temperature is kept constant ($\pm 0.5^\circ\text{C}$) during each set of experiments. Slight variations in temperature between different experimental campaigns are counter-balanced by appropriate changes of the exact glycerol content, so that liquid viscosity remains practically unaffected ($\nu = 10.9$ mm²/s). A system for perturbing the entrance flow rate through an electronic valve at bypass is available in the channel, in order to generate periodic inlet disturbances at desired frequency. Some of the present experiments were performed with a low-frequency inlet disturbance of 0.167 Hz, while others were

only driven by ambient noise. Multiple conductance probes are installed along the channel to measure the local film thickness at various locations. The main advantage of this technique that is relevant to the present investigation is the high rate (≥ 800 Hz) of data collection. Thus, short traveling disturbances are easily detected. Correlating signals from different probes provides information on the spatial growth/decay and on the wavelength and phase velocity of these traveling disturbances. Each probe, sketched in figure 4.1, consists of two parallel chromel wires, 0.4 mm in diameter, separated by an axis-to-axis distance of 2 mm. A function generator provides an input sinusoidal signal to the probes at a frequency of 25000 Hz in order to avoid polarization effects. The output signal is a sinusoidal voltage whose amplitude depends linearly on system conductance, and thus varies with the coverage of the wires by the liquid. The probes are simultaneously calibrated in-situ by taking measurements of the output voltage in the stable flow regime (without inlet disturbances) and calculating the film thickness from the Nusselt solution. In all cases, voltage is found to vary linearly with thickness.

4.3 Result

4.3.1 Fundamental difference between flat and corrugated walls

As already mentioned in the chapter 2, it has been shown both experimentally and theoretically (Brevdo *et al.*, 1999; Liu *et al.*, 1993) that, liquid films on an inclined flat wall are first destabilized by long-wave disturbances, when above the critical Reynolds number, $Re = \frac{5}{6} \cot \varphi$. The disturbance will travel downstream fast enough to result in a convective instability. This characteristic was recently exploited by Vlachogiannis *et al.* (2010), in order to determine the primary instability threshold with smaller effort and higher accuracy. In their experiments,

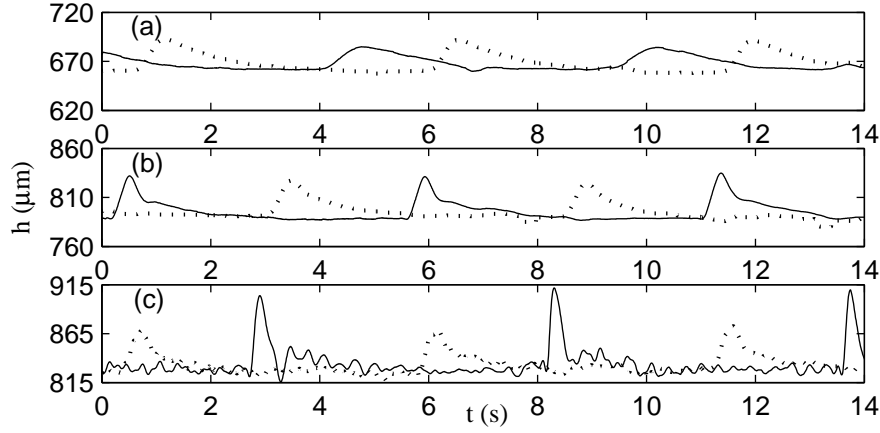


Figure 4.2: Typical time series of liquid film height (·····, upstream signal; —, downstream signal, probe separation 500 mm) on a flat substrate at inclination $\varphi = 5^\circ$, resulting from an inlet disturbance of frequency $f = 0.167$ Hz. The three plots correspond to Re : 8.1, 15.6 and 19.3. The critical Reynolds is determined as $Re_{flat} = 13.1$.

disturbances of constant, very low frequency, $f = 0.167$ Hz, were introduced at the channel inlet, and the ratio of downstream to upstream amplitude served to determine crossing of the threshold. Typical time-signals, below and above the critical Reynolds, are shown in figure 4.2. They indicate that at subcritical Re the disturbances retain their shape and only decline in amplitude, whereas at supercritical Re they grow in amplitude and gradually begin to break into a number of shorter components. We presently consider the two periodically corrugated walls, one sinusoidal and one orthogonal. As will be subsequently shown, both walls produce a strong delay in the appearance of the primary instability of the liquid film. However, we postpone for later the effect of corrugations on the critical Re , and concentrate first on the characteristics of the instability mode.

The new results are more evident for the sinusoidal wall, since they occur over almost the entire range of inclination angles ($\varphi > 7^\circ$) tested. Figure 4.3 shows upstream and downstream time-signals for $\varphi = 10^\circ$ and increasing Re . The locations of the two probes are 150 mm (upstream) and 650 mm (downstream)

from the channel inlet, or respectively 50 mm and 550 mm from the onset of the corrugations (a flat section of length 100 mm precedes the corrugated section). The behaviour exhibits a distinctly different parametric evolution with Re , as compared to a flat wall. In particular, beyond a value of Re , the time-signal presents an oscillation of high frequency that is superposed on the low-frequency inlet disturbances and dominates the free surface dynamics. More specifically, according to the data in figure 4.3, a high-frequency oscillation is clearly present at $Re = 7.7$ and beyond, whereas its onset is determined—by a technique described in the next subsection—at $Re = 7.3$. It is important to observe that the high-frequency oscillation first manifests at a Re for which the long-wave disturbances imposed at the inlet still decline. Indeed, it is visibly evident in figure 4.3 that the low-frequency humps decrease in amplitude from the upstream to the downstream probe, both at $Re = 7.7$ and $Re = 8.9$. Furthermore, the experimentally determined critical Re for the onset of the high-frequency oscillation, $Re_{cr} = 7.3$, is significantly higher than the theoretical, long-wave prediction for a flat wall, $Re_{flat} = (5/6) \cot\varphi = 4.73$. From all the above, we conclude that the high-frequency oscillation corresponds to a new instability mode, which sets in before the long-wave disturbances actually become unstable.

In order to check the above conjecture for a new mechanism, we consider the dynamics of the free surface without the regular inlet disturbances. Representative time-series for the same as above and various Re are shown in figure 4.4. Subject only to ambient noise, the free surface develops downstream an oscillatory component whose amplitude increases with Re . This oscillation consists of a background signal with rather well-defined frequency, which is modulated at a longer time scale. By comparing the evolution of the flow with and without low-frequency inlet disturbances, we note that (a) the oscillation has the same frequency, irrespective of the existence of the regular inlet disturbances, and (b) it occurs at roughly the same Re , with small differences attributable to the variation in the local value of Re caused by the low-frequency inlet disturbances (the

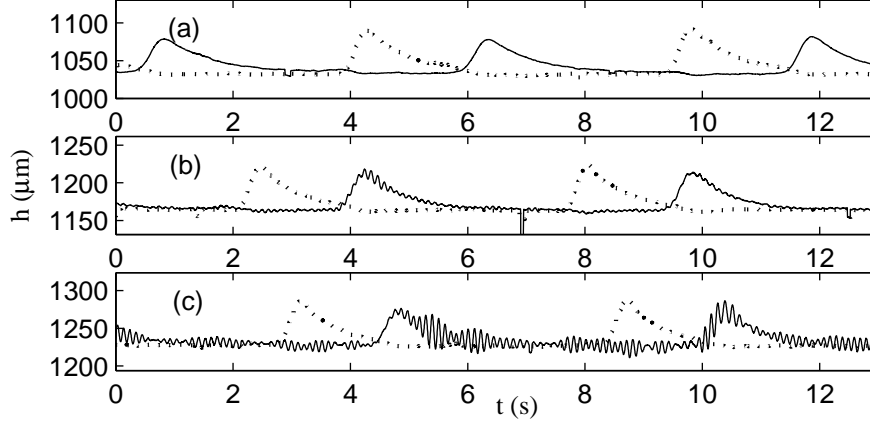


Figure 4.3: Time series of liquid film height (\cdots , upstream signal; $—$, downstream signal, probe separation 500 mm) on the sinusoidal substrate at inclination $\varphi = 10^\circ$, resulting from an inlet disturbance of frequency $f = 0.167$ Hz. The three plots correspond to Re : 5.3, 7.7 and 8.9. The onset of the high-frequency oscillation is determined—by a technique to be discussed in the next sub-section—as $Re_{cr} = 7.3$.

oscillation appears at slightly lower Re on the crests of long waves). Thus, we argue in favour of the existence of two different instability modes, which at most interact only weakly.

The characteristics of the new mode are investigated in the next section. In particular, we show that it is a traveling wave with finite wavelength. Thus, from here on it will be referred as “the short-wave mode”.

4.3.2 Characteristics of the short-wave mode

For the classical long-wave instability, the method of detecting instability threshold is already introduced in chapter 3. However, for short-wave mode, it is no longer valid, since the oscillation occurs prior to long-wave disturbance that we introduced. A new method, by which the onset of the short-wave mode can be reliably determined, will be suggested here.

The time-signal of film flow without inlet disturbance (only subject to ambi-

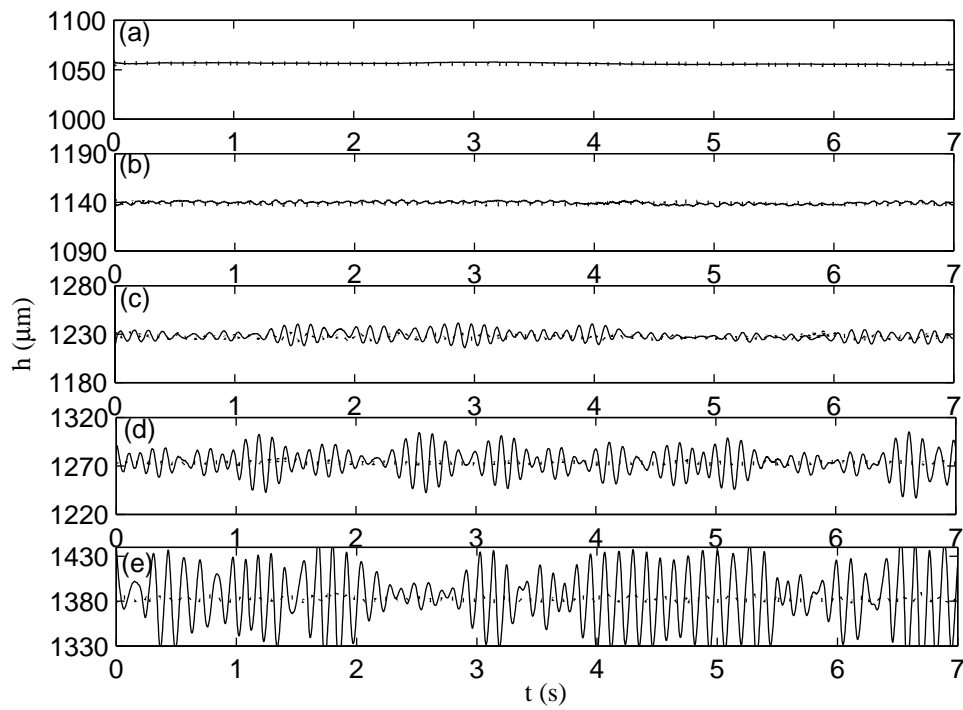


Figure 4.4: Time series of liquid film height (\cdots , upstream signal; $—$, downstream signal) on the sinusoidal substrate at inclination $\varphi = 10^\circ$, resulting only from ambient noise. The five plots correspond to Re : 5.7, 7.3, 9.1, 10.1 and 12.7. The critical Reynolds is determined as $Re_{cr} = 7.3$

4. Short wave instability

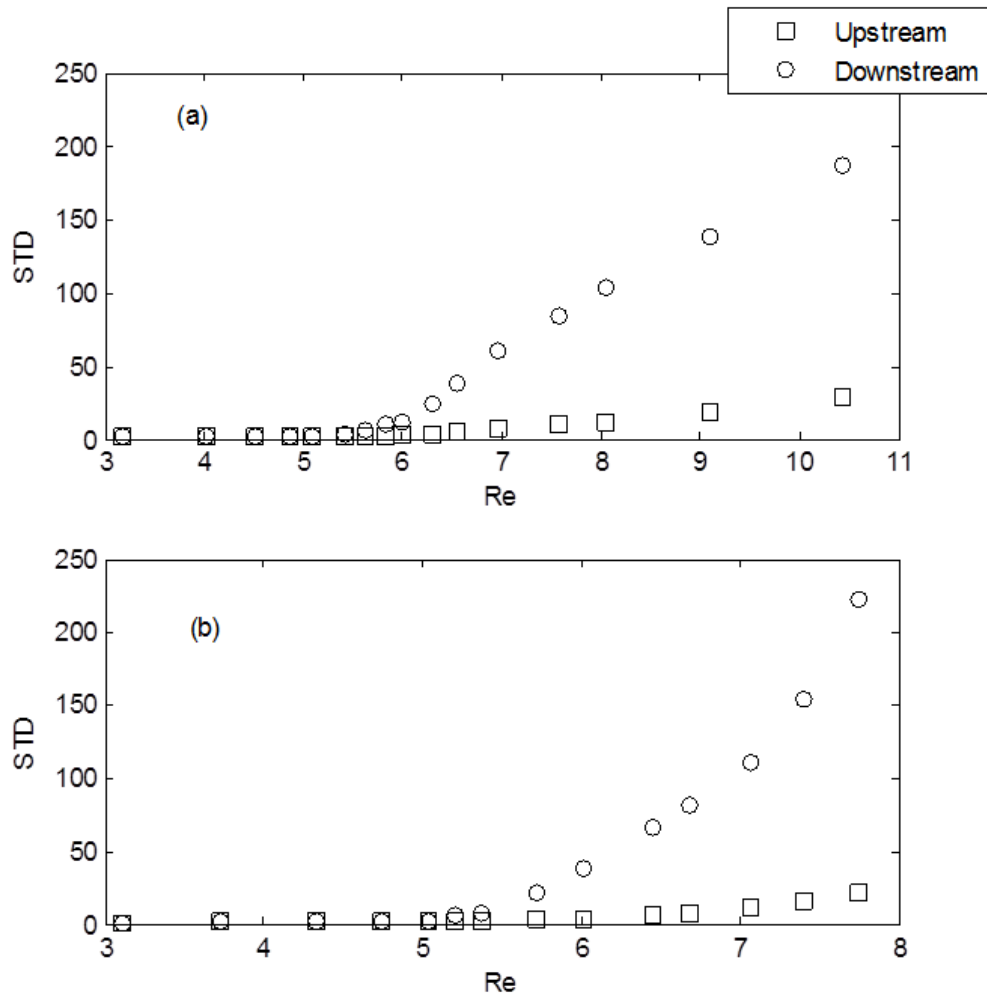


Figure 4.5: Variation of the standard deviation of time signals with increasing Re at inclination 15° and 25° ((upstream: \square ; downstream: \circ)).

ent noise), is used to quantify the magnitude of the oscillation by its standard deviation (STD). Data of STD, corresponding to two inclinations $\varphi = 15^\circ$ and $\varphi = 25^\circ$, are shown in figure 4.5 a and figure 4.5b respectively. It is evident that the magnitude of the oscillation for both upstream and downstream signals originally remains constant a value approximately of zero (small deviation of zero due to the discretization error of signal), and start to increase at well-defined thresholds, whose values may readily be determined by interpolation. For each inclination angle, the threshold is the same for upstream and downstream, but the downstream signal is increasing in a higher rate than upstream, which is reasonable since the disturbances are amplified downstream. Actual values are $Re_{cr} = 5.2$ for $\varphi = 15^\circ$, and $Re_{cr} = 5.0$ for $\varphi = 25^\circ$, and these have been used in normalizing the x-axis, as re-plotted in the figure 4.6a and 4.6b. The parametric evolution of the magnitude of the oscillation with Re may be satisfactorily fitted by an equation of the form

$$STD = \alpha(Re - Re_{cr})^\beta \quad (4.1)$$

as is confirmed by figure 4.6c, which shows a log-log plot of the data in figures 4.6a, b. Parameter β is determined from the slopes in figure 4.6c, as $\beta = 1.21$ (upstream) and 1.41 (downstream) for $\varphi = 15^\circ$, and $\beta = 1.57$ (upstream) and 1.72 (downstream) for $\varphi = 25^\circ$.

As discussed in relation to figures 4.3 and 4.4, the new instability mode introduces an intrinsic frequency, which is insensitive to external excitation. This is further demonstrated in Fourier space. Figures 4.7a and 4.7b show the fast Fourier Transform (FFT) of time-signals, respectively without and with the low-frequency inlet disturbance, at a Reynolds number, $Re = 7.0$ for $\varphi = 15^\circ$, which is above the critical value ($Re_{cr} = 5.2$). A dominant peak around $f = 10$ Hz (with rather narrow frequency range and a discernible first super-harmonic at 20 Hz) is evident in both figures, and corresponds to the new instability.

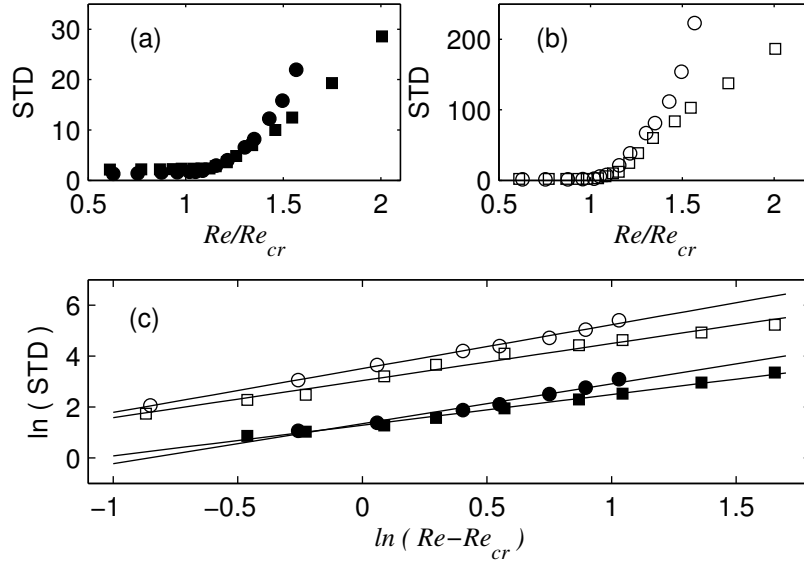


Figure 4.6: Variation of the upstream (a) and downstream (b) standard deviation of time signals with increasing Re at inclination 15° (upstream: \blacksquare , downstream: \square) and 25° (upstream: \bullet , downstream: \circ). (c): log-log plot of STD with $(Re - Re_{cr})$.

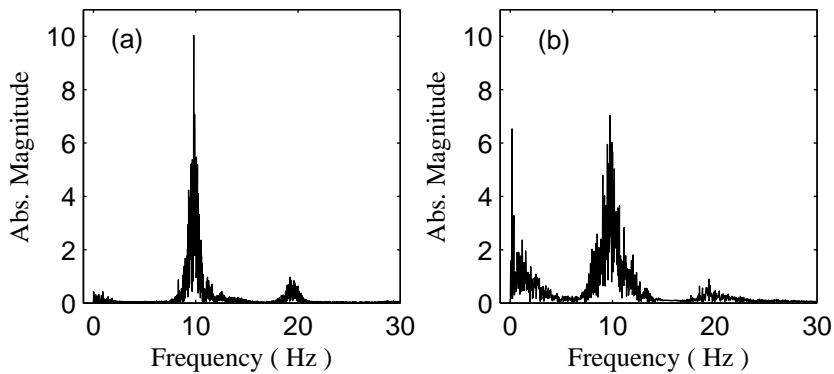


Figure 4.7: Fast Fourier Transform of a time signal without (a) and with (b) inlet disturbance, under condition of $Re = 7.0$ and inclination 15° .

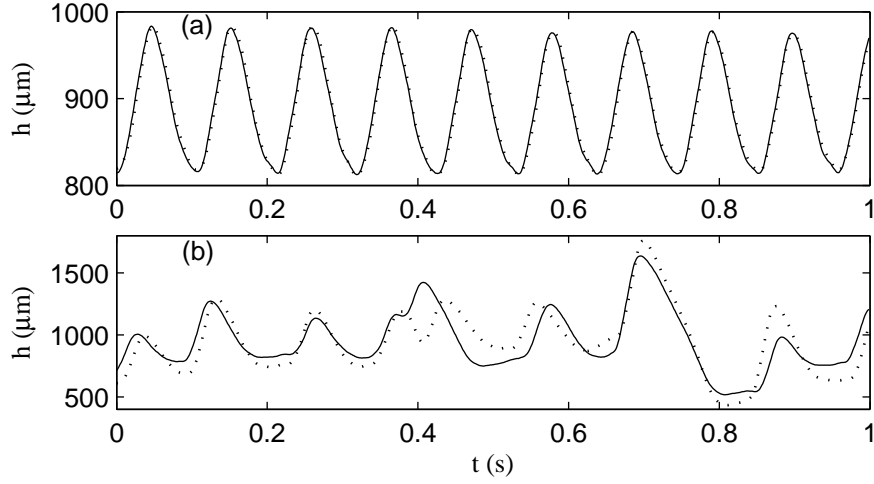


Figure 4.8: Time signals taken at the same streamwise distance from the inlet and symmetrically off the channel centreplane. a: $Re = 8.1$, b: $Re = 17.8$. The inclination is 15° and the experimental critical Reynolds is $Re_{cr} = 5.2$

This behaviour is characteristic of a global mode, rather than a spatial one. This view is further supported by figures 4.6a and 4.6b, which may be interpreted as providing the saturation amplitude of the oscillation as function of the control parameter, Re . Thus, it appears that, beyond a specific inclination, the liquid film along the present periodic substrate switches in behaviour from a noise amplifier to an oscillator (Huerre & Monkewitz, 1990). In this frame, theoretical identification of an absolute instability arises as a challenging question. This would not be the first occurrence of a transition from convective to absolute instability in a thin film system. For example, Duprat *et al.* (2007) predicted such a transition for a viscous film flowing down a vertical fibre.

An interesting characteristic of the short-wave mode is that it is persistently two-dimensional, i.e. it is invariant in the transverse direction, for a significant range of Re beyond the instability threshold. This is confirmed by taking time-signals at the same downstream location but symmetrically off the channel centerplane. Such data are shown for $\varphi = 15^\circ$ and $Re = 8.1$ in figure 4.8a, where the

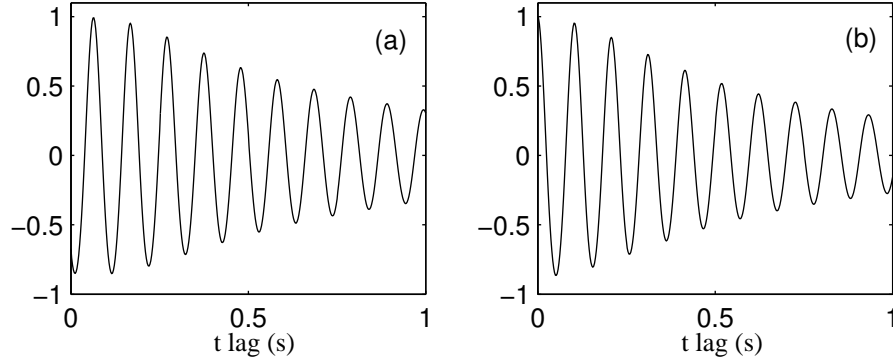


Figure 4.9: a: cross-correlation, and b: autocorrelation of a time signal at $Re = 8.0$ and inclination 15° .

probes are separated by a transverse distance of 110 mm. It is clear that the two signals are identical within experimental error, for a value of $Re \sim 50\%$ beyond the threshold. Results for a further strong increase in Re (above $\sim 200\%$ of the threshold) are shown in figure 4.8b, and indicate that the first deviations from two-dimensionality appear simultaneously with the loss of regularity. Figure 4.8b probably represents a series of fairly independent irregular waves. The aforementioned observation permits us to correlate signals at short streamwise separations (e.g. between consecutive crests), when close enough to the instability threshold, by locating the probes conveniently displaced in the transverse direction.

Moreover, the phase velocity and the wavelength of the short mode are determined. To this end, two probes are placed at a downstream location (approximately 300 mm from the onset of the corrugations), above consecutive crests of the sinusoidal wall. By taking the cross-correlation of the two signals (figure 4.9a), we compute a time-lag, which, in combination with the known distance between the probes (12 mm), gives a non-zero mean phase velocity. Thus, the high-frequency oscillation corresponds to a traveling mode. Using the phase velocity just determined, we return to any of the time-signals and take its auto-correlation (figure 4.9b) in order to calculate the wavelength of the traveling disturbance. The high regularity of the oscillations in the two correlations in figure 4.9, and the slow

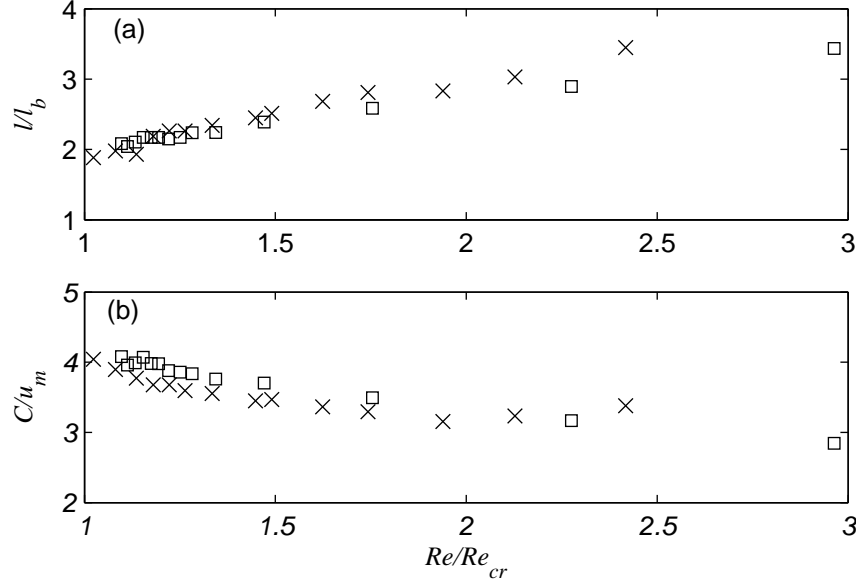


Figure 4.10: a: Variation of wavelength, l/l_b , and b: variation of phase velocity, c/u_N , of the short-wave mode, as a function of Re/Re_{cr} . u_N is the mean Nusselt velocity. \square , $\varphi = 15^\circ$, \times , $\varphi = 25^\circ$.

decay in magnitude of the maxima, manifest that the short-wave mode produces on the free surface a very regular and periodic pattern.

In figure 4.10a, b, we document respectively the parametric evolution of wavelength, l , and phase velocity, c , of the short-wave mode as function of the deviation from the instability threshold. The data are non-dimensionalized respectively with the wavelength of the wall, l_b , and with the mean Nusselt velocity, $u_N = (\nu g \sin \varphi Re^2 / 3)^{1/3}$. Results are shown for two inclination angles, $\varphi = 15^\circ$ and 25° , and exhibit only minor variation. In figure 4.10a, we note that the wavelength of the traveling disturbance attains its lowest value at the onset of the instability, and from there on grows roughly linearly with increasing Re . This is the opposite trend from the behaviour of the classical, long-wave instability of film flows, which starts from infinite wavelength at the onset and then gradually shrinks with increasing Re .

The variation of the dimensionless mean phase velocity with Re is shown

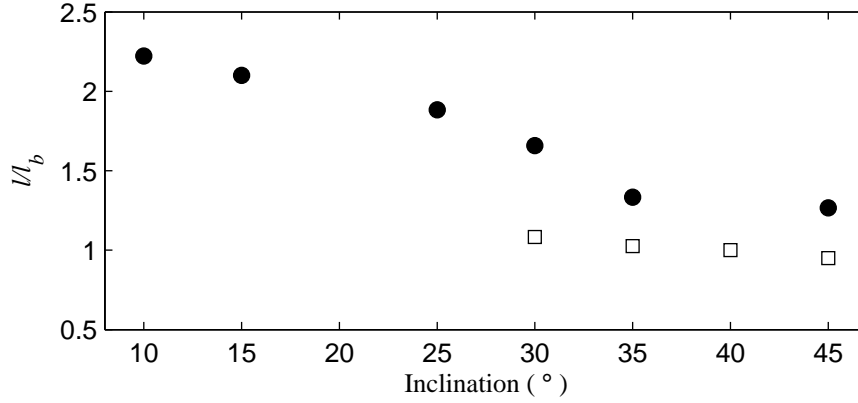


Figure 4.11: Wavelength of the short-wave mode at inception, as function of channel inclination. ●, sinusoidal, and □, orthogonal wall.

in figure 4.10b. We use the qualifier “mean” for the phase velocity, because we anticipate that it will generally vary depending on whether the disturbance travels above a crest or a trough, and that this variation will be periodic with the wavelength of the corrugation. We observe that the mean phase velocity of the short-wave mode is initially slightly higher than four times the Nusselt velocity, and then decreases with Re .

4.3.3 Investigation of the primary instability threshold

After documenting the existence and the main characteristics of the new instability mode in film flow along a periodic wall, in the following section, the competition between the long- and the short-wave mode, and of their combined effect on the primary instability of the film, will be investigated. Up to this point, all the results presented are only for the sinusoidally corrugated wall. Here, results for the orthogonal wall will also be included. Since the two walls share the same wavelength and height, these results will help to investigate the potential role of the wall shape on the critical Re of the primary instability, and also on the mode of the instability.

The wavelength of the unstable mode at the critical threshold is first consid-

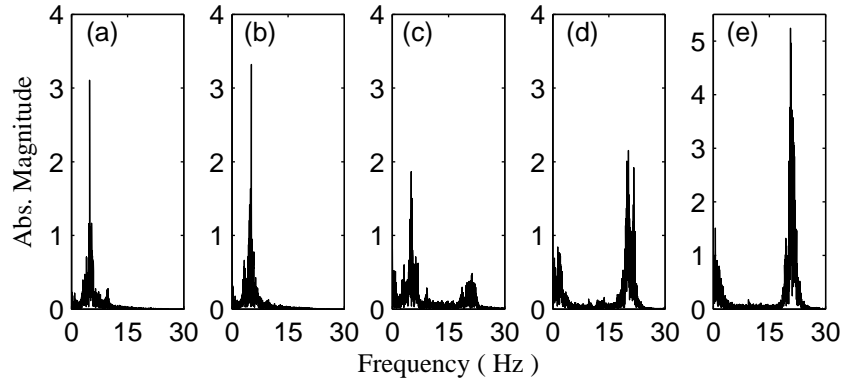


Figure 4.12: Fast Fourier Transform of time signals taken along the orthogonal wall, at increasing inclination. a: $\varphi = 15^\circ$ ($Re = 11.2$), b: $\varphi = 20^\circ$ ($Re = 10.0$), c: $\varphi = 25^\circ$ ($Re = 8.6$) d: $\varphi = 30^\circ$ ($Re = 7.6$), e: $\varphi = 35^\circ$ ($Re = 5.6$).

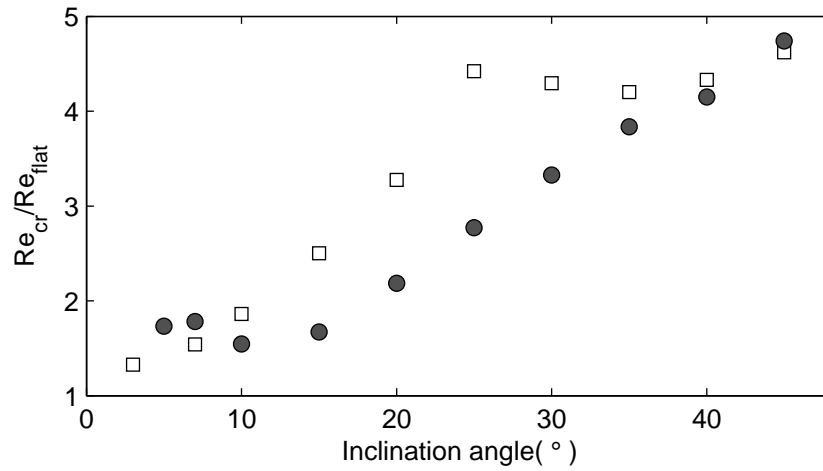


Figure 4.13: The experimentally observed critical Reynolds, normalized with the theoretical prediction for a flat wall, as function of channel inclination. ●, sinusoidal, and □, orthogonal wall.

ered. It is recalled from the introduction that D'Alessio *et al.* (2009) and Häcker & Uecker (2009) have predicted the possibility of transition from long-wave to short-wave instability for high enough corrugations, without paying particular attention to the channel inclination. In the present work, we study only one corrugation steepness, but vary the inclination angle. Results are shown in figure 4.11 for both the sinusoidal and the orthogonal wall. For the sinusoidal wall, the wavelength at inception is finite for $\varphi \geq 10^\circ$, and continuously decreases with inclination. Based on an extrapolation of the results for high inclinations, it may be conjectured that the instability wavelength will approach that of the wall in the limit of a vertical channel. At the other end, experiments at small inclinations indicate that the short-wave mode disappears rather abruptly below $\varphi \leq 7^\circ$, and instability sets in by amplification of the long (low-frequency) inlet disturbance. This is the reason why no data points are plotted below $\varphi < 10^\circ$.

Unlike the results with sinusoidal corrugations, the wavelength at inception with orthogonal corrugations varies weakly with inclination, and is practically equal to that of the wall for the highest inclinations tested. Even more important, the short-wave mode now disappears at inclinations $\varphi \leq 25^\circ$. This is again the reason why no data points are plotted below this inclination. Comparing the two sets of data in figure 4.11, it may be concluded that the shape of the wall has a leading-order effect on the instability mode that prevails.

The rather abrupt transition from one mode to the other can be further demonstrated in Fourier space. Figure 4.12 is an example of Fast Fourier Transforms of time signals from the orthogonal wall. The two FFTs at the left, taken at inclination below the transitional value, $\varphi = 25^\circ$, have dominant frequency around 5 Hz; the two on the right, at inclinations above the long- to short-mode transition, have jumped to a frequency around 20 Hz. The intermediate FFT corresponds to $\varphi = 25^\circ$, and exhibits both peaks.

The dependence of inception wavelength on Re and inclination (demonstrated in figure 4.11), and more generally, the fact that it differs from that of the wall,

argues in favour of the short-wave mode as being the result of a genuine absolute instability. In particular, it may not be considered a naive outcome of spatial forcing, similar to the synchronization of film flow along a flat wall subject to a periodic temporal forcing at the inlet. Indeed, in the latter case, the period measured at a fixed location does not vary with Re , inclination etc, but is “by definition” always equal to the period of the inlet forcing. Of course this is an indirect argument, and a direct and unequivocal experimental confirmation of the absolute nature of the instability would be evidently very welcome.

Next, we concentrate on the critical Re for the film to become unstable, irrespective of the mode that is responsible for the transition. In order to directly assess deviations from a flat wall, the experimentally determined critical Re for each of the corrugated walls is normalized with the classical long-wave prediction, $Re_{flat} = (5/6) \cot\varphi$. The results for Re_{cr}/Re_{flat} , as function of inclination angle, are shown in figure 4.13 and lead to the following phenomenological conclusions: (a) The primary instability is always delayed by the presently examined corrugated walls, and the difference from the prediction for a flat wall is quantitatively very significant. (b) Inclination angle has a strong effect, with the film becoming progressively more stable at higher inclinations. (c) The exact shape of the periodic wall has again a leading-order effect: Film flow along the orthogonally corrugated wall is distinctly more stable at intermediate inclinations.

It is interesting to note from figure 4.13 that the data for both walls exhibit a discontinuity in slope, but each at a different value of inclination angle. The sinusoidal wall changes behaviour at $\varphi = 7^\circ$, whereas the orthogonal wall has a pronounced cusp at $\varphi = 25^\circ$. In both cases, the change coincides with the previously described exchange of the role of the short and the long-wave mode as the disturbance responsible for the primary instability. Thus, the abrupt transition from one mode to the other also manifests in the variation of the critical Re with inclination. In this sense, the data for each wall presented in figure 4.13 may be considered to consist of two independent curves, corresponding respectively to

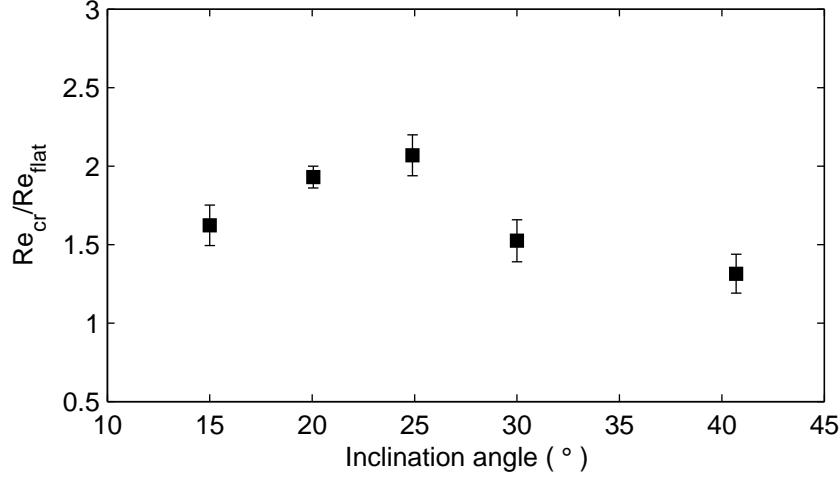


Figure 4.14: Experimentally observed critical Reynolds number, normalized with the theoretical prediction for a flat wall, as function of channel inclination. Measurements taken by (Wierschem *et al.*, 2005) for silicon oil flowing along a sinusoidal substrate with $l_b = 300$ mm and $a_b = 15$ mm.

the parametric variation with inclination of the long and the short mode. These two curves cross at the point of discontinuity. It is further noted that a similar discontinuity in slope exists in the data of Wierschem *et al.* (2005), which are reproduced in figure 4.14 as Re_{cr}/Re_{flat} versus inclination. It would be of evident interest to examine whether this discontinuity is also associated with a change in the mode of instability.

As a consequence of all the above (and as implicitly suggested by Trifonov (2007)) it might be of interest to check the following potential rule of thumb: The critical Reynolds, Re_{cr} , be estimated to leading order by the classical result of long-wave analysis for a flat wall, taking into account not only the first, but also the second term in the expansion, which introduces a finite-wavelength effect. Then, the role of periodic corrugations may be roughly accounted for by an appropriate choice of the disturbance wavelength. The relevant expression, from the solution of the Orr-Sommerfeld equation by a long-wave expansion, is (Oron

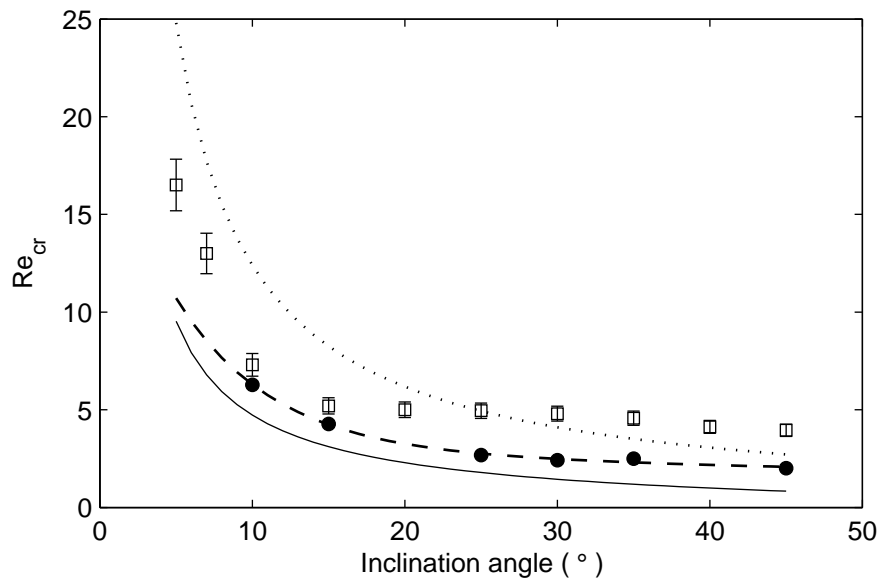


Figure 4.15: Critical Reynolds for the primary instability of liquid film flow along a sinusoidal wall. \square , present data; —, theoretical prediction for disturbances with infinite wavelength; \cdots , theoretical prediction for disturbances with the wavelength of the wall; $- \bullet -$, theoretical prediction for disturbances with the experimentally determined wavelength.

& Heining, 2008)

$$Re_{flat,2} = \frac{5}{6} \left[\cot\varphi + \frac{Ka}{\sin\varphi} \left(\frac{2\pi l_\nu}{L} \right)^2 \right] \quad (4.2)$$

where L is the wavelength of the imposed disturbance, and Ka and l_ν are respectively the Kapitza number and the viscous length-scale. Following this line of thought, we compare in figure 4.15 the data of critical Re for the sinusoidally corrugated wall to three predictions based on the above equation and different choices of L : The lowest curve corresponds to $L \rightarrow \infty$, the upper to $L = l_b$ and the intermediate one to the measured wavelength of the short-wave mode. The proposed rule of thumb works very satisfactorily, using the experimentally determined wavelength, in the range of inclinations $\varphi = 10^\circ$ – 15° . At lower inclinations, the agreement deteriorates, but the extreme predictions, based respectively on $L \rightarrow \infty$ and $L = l_b$ still bracket the data. At higher inclinations, the stability threshold appears to be underestimated even by the prediction based on the wavelength of the wall.

4.4 Concluding remarks

The present work contributes detailed data on the primary instability of liquid film flow along periodically corrugated substrates. Two different wall shapes (sinusoidal and orthogonal) are tested, for a range of inclinations 3° – 45° . It is found that, with increasing inclination, an abrupt transition in the instability mode is manifested: the classical long-wave instability, which is convective and thus determined by the characteristics of externally imposed excitation, is replaced by a new short, traveling mode, which is highly regular and strongly two-dimensional. The new instability introduces an intrinsic frequency insensitive to external excitation, and appears to be a global mode. The exact shape of the corrugations has a leading-order effect on the inclination on which the new mode appears and on its wavelength at inception.

Compared to the behaviour of film flow on a flat substrate, the presently

tested periodic walls are found to delay very significantly—but each one to a different extent—the onset of the primary instability. When expressed as a ratio of the experimental critical Re to the theoretical prediction for a flat wall, the delay increases with inclination, and presents a distinct discontinuity in slope when transition from the long- to the short-wave mode takes place.

The above behaviour raises the interesting question of why long-wave disturbances do not amplify at high enough inclinations. A qualitative explanation for this behaviour may be provided by positing an energy-transfer mechanism from long- to short-wave disturbances. Such a mechanism is presently speculative, but appears to be supported by preliminary numerical simulations that are presently under way. More specifically, it is well-known (e.g. Vlachogiannis & Bontozoglou (2002)) that a periodic wall imposes a similar spatial periodicity on the steady film flow. Free-surface disturbances may interact with this steady, base flow, with the result that wavelengths much longer than that of the wall are filtered out.

The above tentative mechanism is consistent with the aforementioned observation that stabilization by a periodic wall is stronger at higher inclinations. Indeed, it has been shown (Nguyen & Bontozoglou, 2011; Trifonov, 2007) that the periodic, steady deformation of the free surface imposed by the wall, becomes generally more pronounced as inclination increases. It is also consistent with the enhanced stability of the orthogonal wall. The latter may be viewed as a combination of super-harmonics of the wall wavelength, and indeed some of these harmonics appear distinctly in observations of the steady free surface deformation (Argyriadi *et al.*, 2006; Vlachogiannis & Bontozoglou, 2002; Wierschem & Aksel, 2004). As a result, the interaction between disturbances and steady flow will feed energy to shorter wavelengths that are more efficient in dissipating it by viscosity.

A theoretical framework to provide fundamental understanding of the primary instability along a corrugated substrate could borrow ideas from receptivity theory, in particular the interaction of an inlet disturbance, which imposes the tem-

poral scale, with the steadily deformed base flow, which imposes the spatial scale (Choudhari, 1993; Ruban, 1984). Another interesting line of thought involves the scattering of incident wave-energy by the wall topography, as predicted from inviscid theory, and in particular the Bragg resonance that leads to extensive reflection (Davies & Heathershaw, 1984). The availability of a proper theoretical framework would be very useful in the efficient scrutinization of the effect of substrates with different geometric scales. The impressive modification to the film flow, demonstrated by the present data for only one combination of corrugation height and wavelength, points to an enormous potential for instability control in such flows through the development of appropriately tailored substrates.

Chapter 5

Effect of corrugated wall steepness

5.1 Introduction

As reviewed in chapter 2, some recent computational studies propose that a destabilizing effect may be imposed by wall corrugations that are steep enough. It is thus of evident interest to investigate experimentally the effect of corrugations in a fuller range of wall steepness. Moreover, the question concerning instability mode (long- vs short-wave instability) at different wall geometry will also be considered.

5.1.1 Experimental conditions

The experiment results presented in the current chapter, are performed on six different corrugated walls, including sinusoidal and orthogonal shape. The results of the sinusoidal wall from previous chapter are brought for comparison. Since the shape of the wall corrugation has a leading-order effect, the two different shapes will be investigated separately.

The liquid used in the experiments is mainly an aqueous glycerol solution

with weight percentage around 68%, except in section 5.3.2, where an additional concentration (50%) is used in order to investigate the effect of viscosity. Slight variations in temperature and concentration exist in different experimental campaigns, but temperature is kept constant (± 0.2 °C) during each set of experiments. The liquid properties for each experimental campaign, are listed explicitly in the appendix for future reference. The Kapitza numbers are approximately 110 and 260, for the 68% and 50% aqueous glycerol solution respectively.

The conductance probe method same as the one described in last chapter was employed: Typical inlet perturbations are introduced at a frequency of 0.167 Hz. The measurement rate varies from 100–1000 Hz, due to different purposes of investigation.

5.2 Results of sinusoidal substrate

5.2.1 Effect of wall steepness

Two new sinusoidal walls are investigated to compare with result of sinusoidal wall which was presented in last chapter. The geometries of the corrugations of three different sinusoidal walls are listed in table 5.1. The wavelength l_b is normalized with the capillary length of the liquid, $l_c = (\frac{\sigma}{\rho g})^{1/2}$, and the amplitude a_b is normalized as steepness, $A_b = a_b/l_b$. As we known, for a vertical wall, at small enough $L_b = l_b/l_c$, the free surface will remain roughly flat, whereas at very large L_b it is expected to conform closely to the shape of smoothly varying wall (Trifonov, 1998). And the intermediate value of L_b is corresponding to the resonant-like phenomenon as described by Bontozoglou & Papapolymerou (1997). The normalized wavelengths for the three walls are respectively 0.82, 4.9 and 20.4, which have covered the three different cases, for small, intermediate and large L_b .

The threshold of primary instability for wall with small corrugations ($L_b=0.82$, $A_b=0.5$), is shown in figure 5.1: in the upper panel(a), critical Reynolds numbers measured from experiment (Re_{cr}) are plotted against the inclination an-

5. Effect of corrugated wall steepness

Table 5.1: List of dimensions the sinusoidal corrugations

No.	Shape	Wavelength (mm)	Height (mm)	L_b	A_b
1	Sinusoidal	2 mm	1 mm	0.82	0.5
2	Sinusoidal	12 mm	2 mm	4.9	0.167
3	Sinusoidal	50 mm	10 mm	20.4	0.2

gles, and the continuous line corresponds to theoretical prediction for flat substrate (Re_{flat}); in the lower panel(b), the experimentally determined threshold is normalized with the theoretical prediction for flat wall, referred as Re_{cr}/Re_{flat} . As can be seen from the figure, in all inclination angles, the measured critical Reynolds, Re_{cr} , is above the theoretical value of flat substrates, indicating a stabilizing effect. The stabilizing effect slightly varies with inclination angle, with its maximum at inclination angle of $\varphi = 15^\circ$, where the stable regime is expanded for approximately 60%. When above critical Reynolds number, the inlet disturbance with low-frequency (long-waves) was first observed to be amplified downstream, indicating a long-wave instability. We conclude that corrugations with small dimensionless wavelength act like roughness, and the flow does not vary drastically from that over a flat substrate. This behaviour may be interpreted by taking into account that, at such small L_b , the free surface does not deform much from the flat shape.

In the case of large corrugations ($L_b = 20.4$, $A_b = 0.2$), a distinctly different behaviour was observed (figure 5.2). This may be explained by the change of the steady free surface, which is now strongly deformed by wall corrugations, especially at high inclinations. Four inclination angles were investigated for this corrugated wall, and in all cases a stabilizing effects were observed, which is progressively increasing with inclination angles. In terms of the mode of instability, short-wave mode was detected in all the inclination angles. The following interpretation is proposed: due to the steep and long corrugations, the steady free surface takes the form of steps, while, in every trough, the local inclination angle is roughly zero. When the long-waves disturbances travel down the steps, they

5. Effect of corrugated wall steepness

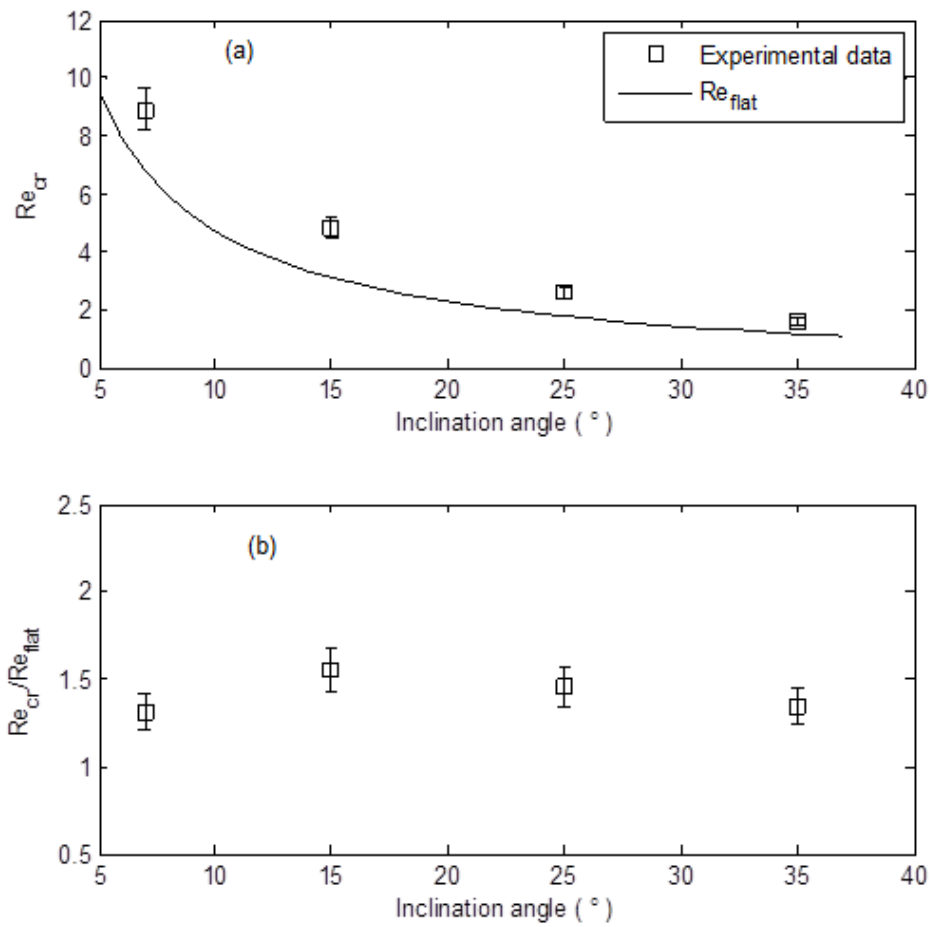


Figure 5.1: Measured (a) and normalized (b) critical Reynolds for the primary instability of liquid film flow along small sinusoidal corrugation ($L_b = 0.82$, $A_b = 0.5$). \square , experimental data; —, theoretical prediction for flat substrate.

5. Effect of corrugated wall steepness

easily break into smaller components right after entering the corrugation. In a different wording, the disturbances of shorter wavelength interact strongly with the steady structures on the free surface, and thus grow in amplitude.

The result of the intermediate corrugation ($L_b = 4.9$, $A_b = 0.167$) was reproduced in figure 5.3 for comparison. As discussed in chapter 4, the primary instability is delayed significantly by the corrugated wall, and the stabilizing effect varies with inclination angles. Moreover, a transition from long- to short-wave mode was observed, which exhibits a discontinuity in the figure ($\varphi = 7^\circ$).

The results for the three wall substrates are plotted together in figure 5.4. Generally, the wall with intermediate corrugation exhibits the most significant stabilizing effect (up to 350% at inclination of $\varphi = 45^\circ$), while the wall with small corrugation (roughness) only slightly expands the stable regime. The wall with the longest and steepest corrugations lies in-between, indicating that the role of the geometric characteristics of the wall is complex, and possibly involves non-monotonic dependence on steepness. The inclination has strong effect, with the film becoming progressively more stable at higher inclinations, for both large and intermediate corrugations. However, for the small corrugation, no such effect was observed.

5.2.2 Preliminary results of effect of liquid properties

Some preliminary results concerning the effect of liquid solution on the primary instability is presented in figure 5.5. Two different concentrations of aqueous glycerol solution, which are 68% and 50%, are investigated in the current experiment. The surface tension and density of the solution remains roughly constant with variation of the concentration. However, the viscosity for 68% aqueous glycerol solution is approximately twice of that of 50%. We consider in general that the effect of physical properties of the liquid is described satisfactorily by the Kapitza number. We presently vary only the viscosity, but we could also vary surface tension by adding in the liquid a highly soluble surfactant (Georgantaki

5. Effect of corrugated wall steepness

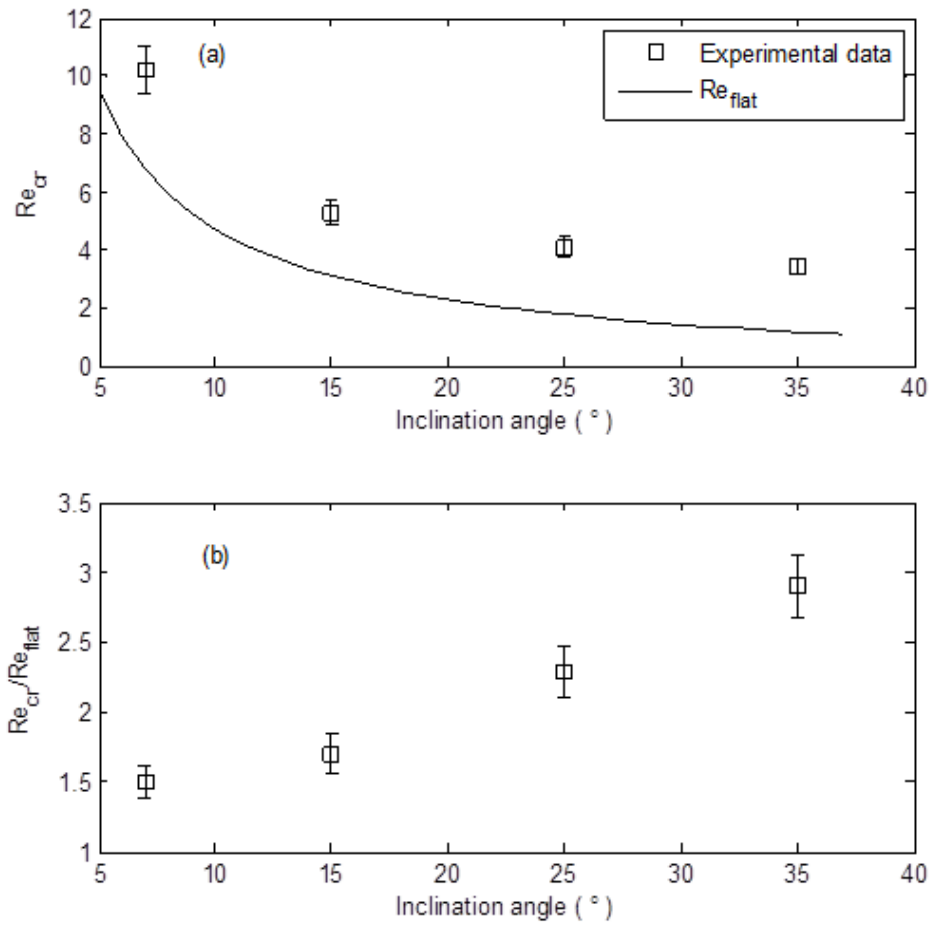


Figure 5.2: Measured (a) and normalized (b) critical Reynolds for the primary instability of liquid film flow along large sinusoidal corrugation ($L_b = 20.4$, $A_b = 0.2$). \square , experimental data; —, theoretical prediction for flat substrate.

5. Effect of corrugated wall steepness

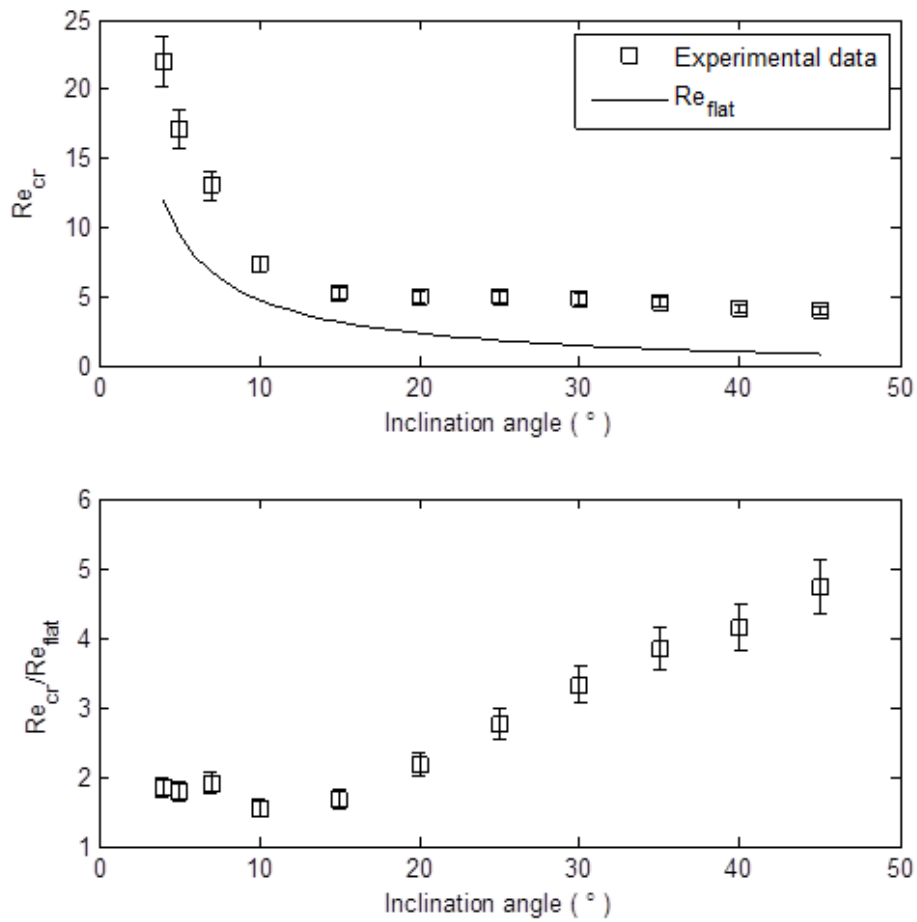


Figure 5.3: Measured (a) and normalized (b) critical Reynolds for the primary instability of liquid film flow along an intermediate sinusoidal wall ($L_b = 4.9$, $A_b = 0.167$). \square , experimental data; —, theoretical prediction for flat substrate.

5. Effect of corrugated wall steepness

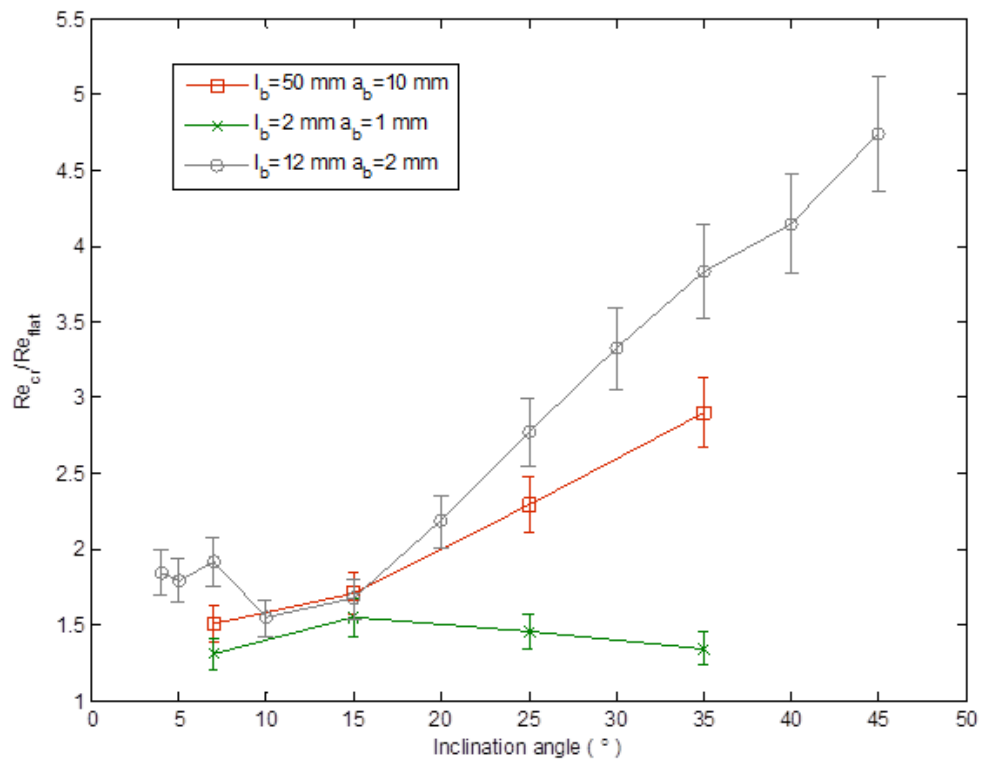


Figure 5.4: Normalized critical Reynolds for the primary instability of liquid film flow along three sinusoidal corrugations. (\times), $L_b = 0.82$, $A_b = 0.5$; (\square), $L_b = 20.4$, $A_b = 0.2$; (\circ), $L_b = 4.9$, $A_b = 0.167$.

5. Effect of corrugated wall steepness

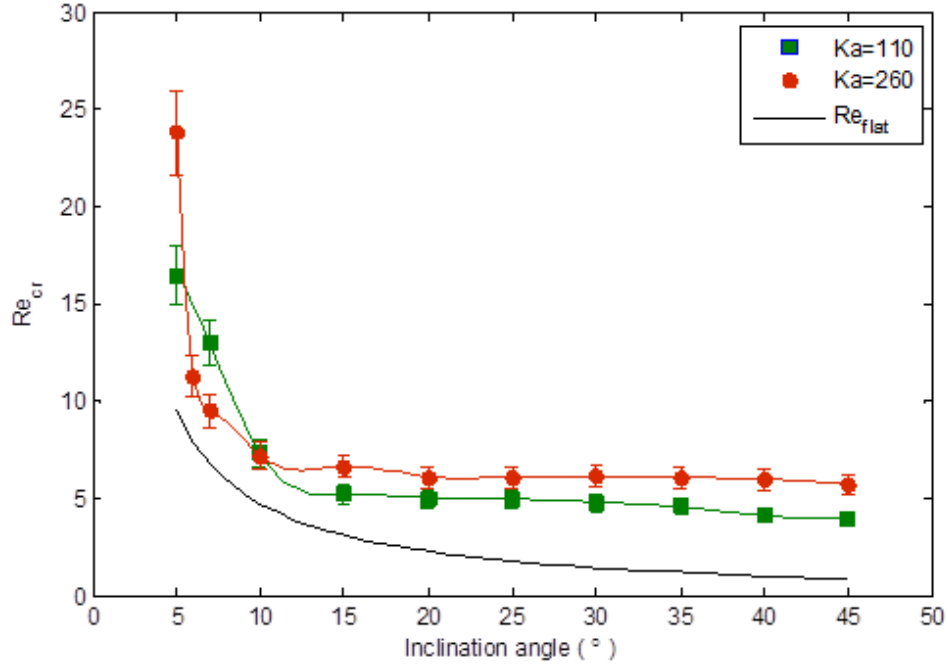


Figure 5.5: Critical Reynolds for the primary instability of liquid film flow along a sinusoidal corrugation ($L_b = 4.9$, $A_b = 0.167$). —●— and —■— are respectively for $Ka = 260$ and 110 . —, theoretical prediction for disturbances with infinite wavelength.

et al., 2011).

As shown in figure 5.5, the squares indicate the measured threshold for $Ka = 260$, while the circles refer to the results for $Ka = 110$. In all the inclination angles, stabilizing effect has been found in both liquid with current wall corrugation. However, the extent of the stabilizing effect varies in the range of tested inclination angles, which can be divided into three regions: for inclination angles $\varphi > 10^\circ$ and $\varphi \leq 5^\circ$, the film is more stable with higher Kapitza number, which is consistent with finding on flat substrate (Georgantaki *et al.*, 2011); while in the intermediate range $5^\circ < \varphi < 10^\circ$, the film is less stable with the liquid of $Ka = 260$.

The result presented in preliminary and fragmental, more detailed investigated in necessary in the future.

Table 5.2: List of dimensions the orthogonal corrugations

No.	Shape	Wavelength (mm)	Height (mm)	L_b	A_b
1	Orthogonal	24 mm	0.8 mm	9.7	0.033
2	Orthogonal	12 mm	0.8 mm	4.9	0.067
3	Orthogonal	12 mm	1.6 mm	4.9	0.133

5.3 Results on orthogonal substrate

For film over orthogonally corrugated walls, there are super-harmonics on the free surface (Argyriadi *et al.*, 2006; Vlachogiannis & Bontozoglou, 2002; Wierschem & Aksel, 2004), which make the phenomena of primary instability behaviour more complicated.

Three orthogonal walls are investigated in current experiments, as shown in table 5.2. The wavelengths for three walls, L_b , are of the same order, in which region free surface resonance occurs. Mainly, the effect of wall steepness will be studied from the experiments on those walls. Similar to the sinusoidal corrugations, the threshold of primary instability and the mode of instability are determined experimentally.

The experimental results from three orthogonally corrugated walls are illustrated respectively in figure 5.6, 5.7 and 5.8. Before discussing the effect of steepness on the instability threshold, we concentrate first on the instability mode. For the wall of smallest steepness, $A_b = 0.033$, only long-wave mode exists in all the tested inclination angles (shown in figure 5.6): the long-waves are observed to be amplified first downstream, when above the critical Re . For larger wall steepness ($A_b = 0.067$ and $A_b = 0.133$), both long-wave and short-wave mode are observed. The inclination angle where transition occurs is marked as red line in figure 5.7b and 5.8b. The red line is more appropriate to be viewed as a transition region rather than the exact transition boundary, and more closely-spaced experiments should be performed in order to determine the accurate transition conditions. For the wall of steepness $A_b = 0.133$, long-wave mode is observed at inclination angles, $\varphi < 25^\circ$, and short-wave mode dominates for inclinations, $\varphi > 25^\circ$. In the

case of $A_b = 0.067$, multiple transitions were found (figure 5.7): first transition occurs at inclination angle $\varphi = 7^\circ$, below which long-wave mode dominates and above which the primary instability becomes short-wave mode; a second short- to long-wave mode transition occurs at inclination around $\varphi = 25^\circ$. This behaviour is puzzling and needs to be further investigated. As a preliminary guess, it may be attributed to the more complicated free surface profile, where multiple harmonics exists. However, this cannot be confirmed by conductance probe method, which can only provide temporal, and not spatial, variation of film thickness.

Comparing the effect on the primary instability of various wall steepnesses become more complicated, since two different instability modes need to be considered. Generally, all three walls exhibit stabilizing effects on the film flow, and the stabilizing effects increase with wall steepness. The wall with largest steepness expands the stable regime up to 400% of that over flat substrate at high inclination angles. However, for the two lowest inclination angles tested ($\varphi = 3^\circ$ and 5°), the reverse trends was observed. The critical Reynolds number, Re_{cr} , becomes smaller with increasing steepness, as shown in figure 5.9.

5.4 Conclusion and discussion

In this chapter, the effect of wall corrugated wall on the primary instability was investigated in a wide range of wall geometries (both sinusoidal and orthogonal shape) and inclinations 3–45°. The tested periodic walls are always found to delay the onset of the primary instability with different extent, compared to the film flow on a flat substrate.

For sinusoidal shape, the three corrugations correspond to three different flow regimes: For the corrugation with smallest wavelength and amplitude, which can be viewed as surface roughness, the effect on primary instability is mild. A slight stabilizing effect was observed, and the effect remains roughly constant with inclination angles. Moreover, only long-wave mode was observed in the experiments

5. Effect of corrugated wall steepness

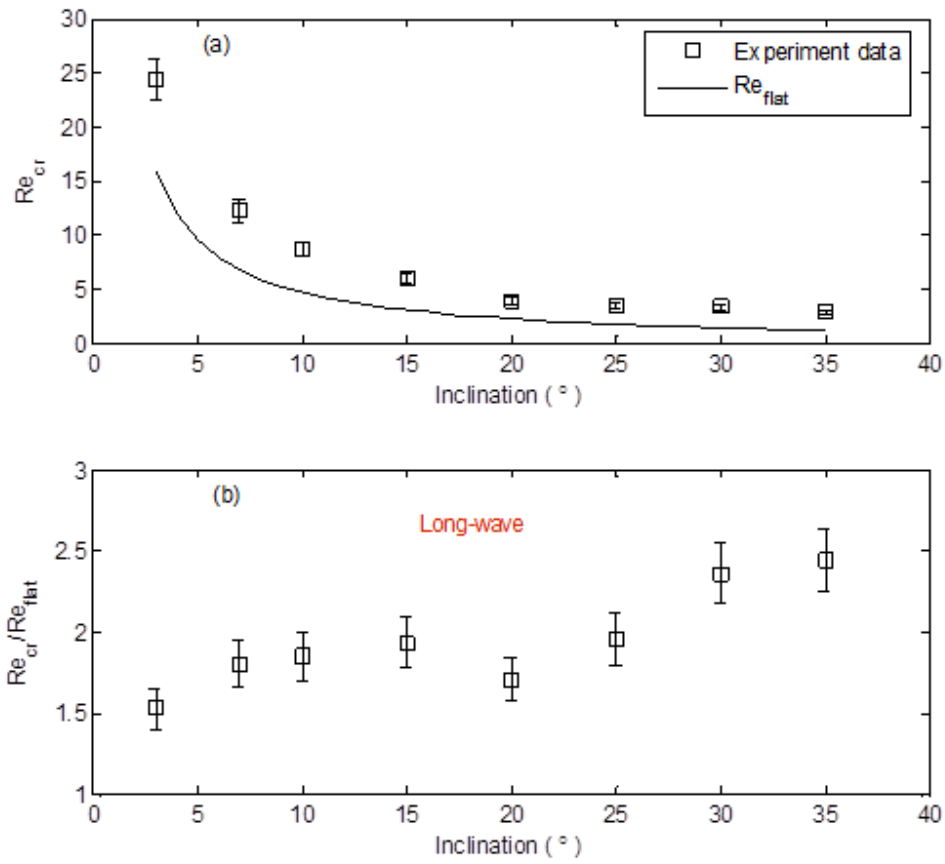


Figure 5.6: Measured (a) and normalized (b) critical Reynolds for the primary instability of liquid film flow along an orthogonal corrugation ($L_b = 9.7$, $A_b = 0.033$). \square , experimental data; —, theoretical prediction for disturbances with infinite wavelength.

5. Effect of corrugated wall steepness

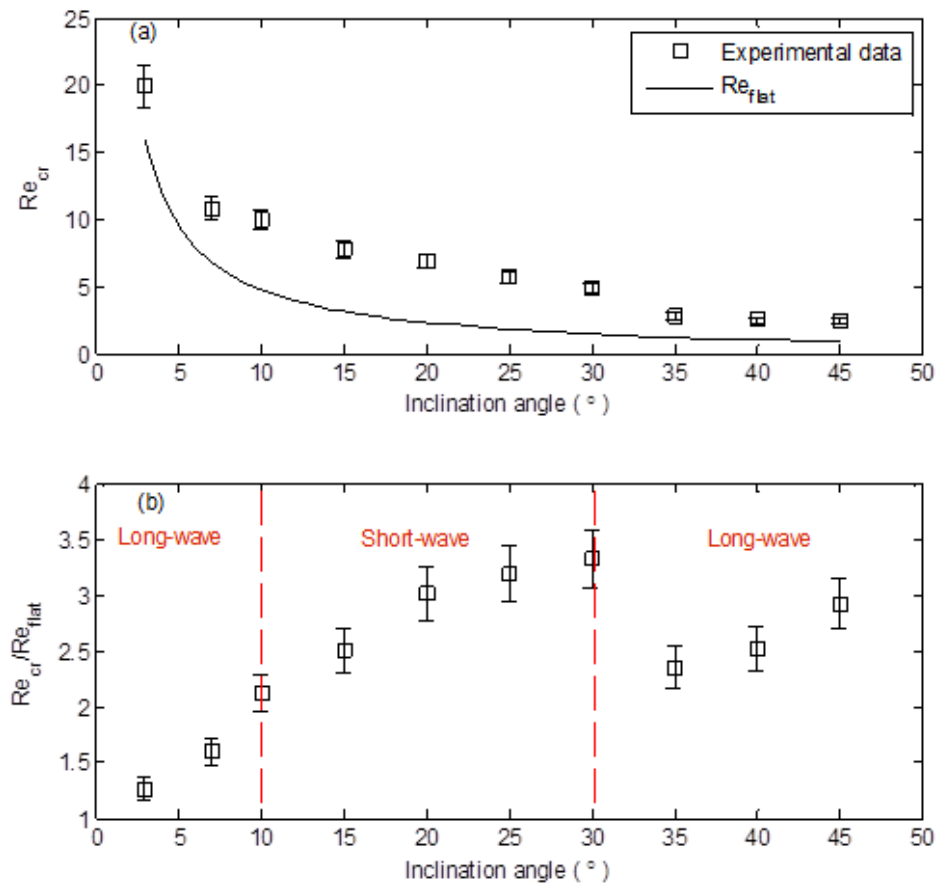


Figure 5.7: Measured (a) and normalized (b) critical Reynolds for the primary instability of liquid film flow along an orthogonal corrugation ($L_b = 4.9$, $A_b = 0.067$). \square , experimental data; —, theoretical prediction for disturbances with infinite wavelength.

5. Effect of corrugated wall steepness

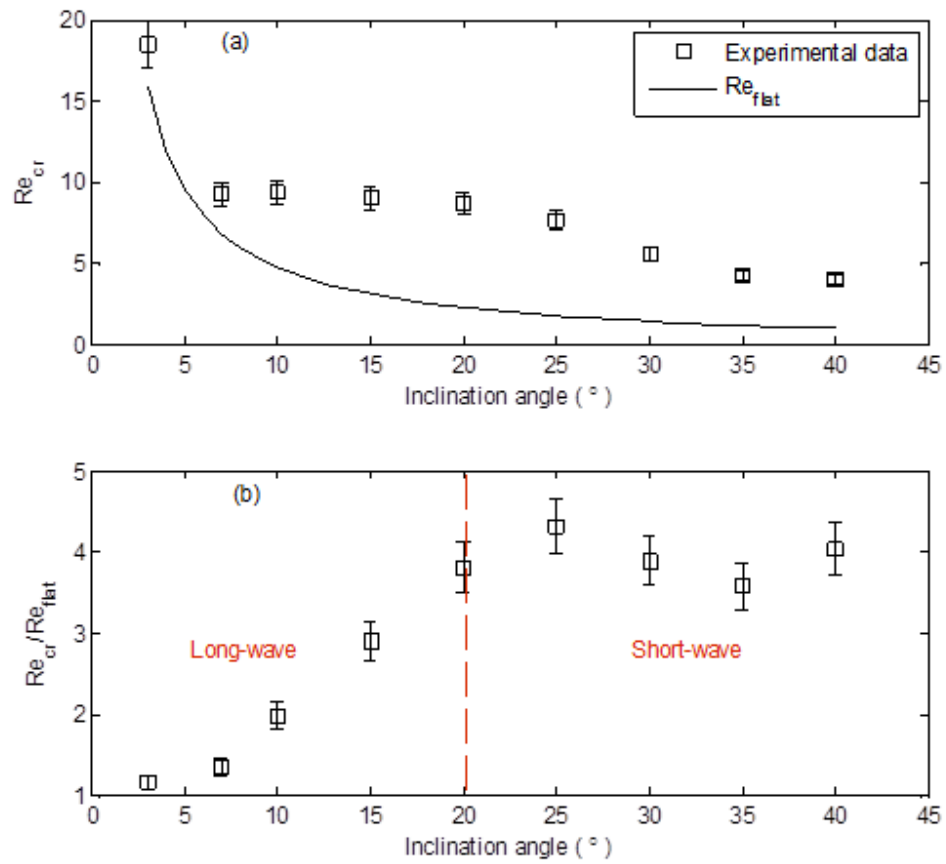


Figure 5.8: Measured (a) and normalized (b) critical Reynolds for the primary instability of liquid film flow along an orthogonal corrugation ($L_b = 4.9$, $A_b = 0.133$). \square , experimental data; —, theoretical prediction for disturbances with infinite wavelength.

5. Effect of corrugated wall steepness

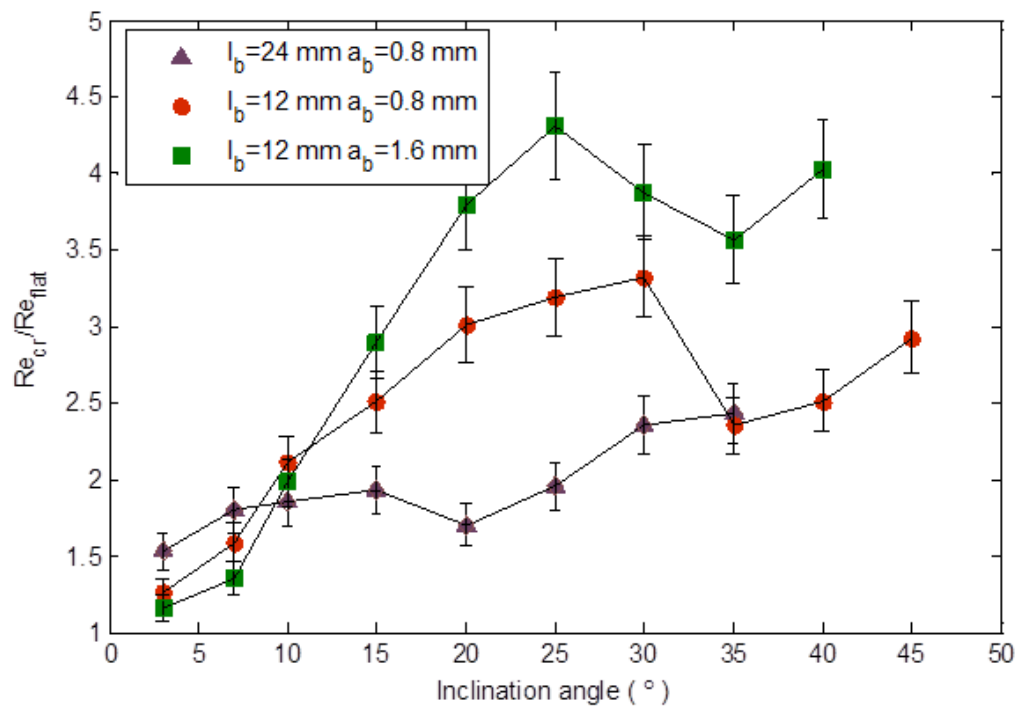


Figure 5.9: Normalized critical Reynolds for the primary instability of liquid film flow along three orthogonal corrugations. ▲, $A_b = 0.033$; ●, $A_b = 0.067$; ■, $A_b = 0.133$

5. Effect of corrugated wall steepness

have been done. For the other limit (with large wavelength and amplitude), on the contrary, only short-wave mode was observed. A stabilizing effect, whose extent is increasing with inclination angles, is found in those corrugations. The intermediate wall corrugation, where the resonance-like phenomenon occurs, exhibits most significant stabilizing effect.

In the case of orthogonal shape, the wavelengths of three tested corrugations are of the same order, but varying the steepness. The instability mode transition is more complicated on orthogonal corrugations, where multiple transitions between long- and short-wave modes can be observed along inclination angles. Generally, the more steep walls lead to higher stability thresholds. However, at the low inclination angles ($\varphi < 7^\circ$), an opposite trend can be observed.

Some preliminary results regarding effect of liquid properties (characterized as Kapitza number) is also provided. An strong dependence on inclination angles is observed. The fluid with lower Kapitza number is more stable at intermediate inclination angle ($5^\circ < \varphi < 10^\circ$), but less stable at both high ($\varphi > 10^\circ$) and low inclination angles ($\varphi \leq 5^\circ$).

Chapter 6

Film flow around a vertical cylinder

6.1 Introduction

This chapter presents a study of liquid film flow along the outer surface of a vertical wavy cylinder. The main result is concerned with the instability of the flow, which will be compared with the inclined case. Moreover, an alternative measurement method that can provide spatial film thickness, is developed. In combination with conductance probes, more comprehensive information of film flow can be obtained. The chapter will be organized as follows:

In section 6.1, the experiment conditions will be described.

In section 6.2, experiment results of film flow over the vertical cylinder will be discussed.

In section 6.3, the principles and procedure of the photographic image processing method will be presented.

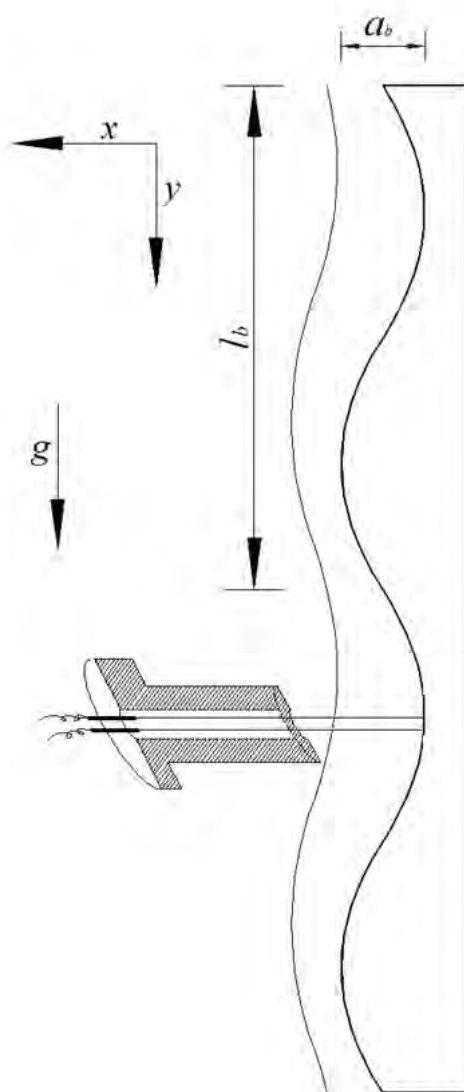


Figure 6.1: Schematic diagram of the film flow test section with the geometric characteristics of the corrugation, and the typical location of a conductance probe.

6.1.1 Experimental conditions

The present experiments are performed on the vertical cylindrical set-up, as described in chapter 3. The wall corrugations are of the sinusoidal shape, with the wavelength, $l_b = 12$ mm, and height, $a_b = 2$ mm, as shown schematically in figure 6.1. The x and y coordinates correspond respectively to the radial (horizontal) and streamwise (vertical) directions. The normalized wavelength L_b and steepness A_b of the wall are $L_b = 4.9$ and $A_b = 0.167$. The liquid used in the experiments is an aqueous glycerol solution with weight percentage around 65% ($\rho = 1.19$ g/cm³, $\nu = 12.324$ mm²/s), and temperature is kept constant at 19 °C (± 0.2 °C). The corresponding Kapitza number in current experiments is of the value, $Ka = 92$.

No external disturbance is introduced into the system, since a small variation in the flow rate is already exists due to the rotation of the gear pump used in this setup. Conductance probes method was employed to record the time signal and detect instability. The design and setting of the method is the same as in chapter 4.

6.2 Experiment Results

In order to detect the instability threshold, two conductance probes are first placed along the channel, respectively 150 mm (upstream) and 650 mm (downstream) from the channel inlet. For vertical case, film flow evolve quickly downstream, therefore, this distance is sufficient to observe the evolution.

The time series of liquid film height are shown in figure 6.2, in which the green (thick) line and red (thin) line corresponds to the location of upstream and downstream, respectively. At low flow rate, take $Re = 1.19$ for instance, a long-wave modulation of the period approximate 3 s can be observed from the time series. This is due to the variation of flow rate from the gear pump, and can be viewed as a low frequency disturbance ($f \approx 0.35$ Hz). As can be observed in the figure, for

6. Film flow around a vertical cylinder

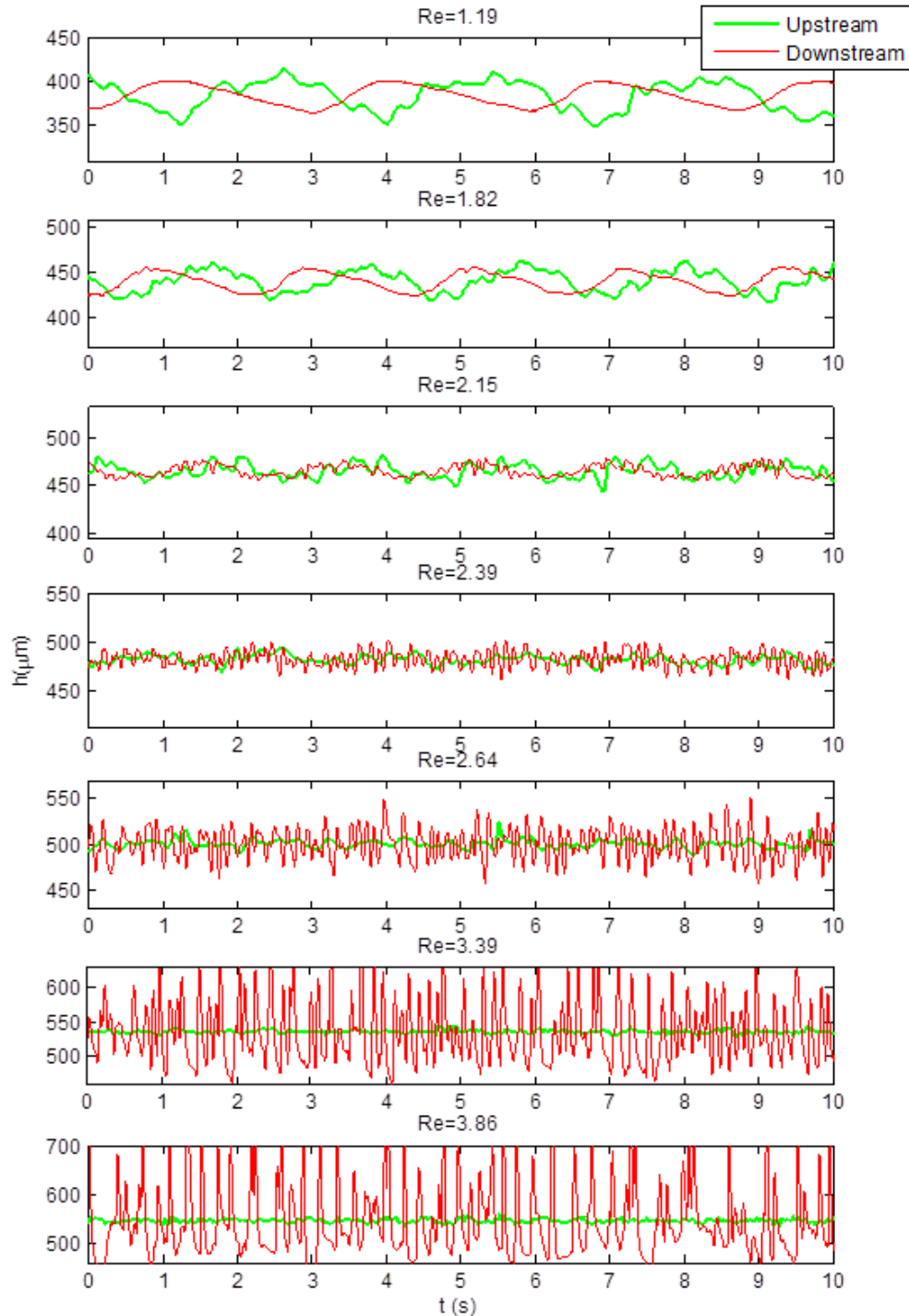


Figure 6.2: Time series of liquid film height (green(thick) line: upstream signal; red(thin) line: downstream signal) on the vertical cylinder, resulting only from ambient noise. The seven plots correspond to Re : 1.19, 1.82, 2.15, 2.39, 2.64, 3.39 and 3.86.

6. Film flow around a vertical cylinder

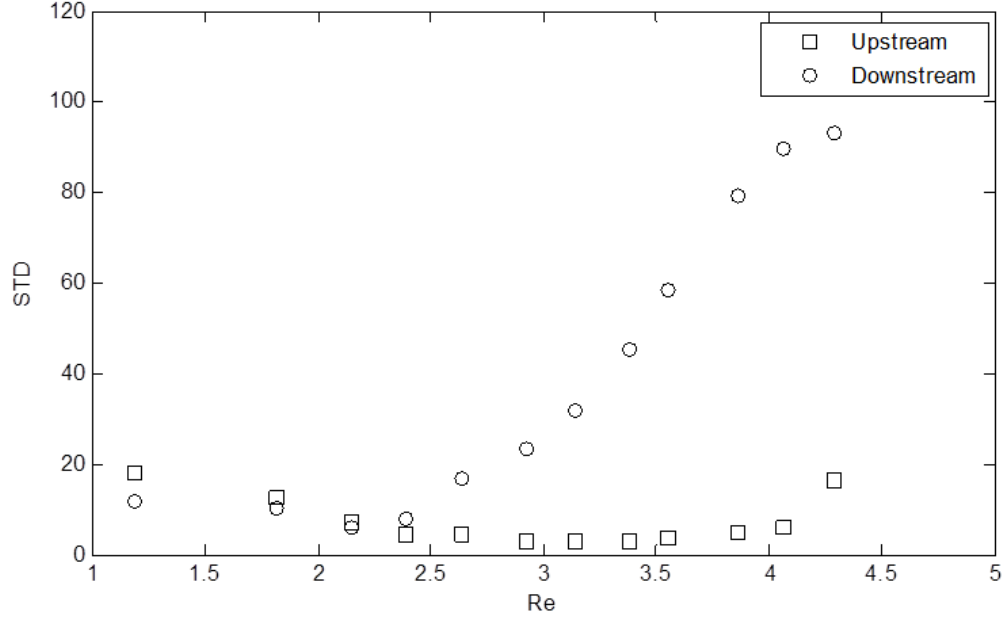


Figure 6.3: Variation of the upstream and downstream standard deviation of time signals with increasing Re .

the first three Re ($Re \leq 2.15$), the disturbances (both the long-wave modulation and and super-posed oscillation) are damped downstream. With increasing Re , the amplitude of small oscillations is amplified, and these oscillations gradually evolve to solitary waves, indicating a short-wave mode. The variations of amplitude measured by the two probes are illustrated further by standard deviation (figure 6.3). The STD at the downstream location is initially smaller than that at the upstream, and the former overtakes the latter at a well-defined threshold (intersection of two curves). At the conditions shown, this corresponds to $Re = 2.3$. According to the theoretical prediction for flat substrate, at inclination angle $\varphi = 90^\circ$, the film will be unstable for any Re , since the critical Re is of the value, $Re = 5/6 \cot \varphi = 0$. The experimental result is qualitatively consistent with Trifonov (2007), who predicts that the flow will remain stable for small Re with sufficiently steep corrugations. Quantitative comparison is not possible due to the difference in liquid solution and geometry of the set-up. The critical Re

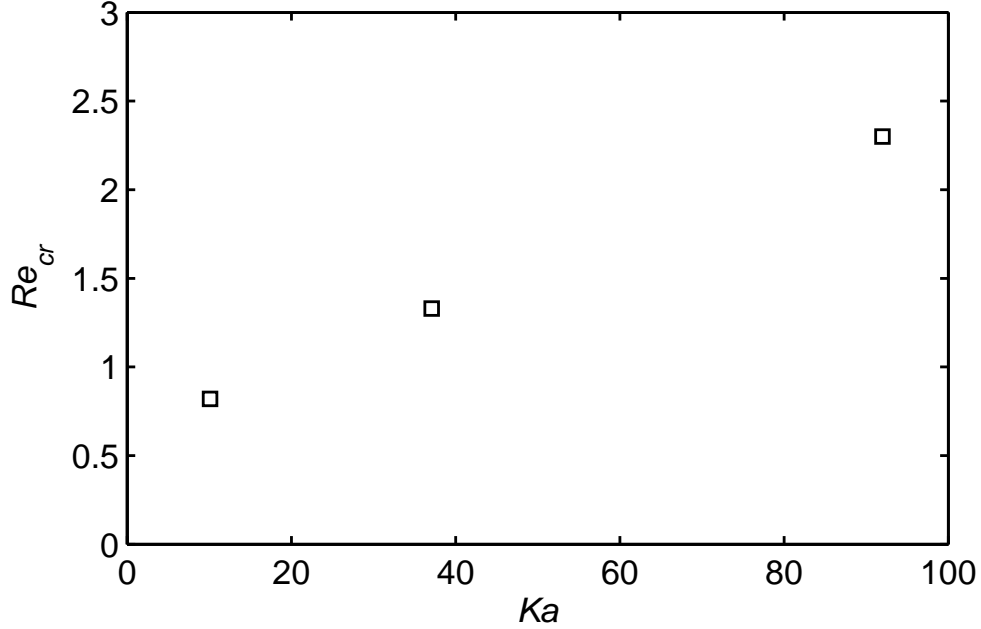


Figure 6.4: Variation of critical Re with Kapitza number. The three points correspond to $Ka = 10.1$, 37.1 (Zioulis, 2011) and 92 .

is also compared with the preliminary results by Zioulis (2011), who performed experiments with two other Kapitza numbers ($Ka = 10.1$ and $Ka = 37.1$) with the same wall. As shown in figure 6.4, the stable regime expands with increasing Ka . Given that Ka represents a comparison of capillary to viscous forces, we argue that the corrugated substrate stabilizes the falling film through the action of capillary forces.

Next, we determine the wavelength and phase velocity of the traveling waves, and compare them with the respective measurements taken in the inclined channel. As the film flow evolves quickly along the vertical cylinder, both probes are placed at locations relatively close to the inlet, where the oscillations remain roughly periodic. The probes are also placed close to each other, more specifically at 175 mm and 199 mm from the inlet. The time lag of waves traveling through the two probes are determined by cross-correlation of the two signals, as shown in figure 6.5a. The phase velocity can then be determined by dividing the distance

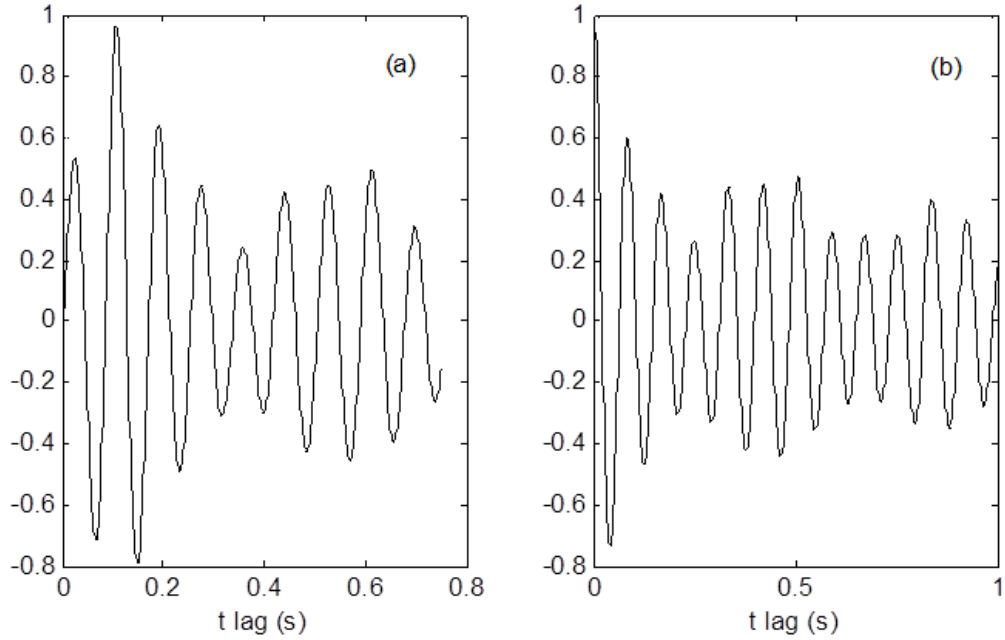


Figure 6.5: a: cross-correlation, and b: autocorrelation of time signal at $Re = 4.07$.

of the two probes with the time-lag. Combined with the auto-correlation of the time signal (figure 6.5b), the wavelength of the traveling wave can be obtained. The parametric evolution of wavelength, l , and phase velocity, c , as function of the deviation from the instability threshold is documented in figure 6.6. The data are non-dimensionalized respectively with the wavelength of the wall, l_b , and the mean Nusselt velocity, u_N . As can be seen from the figure, for increasing Re , the wavelength of the traveling waves increase slightly, from 1.35 times of wall wavelength at onset, and phase velocity remains roughly constant, at a value around 2.5–2.7 times the mean Nusselt velocity.

In chapter 4, it was conjectured that the instability wavelength may approach that of the wall in the limit of vertical channel. However, as plotted in figure 6.7, it turns out that the wavelength remains roughly constant for inclination angles, $\varphi > 35^\circ$. It is worth mentioning that there are small differences in the liquid properties between inclination angles, which may cause the variation in the

6. Film flow around a vertical cylinder

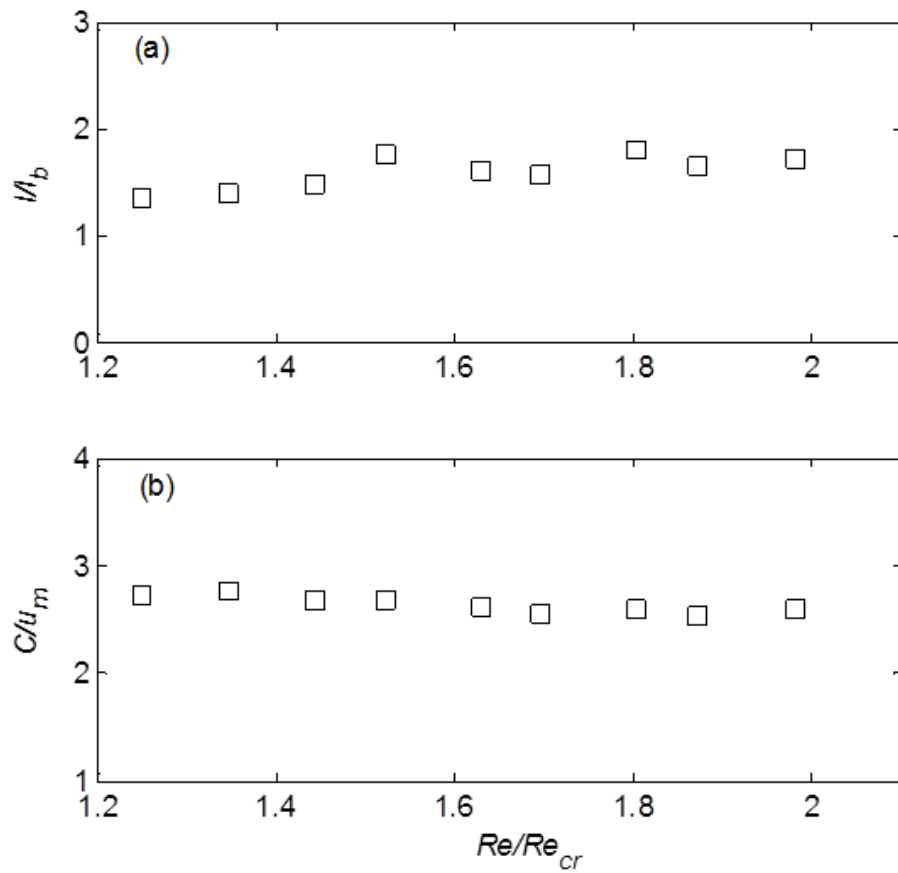


Figure 6.6: a: Variation of wavelength, l/l_b , and b: variation of phase velocity, c/u_N , as a function of Re/Re_{cr}

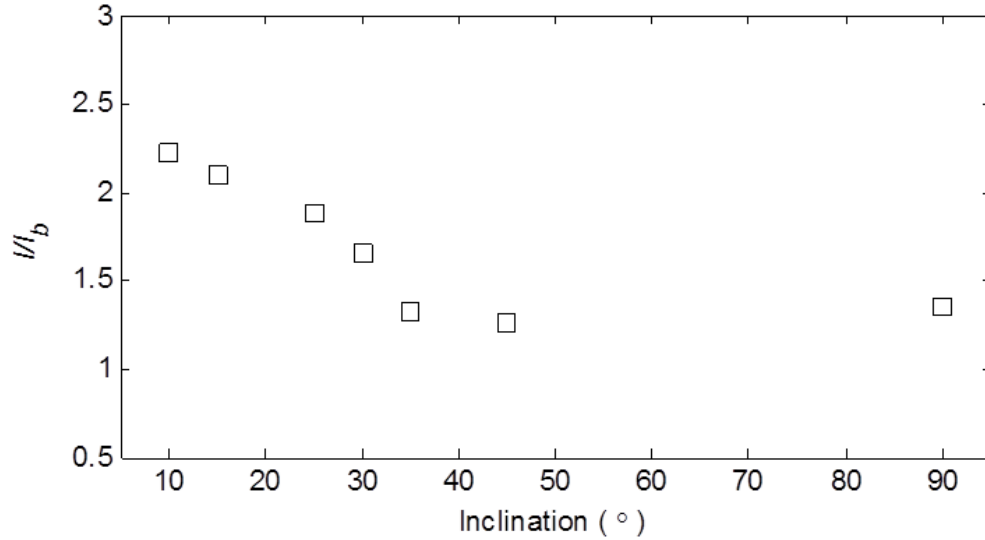


Figure 6.7: Wavelength of the short-wave mode at inception, as function of channel inclination

inception wavelength. The wavelength of instability inception may be to some extent related to the liquid properties. However, due to the time restriction, the effect of liquid properties was not studied in the current project, and it is of evident interest for future investigation.

6.3 Photographic image processing

6.3.1 Principles

The design and setting of the photographic image processing methods has already described in chapter 3. In the following section, we will concentrate on the image processing and result analysis.

The processing of raw images and edge detections were realized by MATLAB. Figure 6.8 represents a typical raw image obtained from the system. The left part, which shows black in the image, is the background, while the white area is the left edge of the vertical cylinder. The quality of the raw image is crucial to

6. Film flow around a vertical cylinder

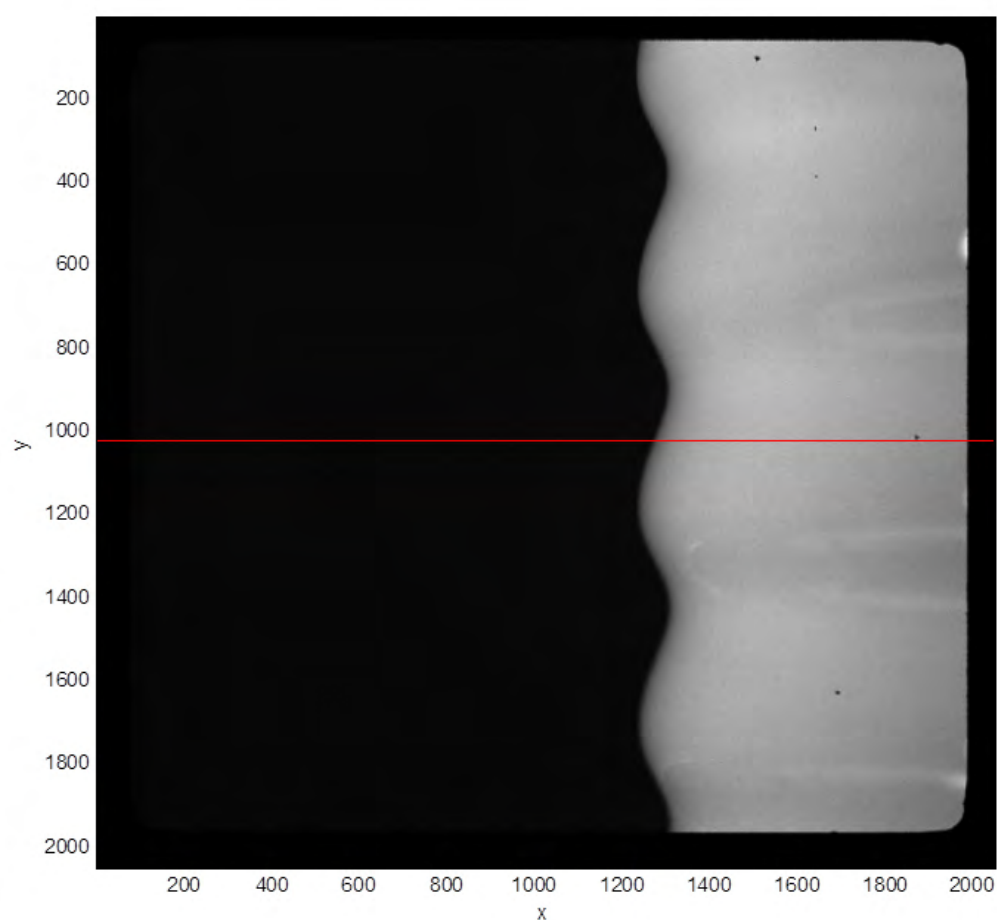


Figure 6.8: A example of raw image taken from the CCD camera (the red line is the mark of a row of pixels, which will be shown in the following text).

the resolution of the final result. Since the edge is composed of the pixels at the boundary that connects two separate regions with varying intensity, the accuracy of edge detection will improve if the contrast of those two regions is enhanced. The intensity variation along the pixels on the red line in figure 6.8, was plotted in figure 6.9. A clear jump in the intensity can be observed at the location $x \approx 1261$, which marks the edge of free surface at corresponding y location. Before edge detection, typically, appropriate image enhancement processes are employed, to convert the image to a form better suited for detection. This is done by analysing the histogram of the raw image, as shown in figure 6.10. Examination of the histogram of the raw image reveals that the dominant two peaks are corresponding to the black and white region in the raw image, and the edge lies between the values 50 and 550. Consequently, applying a window-level contrast stretching function will give a better contrast at the edge, as shown in figure 6.11.

There are two generic methods for edge detection, differential detection and model fitting. In the current study, differential detection is more appropriate. In the approach, a spatial processing is first performed on the original image to produce a differential image with accentuated spatial amplitude changes, and then, a differential detection operation is executed to determine the pixel locations of the maximum differentials. There are several in-built operators of edge detection in Matlab, including both first- and second-order derivative. For methods based on first-order derivative, including Sobel, Prewitt, Roberts and Canny methods, spatial first-order differentiation is first performed, and the resulting edge gradient is compared to a threshold value. The edge will be registered only when the resulting gradient is larger than the threshold. In our result, Canny methods, in which the gradient is calculated using the derivative of a Gaussian filter, shows reasonable accuracy and is employed.

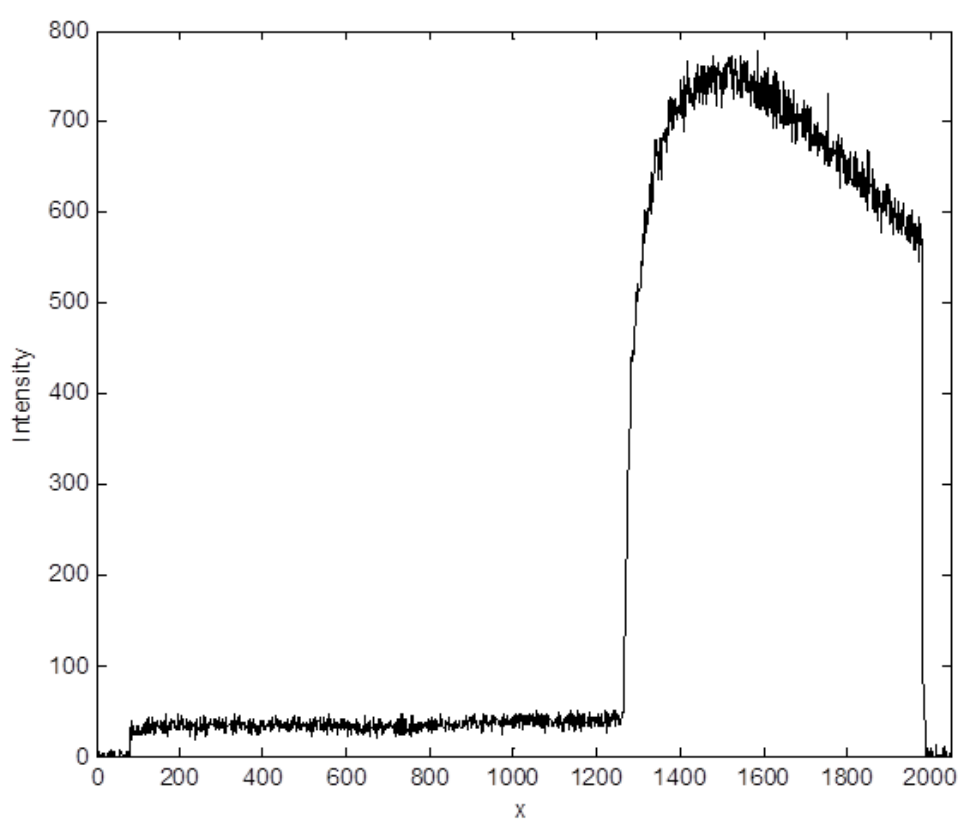


Figure 6.9: The intensity variation along a row of pixels, corresponding to the red line in figure 6.8

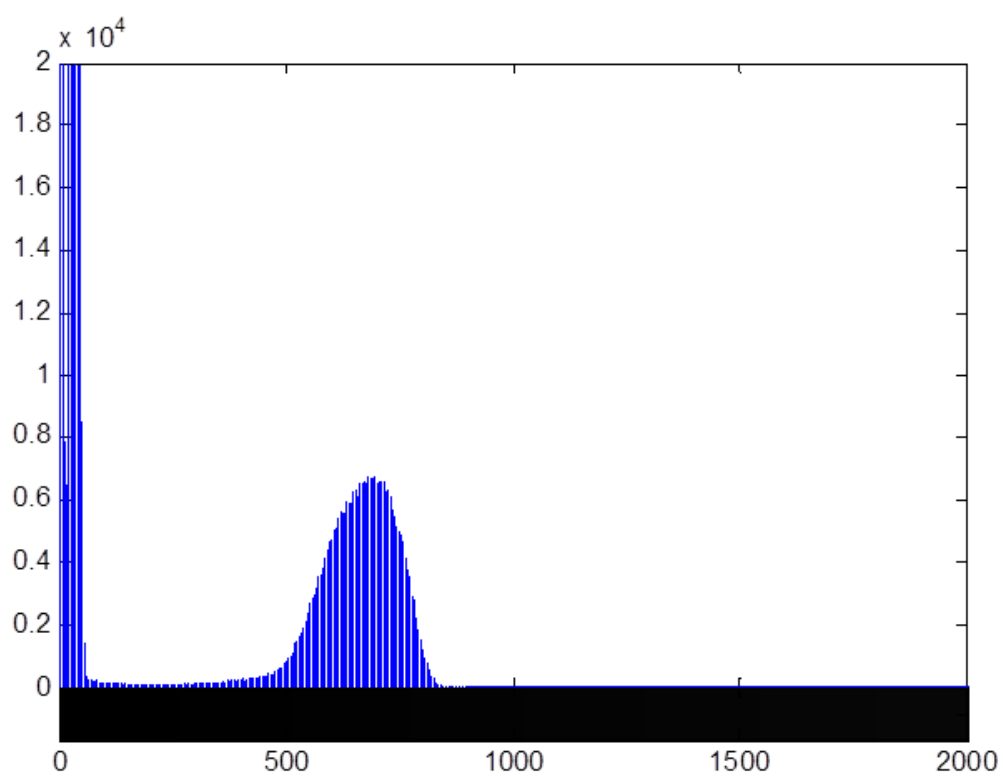


Figure 6.10: The histogram of the raw image

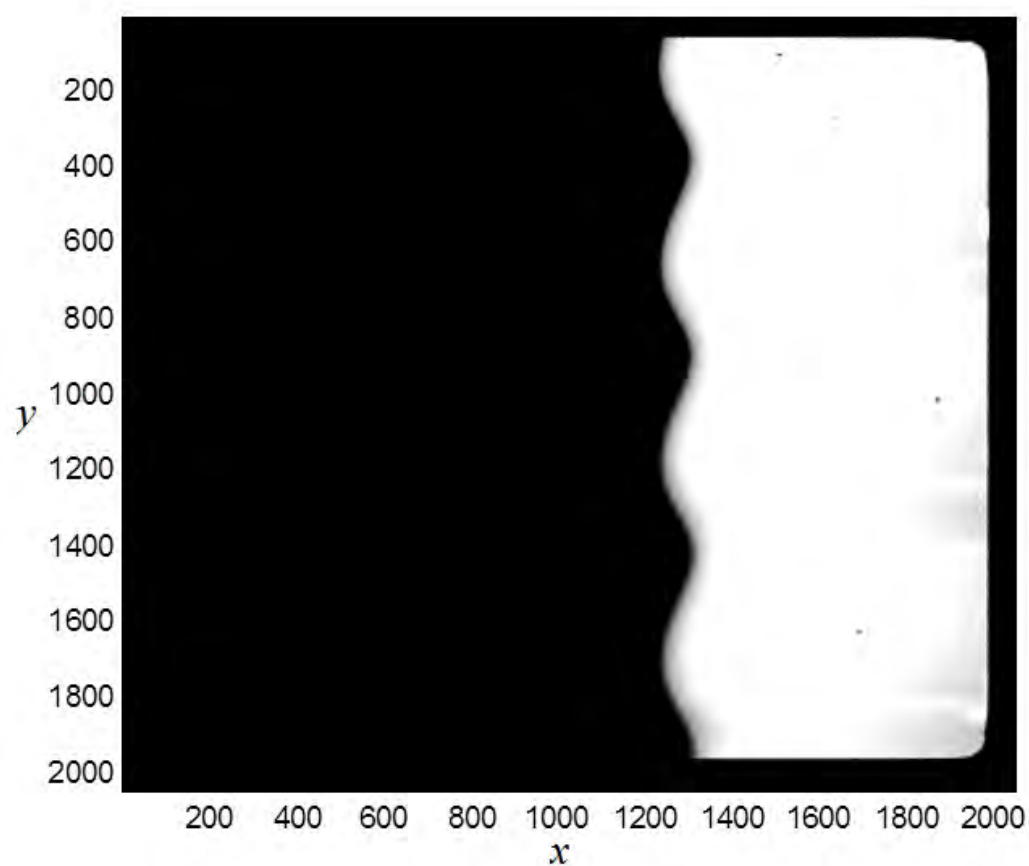


Figure 6.11: The processed image by applying a window-level contrast stretching function

6.3.2 Image processing procedure

In this section, the step of image processing will be introduced. The raw image, which has been shown in figure 6.8, will be used as an example.

Step 1: Crop. The region of interest, which contained the edge of the wall and the free surface, will be selected. This step can reduce the unnecessary processing of the large region of the background and wall away from the edge, and also can avoid some defects of the image, which is not relevant to the edge. The processed image is shown in figure 6.12.

Step 2: Median filter and Image enhancement. A 1×3 median filter is applied to every row of the image, to reduce single-pixel noise and preserving the interfacial edge. The image then is analysed based on its histogram, and adjusted accordingly, to increase the contrast at the edge. This step is usually done manually. In practice, for low flow rate, the interfacial edge is cleared displayed. The edge can be well defined even without the enhancement step.

Step 3: Edge detection The enhanced image is proceed to edge detection using Canny method. Keep in mind that, the free surface is a smooth and continuous line. When multiple edges are found, the edge on the left is usually the real interface. The real edge is expected to be a smooth continuous line. The detected free surface is re-plotted in the raw image in the red, as shown in figure 6.13.

Step 4: Calibration and data analysis. The calibration is done by measuring the number of pixels of known distance, e.g. the wavelength of the corrugation without film flow. Next, the free surface profile can be converted into dimensional scales, as illustrated in figure 6.14. Similar detection method can be employed to the images of wall substrate, without film flow. Since the camera is fixed at same location, therefore, the film distribution along the wall can be obtained (figure 6.15). Some other information can be derived from the free surface profile: for instance, the wave number of the free surface can be obtained by auto-correlation, which is shown in figure 6.16.

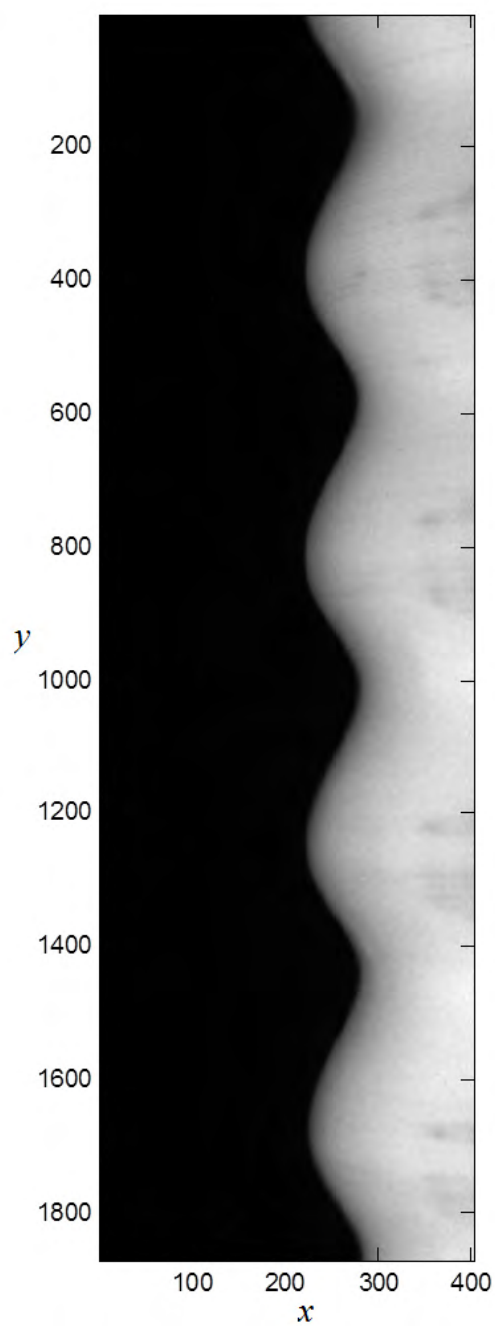


Figure 6.12: The processed image after step 1

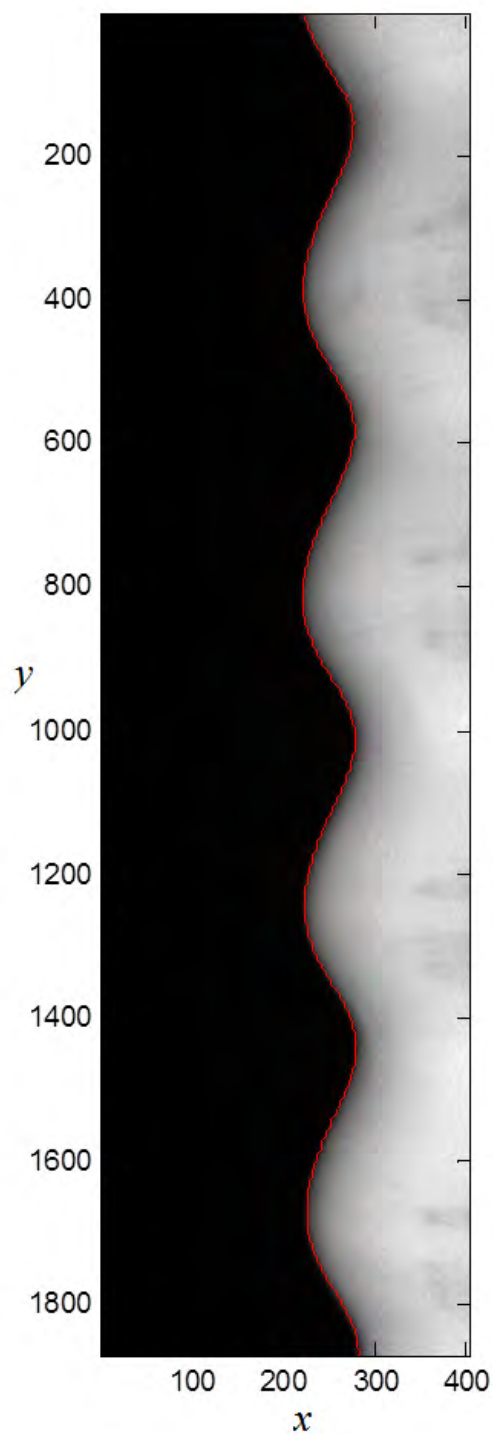


Figure 6.13: An example of edge detection. The red line corresponds to the detected edge using Canny method.

6. Film flow around a vertical cylinder

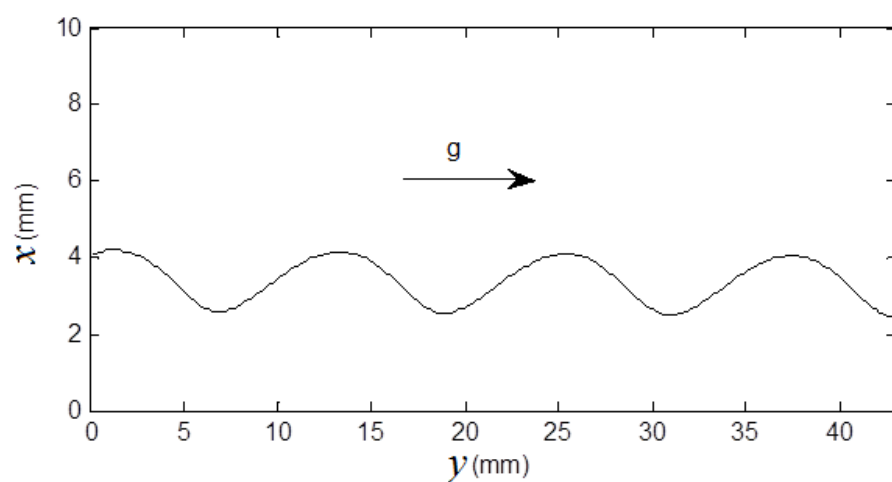


Figure 6.14: Free surface profile obtained by calibration

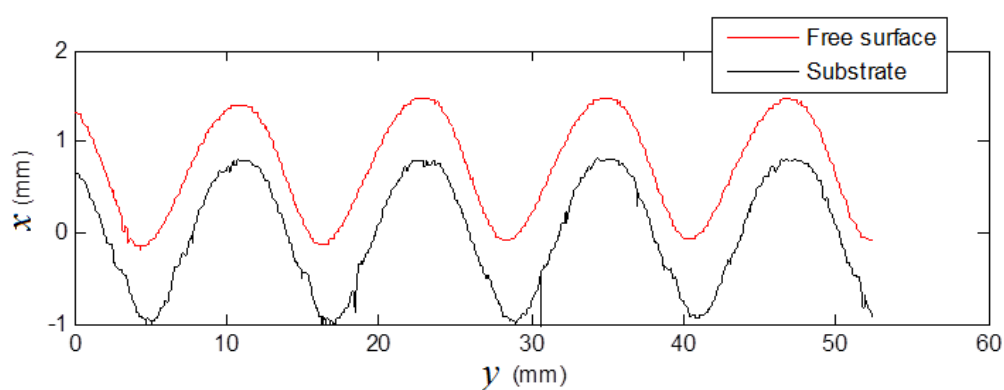


Figure 6.15: Spatial film thickness determined by image processing

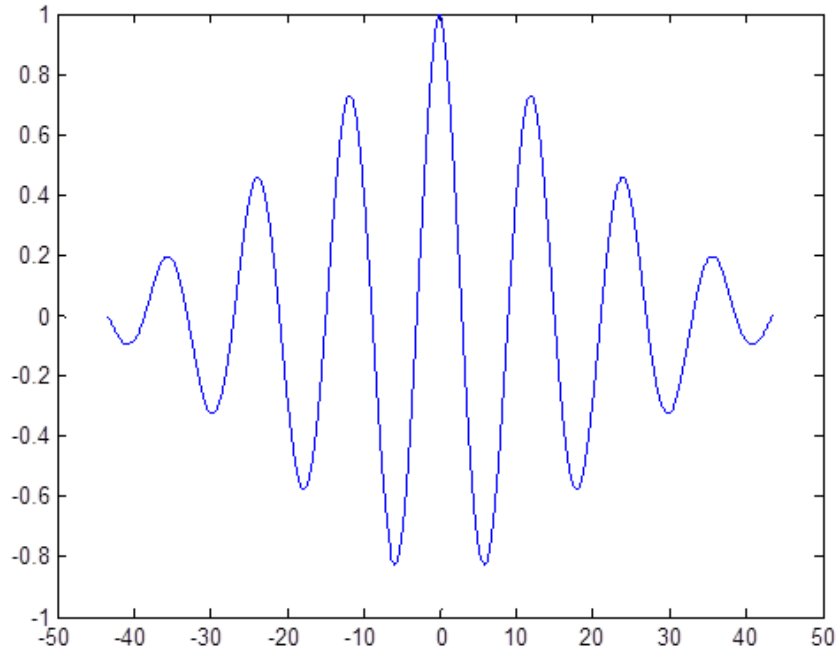


Figure 6.16: Auto-correlation of spatial film thickness

6.3.3 Restriction of methods

The application of the technique is evidently limited by the high flow rate, when the flow loses its symmetry and three-dimensional solitary waves start to appear on the surface. Moreover, a spurious edge might be detected due to the three-dimensional traveling waves, since the height of free surface before/behind might be higher than at the measurement location, and shown as a blurred edge in the image. Thus, a laser-induced system is necessary for this case, as only the location of interest will be illuminated by the laser. If information of flow field is required, a PIV system is then appropriate.

6.4 Summary and discussion

Although various wall geometries are available, investigation is only performed on one corrugation with one liquid solution due to the time restriction. The primary

6. Film flow around a vertical cylinder

instability is found to be a short-wave mode, which is the same as on the inclined channel. The onset wavelength of primary instability is roughly the same as that on inclined channel at high inclinations ($\varphi > 35^\circ$). The wavelength might depend on the liquid properties and has to be investigated in the future. Compared to film over flat substrate, a stabilizing effect was observed in the experiment, and results in a finite critical Re , which is qualitatively consistent with the prediction by Trifonov (2007).

In addition, a measurement technique based on direct photography is proposed for film thickness and free surface profile detection. By using a normal illumination and black background, the free surface can be determined from the processing of the flow image. The measurement frequency of the method is up to 14.5 Hz.

Some drawbacks in terms of the set-up is observed during the experiments, which can be improved in the future. As seen from the current experiment, the pump introduced a low frequency variation in the flow rate. Since the liquid film is very sensitive to the external perturbation, the variation is quite significant in the film flow and dominates at low flow rate. This may cover some important intrinsic characteristics, and thus is worth alleviating by replacing the pump with a smoother one. A better way to tackle the drawback is overflow tank on the top of the system, which can generate a more stable flow rate. Moreover, the interior compartment can be enlarged and filled with a porous medium, which will ensure smoother entrance of the liquid and more uniform distribution along the cylinder circumference.

Chapter 7

An oscillatory behaviour at low Re

7.1 Introduction

It is well known that film flow over a flat substrate is considered convectively unstable, namely, all the disturbances are amplified spatially, and the flow is supposed to become more stable with decreasing Re . However, in the case of steep orthogonal corrugation at high inclination angle ($\varphi = 40^\circ$ and 45°), an interesting oscillatory behaviour is observed at low Reynolds number. The amplitude of disturbance no longer varies monotonically with the control parameter, Re : the oscillation will not disappear with decreasing Re , on the contrary, the magnitude of oscillation increases until film raptures. In this chapter, experimental results of this oscillatory behaviour will be presented and discussed.

The liquid used in the current experiments is aqueous glycerol solution, with different concentration (from 55%–78%). The temperature varies slightly between different experimental campaigns. Similarly, Kapitza number is used to characterize the liquid properties.

7.2 Characteristic of the oscillatory instability

The behaviour occurs on two orthogonally corrugated walls, which are of the same wavelength, $l_b = 12$ mm and different amplitudes, $a_b = 1.6$ mm and $a_b = 2.0$ mm. Figure 7.1 shows upstream and downstream signal for $\varphi = 45^\circ$, with decreasing Re ($a_b = 1.6$ mm). The two probes are placed along the centreline, at distances respectively 15 mm and 550 mm from the inlet. No inlet perturbation was introduced, and the flow is only subject to ambient noise. As can be seen in the figure, at first, when the flow rate is high ($Re = 4.49$), traveling waves have been developed and amplified downstream. With decreasing Re , the magnitude of traveling waves, which are detected downstream, gradually decreases, and the waves finally disappear at $Re = 3.15$. The variation manifests the typical transition from the unstable regime to a stable regime, which has been discussed in chapter 4. However, when the flowrate is reduced further ($Re < 2.26$), the free surface at downstream deviates from its steady state and starts to oscillate. This oscillation is more remarkable with lower Re , and found to be sustainable and is not vanishing even at very small Re .

This phenomenon can be further demonstrated by figure 7.2, where standard deviation (STD) is used to quantify the magnitude of the free surface deformation. For probe 1, which is located upstream close to flow inlet, the value of STD remains approximately zero (small deviation due to the signal noise) for $Re < 3.2$, and slightly increases with Re for $Re \geq 3.2$. In the case of probe 2, which is placed at downstream of the channel, the magnitude of STD is close to zero for $Re \approx 3$, which indicates a steady state of free surface. For Re above 3.5, it is reasonable to attribute the growth of STD to the development of the short-wave instability. The branch with decreasing Re manifests the remarkable growth of oscillation at low flowrate.

Initially, the oscillation first appears at the very end of the channel, and, with decreasing Re , the area of oscillation gradually expands upstream and occupies a larger part of the channel. This cannot be shown directly by conductance probe,

7. An oscillatory behaviour at low Re

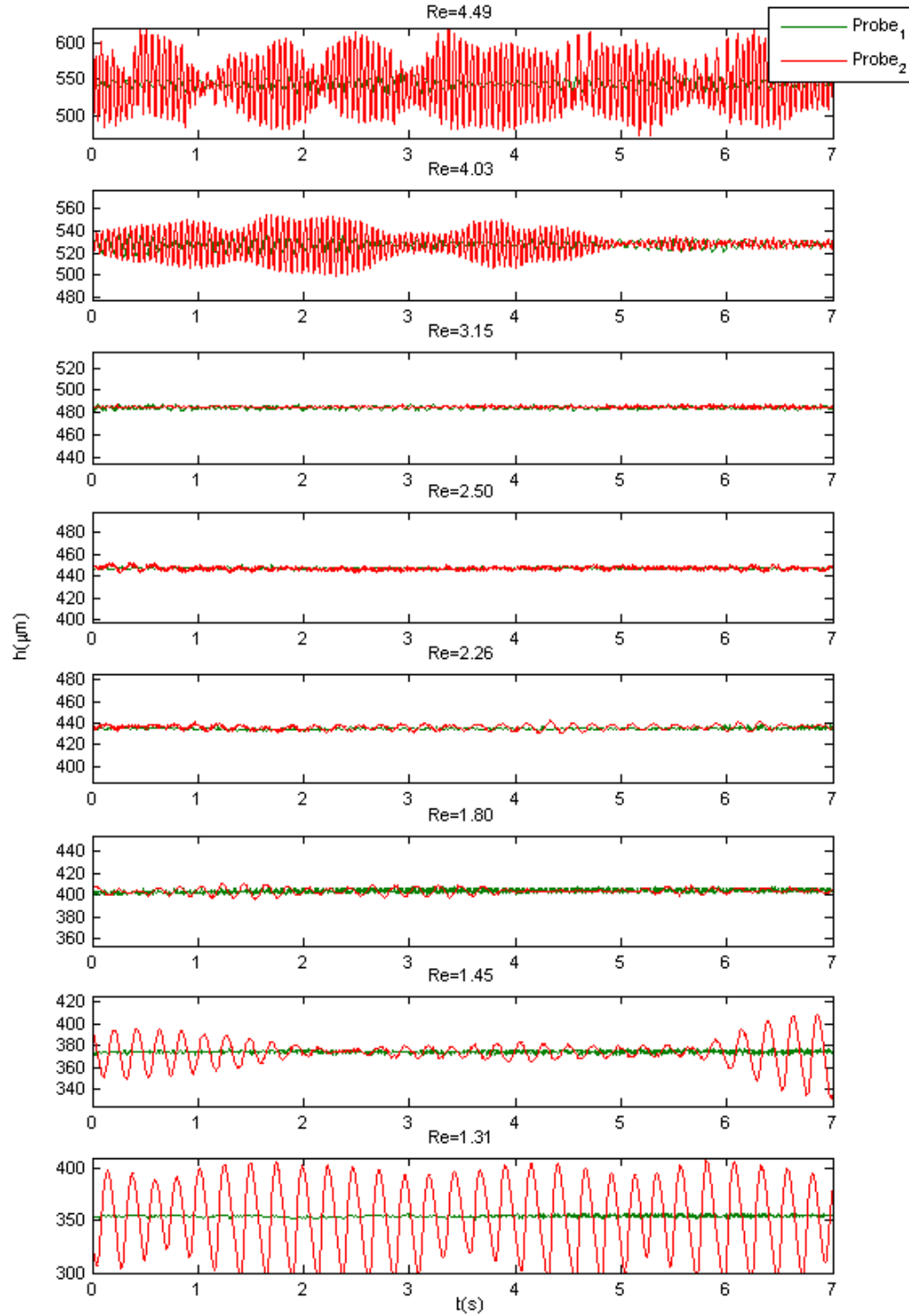


Figure 7.1: Time series of liquid height on an orthogonally corrugated wall ($l_b = 12$ mm $a_b = 1.6$ mm) at inclination $\varphi = 45^\circ$ ($Ka = 137$). Green (thick) and red line are respectively corresponds to upstream and downstream signal

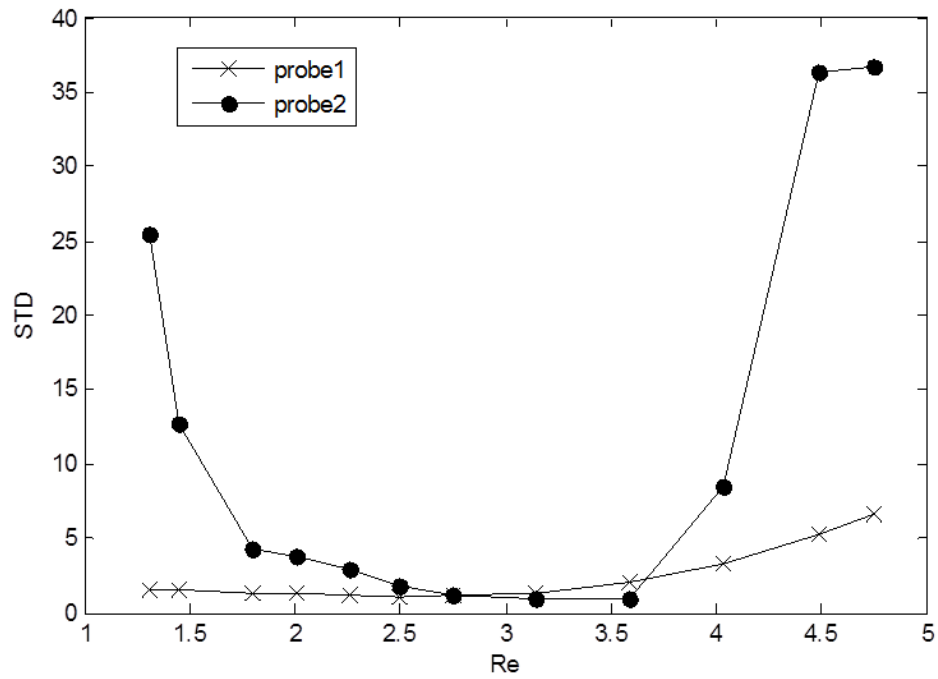


Figure 7.2: Variation of standard deviation of time signals with Re on an orthogonally corrugated wall ($l_b = 12$ mm $a_b = 1.6$ mm) at $\varphi = 45^\circ$ ($Ka = 137$).

since it is incapable to provide spatial measurement. However, indirect evidence can be provided by comparing time signals from multiple conductance probes. Three probes are placed at the bottom of the channel, which are respectively 370 mm, 430 mm and 485 mm from the onset of the corrugation. Time series of four different Re with descending order, is plotted in figure 7.3. The free surface is originally steady in all three locations at $Re = 3.40$. For $Re = 2.46$, slight oscillation can be observed at the probe 3, which is placed near the end of the channel. With further decreasing of flow rate ($Re = 1.66$), oscillation spreads to all the area of three probes, but is most significant at probe 3. Finally, in the case of $Re = 1.44$, the oscillation is remarkable in both probes 2 and 3, moreover, in some time period, the oscillation is even stronger at probe 2 than probe 3.

The oscillation has an intrinsic frequency, which is insensitive to the (much lower) external disturbance. The film flow with low frequency external disturbance, $f = 0.167$ Hz, is shown in figure 7.4. The inlet disturbances are modulated by the oscillation, and downstream, the oscillation dominates the dynamics of free surface. The fast Fourier Transform (FFT) of time-signals, with and without external disturbances, are shown in figure 7.5. In both figures, a dominant peak around $f = 5$ Hz is evident, which corresponds to the oscillatory phenomenon. The frequency increases slightly with the Re , as illustrated in figure 7.6, where the results of two corrugations and various percentages of glycerol solution are presented. However, the oscillation is very sensitive to the gradual change of flow rate, as show in figure 7.7. A significant magnification oscillation can be observed, when the Re is changed from 1.78 to 1.59. In comparison, film flow with single long-wave pulse was presented in figure 7.8.

The wavelength of the oscillation is obtained by correlating time signals of two probes, which are placed 48 mm apart, respectively 424 mm and 472 mm from onset of corrugation. By taking the cross-correlation of the two signals (figure 7.9a), we can computer the time-lag, and further obtain the mean phase velocity. In combination with the frequency that obtained from auto-correlation

7. An oscillatory behaviour at low Re

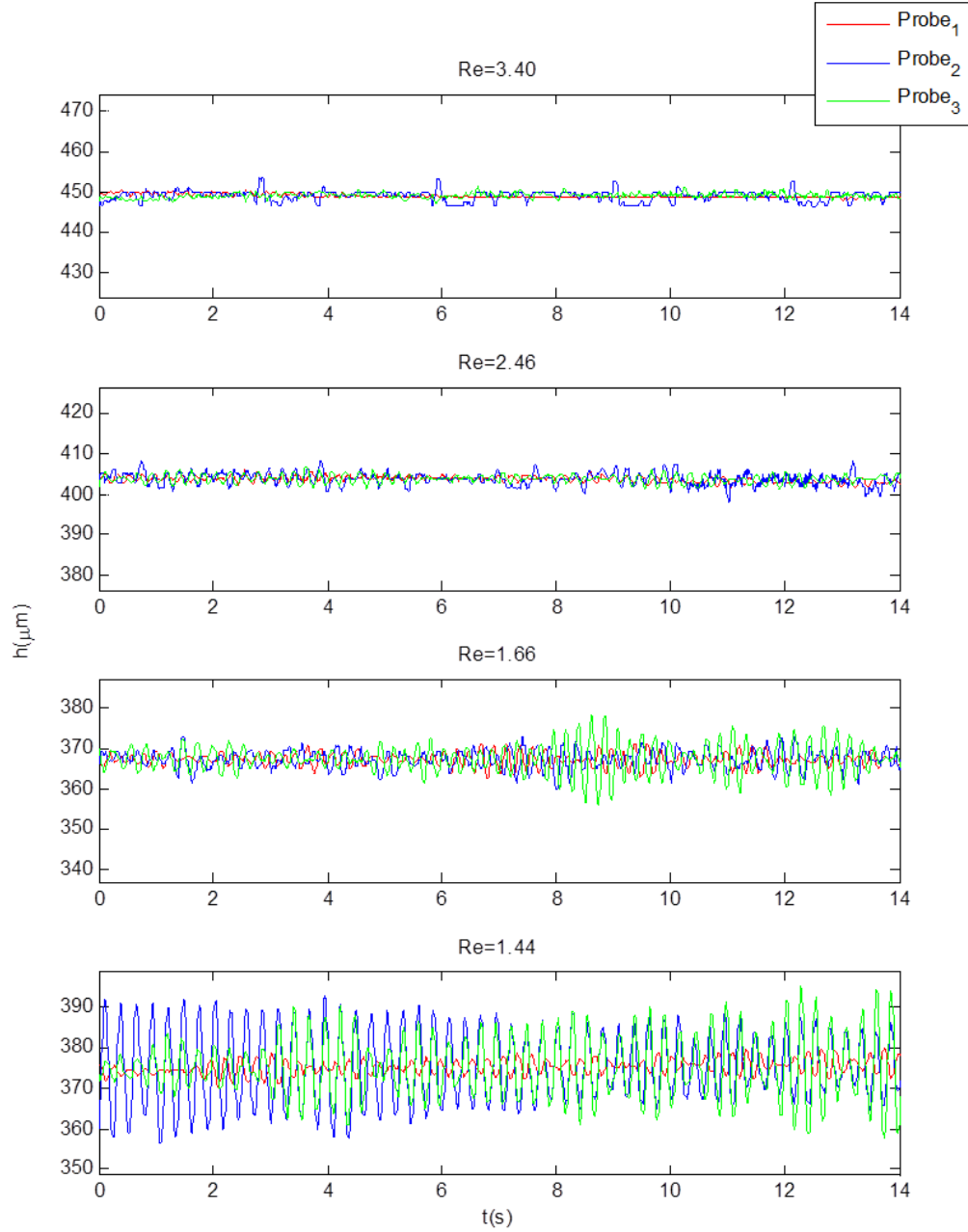


Figure 7.3: Time series of liquid height on an orthogonally corrugated wall ($l_b=12$ mm $a_b=2.0$ mm) at $\varphi=45^\circ$ ($Ka=169$). Red, blue and green line are respectively 370 mm, 430 mm and 485 mm from the onset of the corrugation.

7. An oscillatory behaviour at low Re

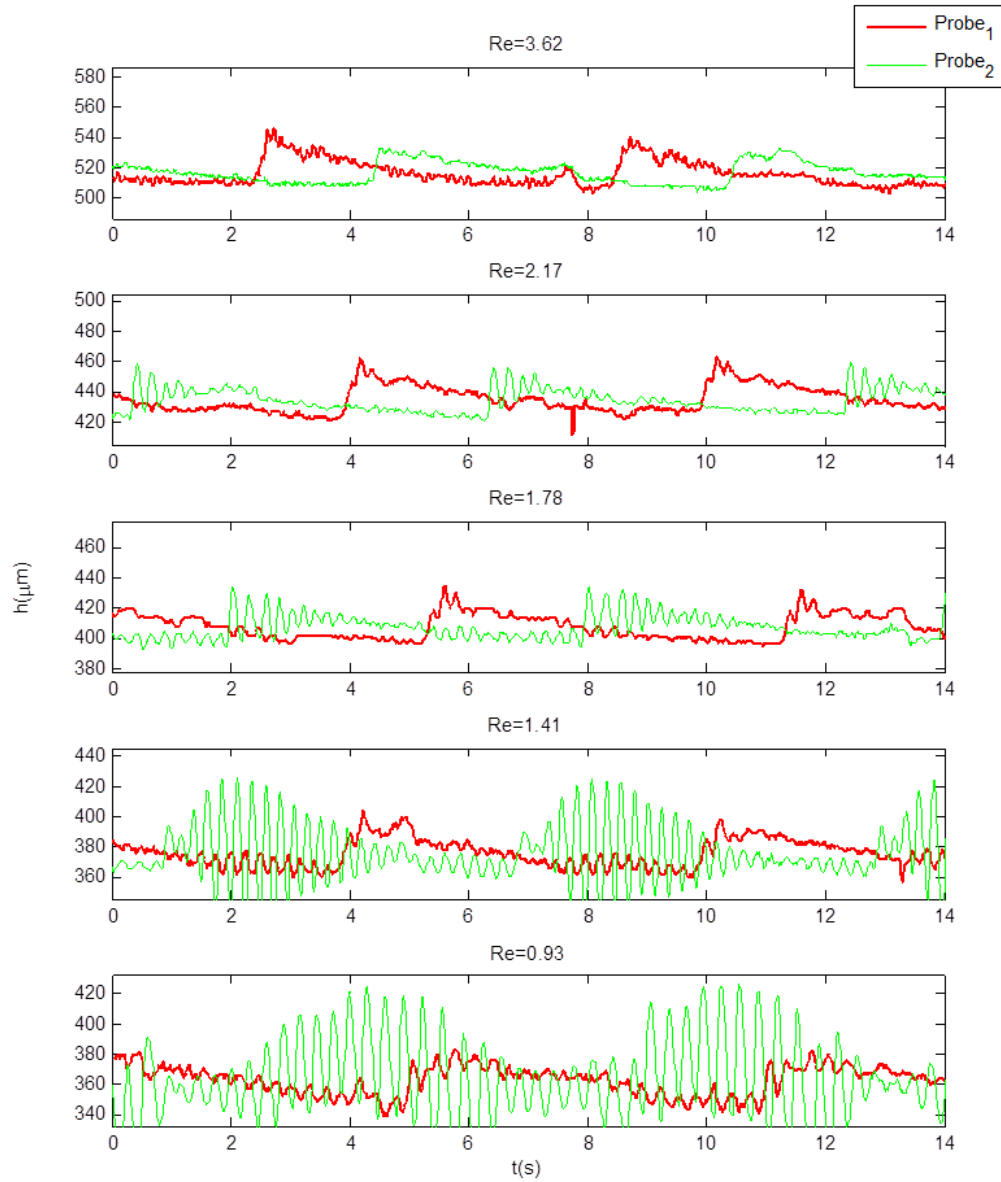


Figure 7.4: Time series of liquid height on an orthogonally corrugated wall with low-frequency disturbance ($l_b = 12$ mm $a_b = 2.0$ mm) at $\varphi = 45^\circ$ ($Ka = 134$).

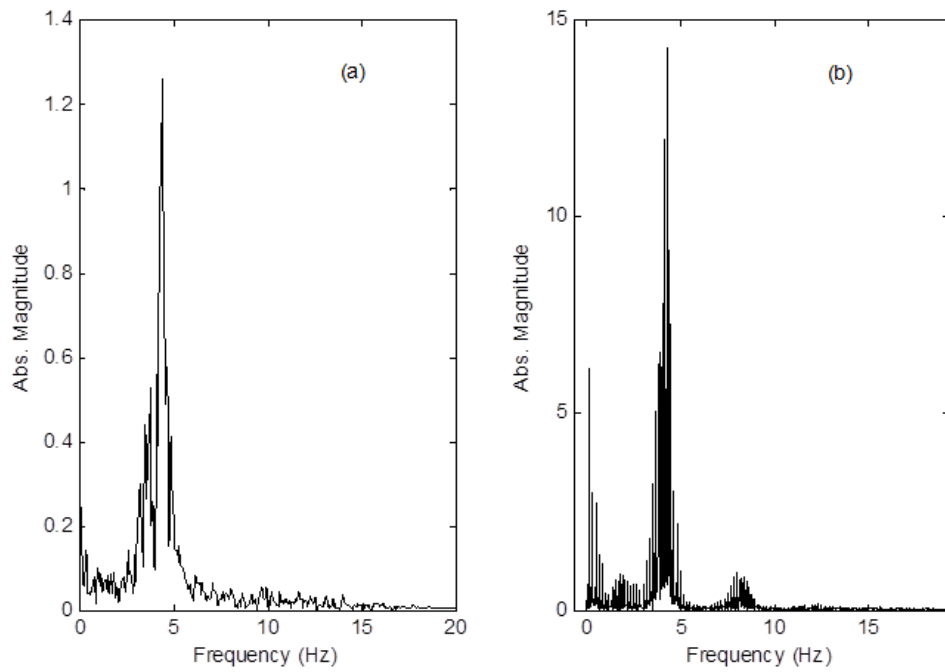


Figure 7.5: Fast Fourier Transform of a time signal without (a) and with (b) inlet disturbance. ($Ka = 134$, $l_b = 12$ mm $a_b = 2.0$ mm). $Re = 1.83$ (a); $Re = 1.41$ (b)

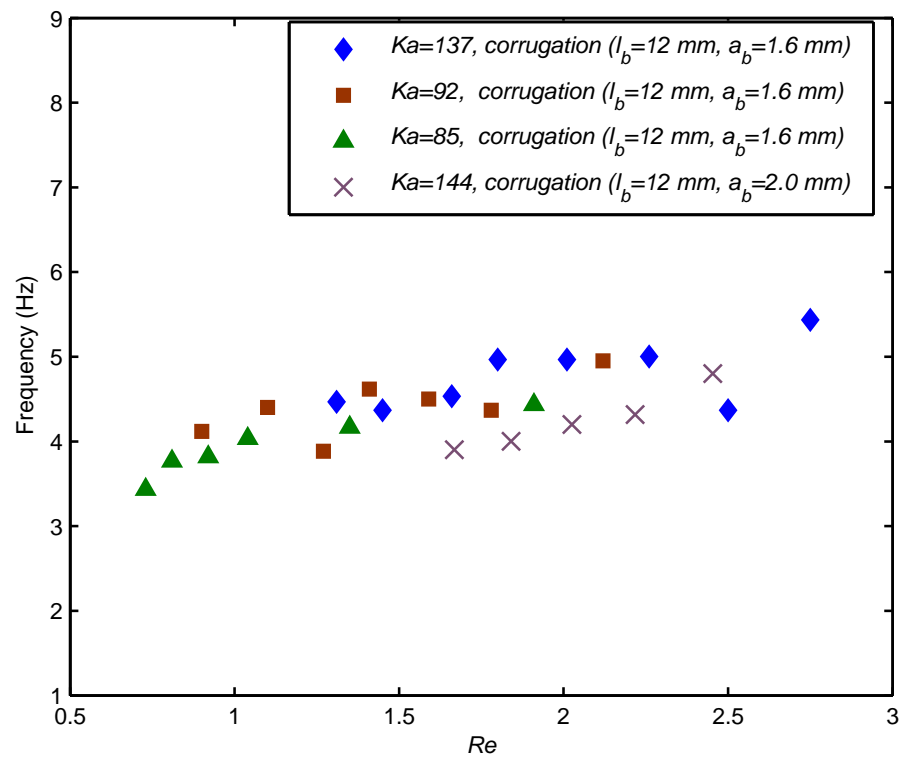


Figure 7.6: The frequency of oscillation VS Re at two different orthogonal corrugations

7. An oscillatory behaviour at low Re

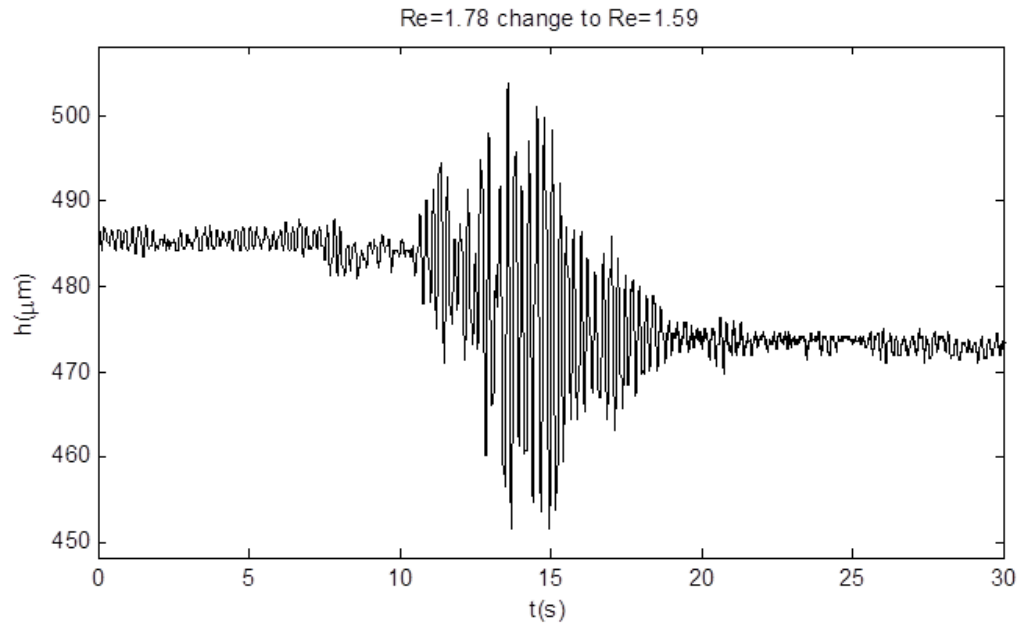


Figure 7.7: Time series of liquid height with the condition of changing Re from 1.78 to 1.59

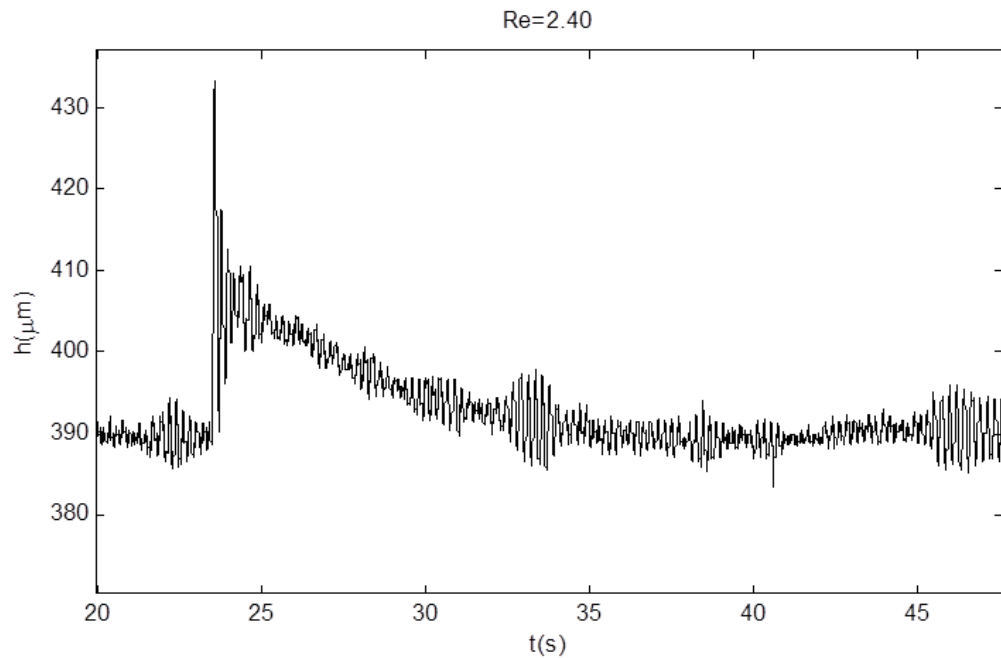


Figure 7.8: Time series of liquid height with a pulse disturbance at $Re = 2.40$

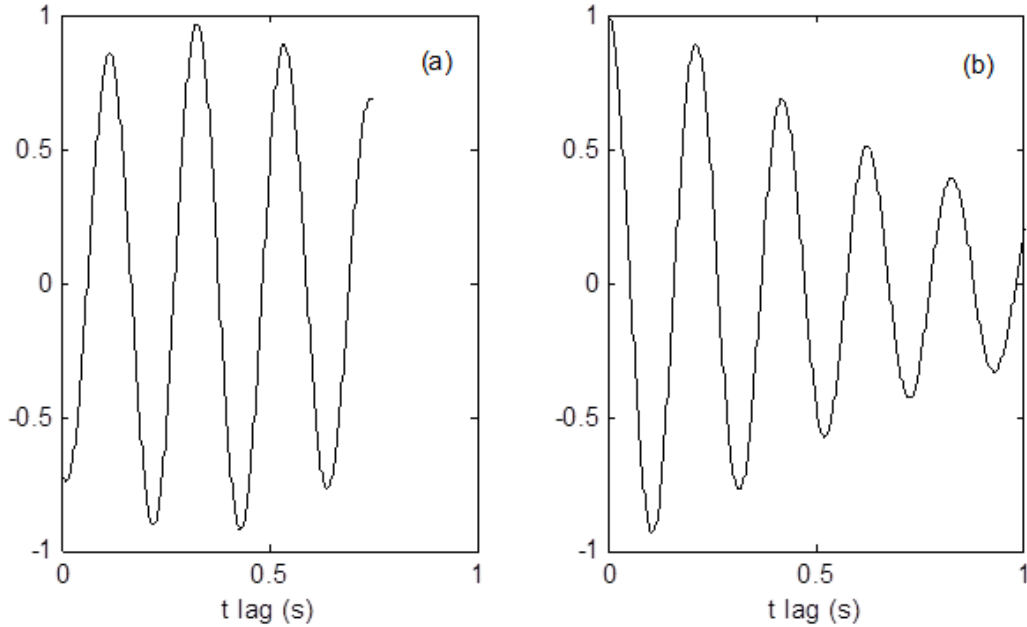


Figure 7.9: a: cross-correlation, and b: autocorrelation of a time signal at $Re = 2.06$ ($a_b = 1.6$ mm, $\varphi = 45^\circ$)

(figure 7.9b), the wavelength of the oscillation can be determined. The wavelength of oscillation at different Re is presented in figure 7.10 the wavelength remain approximately 30 mm under current conditions.

7.3 Occurrence of oscillation

As mentioned, the oscillation was first observed on orthogonal wall at high inclination angles. A question of evident interest is that whether it occurs in other experimental conditions, including different wall geometries, liquid properties inclination angles and etc.

We first consider the method to determine the occurrence of the oscillation. A straight-forward way is to perform measurements at gradually smaller Re : by observing the time series and its fast Fourier Transform, we can determine the state of free surface. However, because of practical difficulties with film rupture,

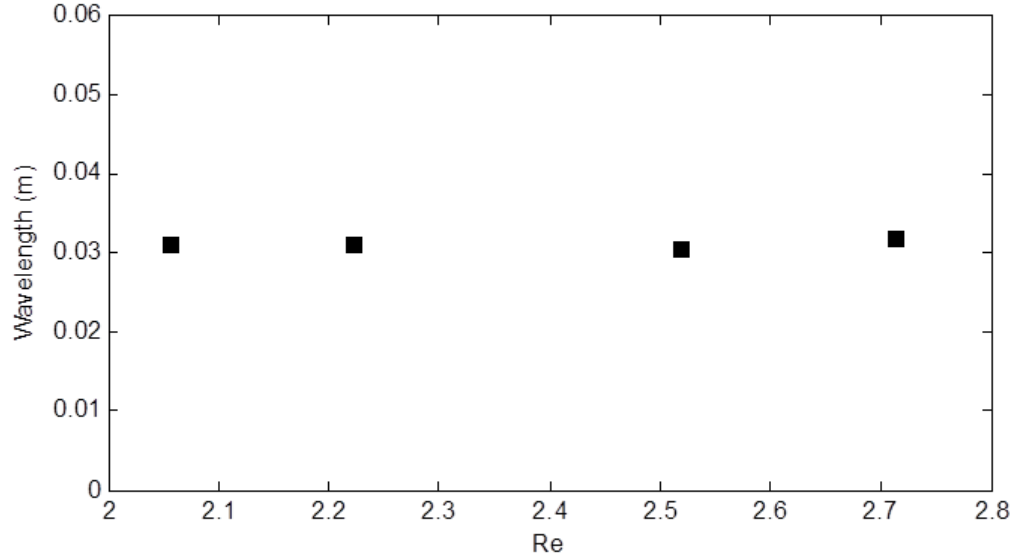


Figure 7.10: The wavelength of oscillation at different Re ($Ka = 181$, $l_b = 12$ mm $a_b = 1.6$ mm).

it is possible that we do not reach a low-enough Re for the oscillation to occur. An alternative that may help rule out this possibility, is to completely stop the inlet flow while performing measurements. Then, the liquid film gradually diminishes in size, and—if a pseudo steady-state approximation is made—the behaviour of small thicknesses is scanned. Of course, this approach is not rigorous, and in reality we observe the behaviour of a time-varying flow. Thus, it is only used as an additional check. A typical time signal with vanishing flow rate is shown in figure 7.11, in which case we knew that oscillation exists. Time series from three probes, which are placed respectively 36 mm, 240 mm and 456 mm from the onset of corrugation, are shown in the figure. The Re is initially at 0.9, and decreases after stopping the inlet flow. When $Re = 0.9$, weak oscillation can be observed at the downstream probe (probe 3), free surface at upstream and mid of channel is almost steady. After closing the inlet flow, a remarkable oscillation can be first observed in probe 3, and then, gradually moves upstream, shown in probe 2 and probe 1. In contrast, the time signal, under conditions for which

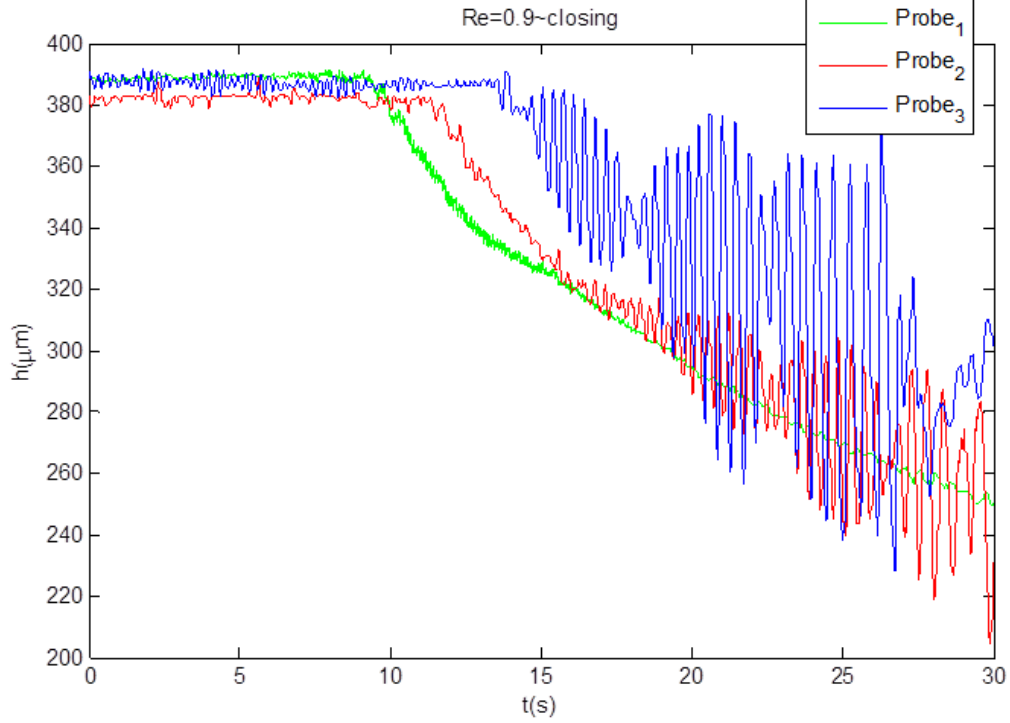


Figure 7.11: An example of time series with vanishing flow rate, which oscillation exists ($Ka=85$, $l_b=12$ mm $a_b=1.6$ mm).

no oscillation can be observed, is shown in figure 7.12. For both probes (one is placed upstream and the other is at downstream), the variation of free surface with vanishing Re is slow and smooth.

From the experiments that have been performed, the oscillations are found only on orthogonally corrugated walls, with two dimensions ($l_b=12$ mm, $a_b=1.6$ mm and $l_b=12$ mm, $a_b=2.0$ mm). We note though, that no experiment have been done at low Re for orthogonal walls with other dimensions. Therefore, whether the oscillation occurs at other steepness is still unknown. In case of sinusoidal corrugations ($l_b=12$ mm, $a_b=2.0$ mm), no oscillation is found in the experimental range (up to inclination angle of $\varphi=47^\circ$). The time series of film thickness over sinusoidal substrate at inclination angle, $\varphi=47^\circ$, is plotted in figure 7.13. The Re is decreasing from 2.11, and the plot indicates that no oscillatory phenomenon

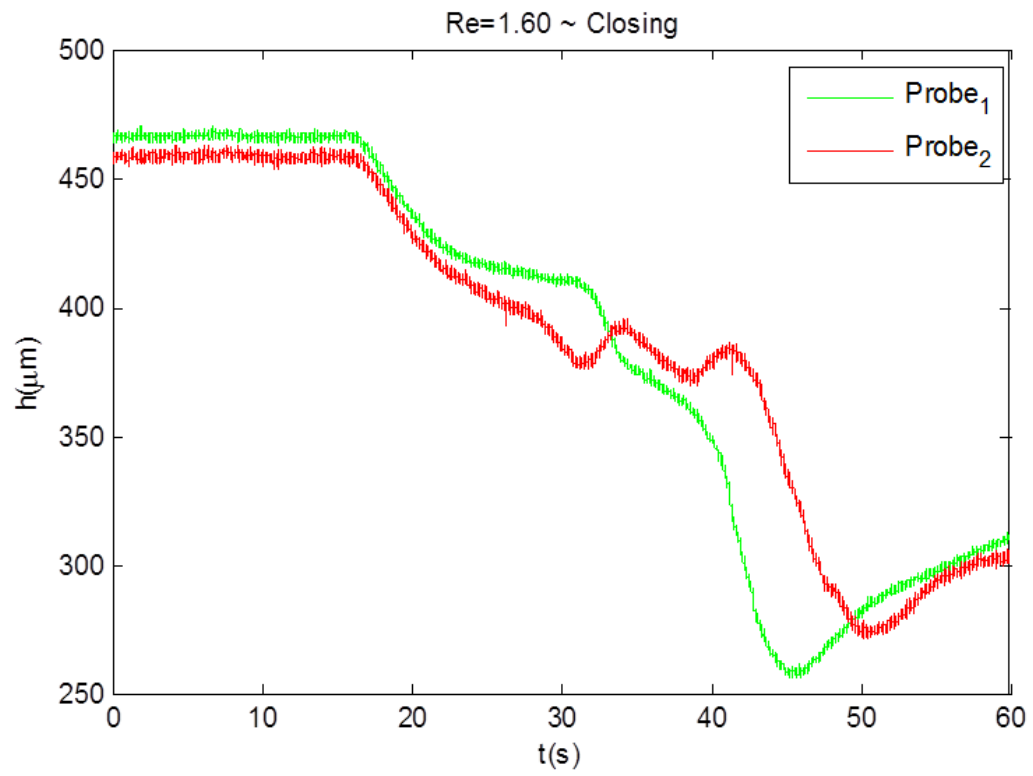


Figure 7.12: An example of time series with vanishing flow rate, which has no oscillation ($Ka=138$, $l_b=12$ mm $a_b=1.6$ mm).

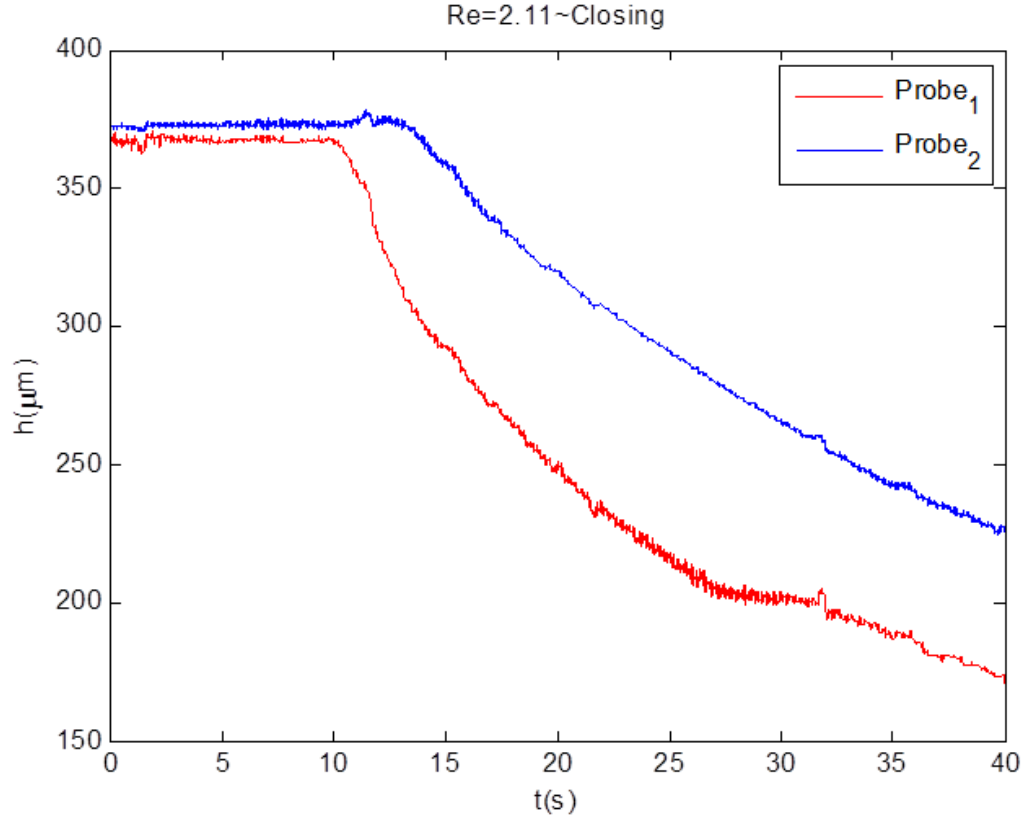


Figure 7.13: An example of time series with vanishing flow rate (Sinusoidal, $l_b = 12$ mm $a_b = 2.0$ mm).

occurs under this condition.

Different inclination angles are also tested: oscillation only occurs at high inclination angle, $\varphi \geq 40^\circ$; for lower inclinations, $\varphi \leq 35^\circ$, no oscillation is detected (inclination angle between 35° and 40° were not tested).

The liquid property (more specifically the viscosity, since the surface tension and density are roughly the same for small variation in glycerol concentration), has significant effect on the onset of the oscillatory phenomenon. In general, the oscillation will occur at lower Re the more viscous the liquid solution. In addition to figure 7.1, which corresponds to $Ka = 137$, time series of three different concentrations of aqueous glycerol solution is presented respectively in figure 7.14,

7.15 and 7.16. In the case of $Ka = 137$ (figure 7.1), the oscillation appears when the Re is below 2.20 (more evident at $Re = 1.80$); while for $Ka = 85$ (figure 7.15), evident oscillation can only be found when Re is below 1.04. For the very viscous solution ($Ka = 50$), oscillation starts to appear when Re is as low as 0.29, as shown in figure 7.16. This is significant lower than the theoretical long-wave prediction for a flat wall, $Re_{flat} = (5/6)cot\varphi = 0.833$, indicates a destabilizing effect.

Due to the multi-parameter nature, it is difficult to exhaust all the parameters. Thus, only fragmental experimental data are available. More experimental evidence and theoretical work are encouraged to investigate this problem.

7.4 Conclusion and discussion

This chapter reports on an unexpected oscillatory phenomenon that occurs at low Re , and is specific to orthogonal corrugation with high inclination angles (> 40 degrees). When decreasing the flow rate, the free surface, especially at the downstream of channel, deviates from its initial steady state and starts to oscillate, and this oscillation tends to be more significant at lower Re . The oscillation exhibits a synchronized mode with streamwise coherence, and can be characterized by its dominant frequency, which slightly increases with Re .

Generally, disturbances on film flow are considered convective, and film flows are supposed to be more stable with reducing the flow rate. However, the low- Re oscillation is sustainable and will not vanish even at very small Re . In the experimental range, the oscillation exists until film rupture occurs. Moreover, for viscous liquid ($Ka = 50$), the oscillation occurs at $Re = 0.29$, which is even lower than the theoretical long-wave prediction for a flat wall, indicating a destabilizing effect.

This counter-intuitive oscillatory phenomenon is believed to have a different mechanism. Huerre & Monkewitz (1985) have reported that inviscid mode of instability will be absolute type when the backflow velocity in an isolated free

7. An oscillatory behaviour at low Re

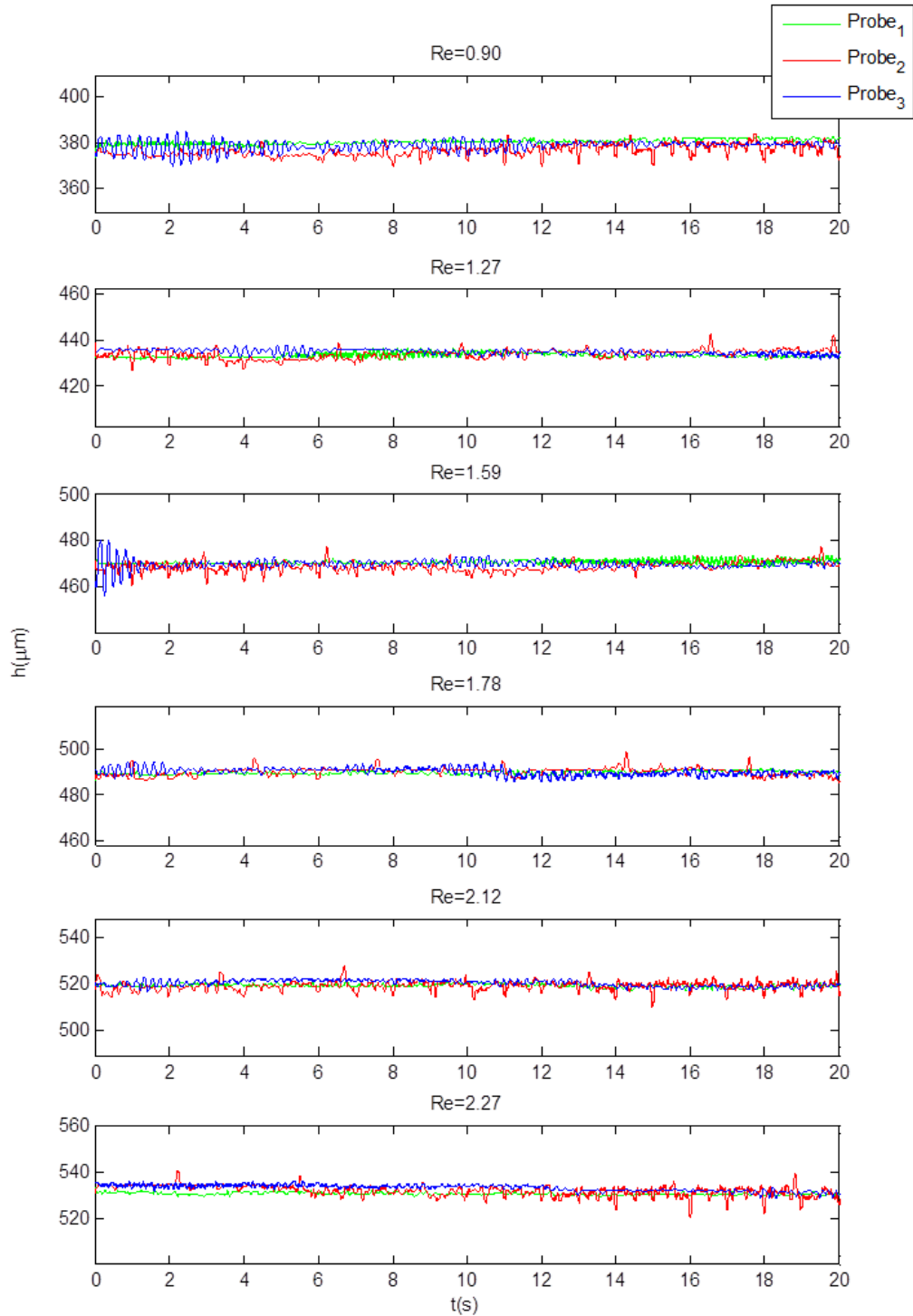


Figure 7.14: Time series of liquid height on an orthogonally corrugated wall ($l_b = 12 \text{ mm}$ $a_b = 1.6 \text{ mm}$) at $\varphi = 45^\circ$ ($Ka = 92$)

7. An oscillatory behaviour at low Re

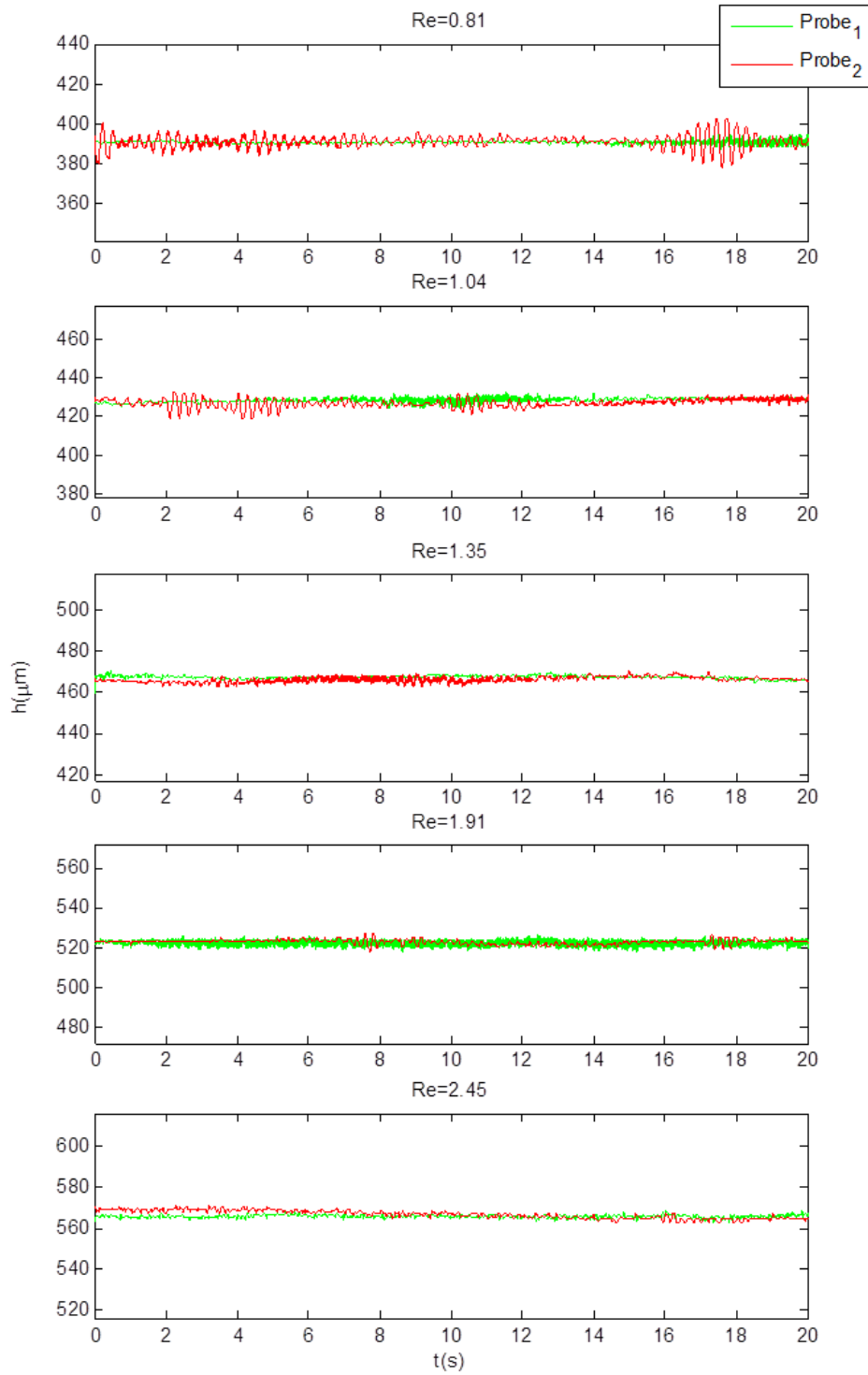


Figure 7.15: Time series of liquid height on an orthogonally corrugated wall ($l_b = 12 \text{ mm}$ $a_b = 1.6 \text{ mm}$) at $\varphi = 45^\circ$ ($Ka = 85$)

7. An oscillatory behaviour at low Re

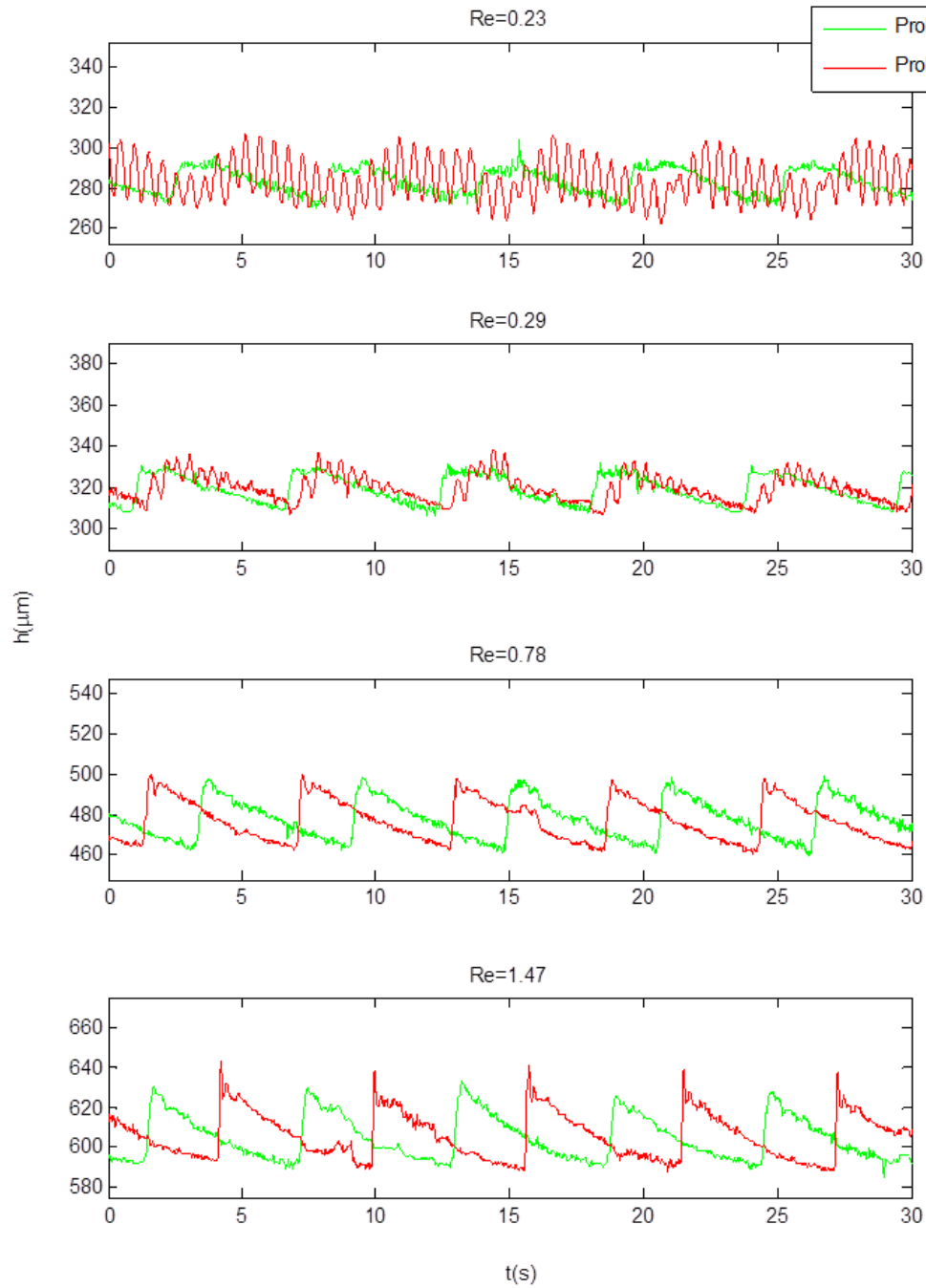


Figure 7.16: Time series of liquid height on an orthogonally corrugated wall ($l_b = 12 \text{ mm}$ $a_b = 1.6 \text{ mm}$) at $\varphi = 45^\circ$ ($Ka = 50$)

shear layer exceeds a specific value of the primary stream. A number of papers have indicated that a global instability may occur in the region where sufficient streamwise local absolute instability exists and cause streamwise synchronized oscillation. Hammond & Redekopp (1998) further suggested that intrinsic, global dynamics can be expected in flows with extensive separation if the peak back flow velocity exceeds approximately thirty percent of the ambient stream speed. This implies that strongly separated flows are likely to be globally unstable. The streamwise synchronized oscillation observed in the experiments seems to be close to a global unstable mode, which may be triggered by local absolute instabilities of the separated regions in the periodic corrugations. The fact that this phenomenon is only observed with the orthogonal wall at high inclinations (though separation also occurs with the sinusoidal wall, and may be more extensive at smaller inclinations), motivates further investigation of the role of the detailed characteristics of separation.

Chapter 8

Conclusions

8.1 Conclusion

The objective of the current study was to investigate experimentally the effect of wall corrugations on gravity-driven film flow, and in particular on the primary instability of the film. The experiments were performed in two experimental set-ups, an inclined film flow channel and a vertical cylindrical setup. A number of parameters was varied, including wall shape (sinusoidal and orthogonal), wall steepness, inclination angle and liquid viscosity. The main measuring technique employed involves conductance probes, and provides time-series of local thickness of the liquid film. Based on this technique, a method for determining the threshold of primary instability was developed and implemented. A photographic measurement technique was also developed, which is based on direct photography with normal illumination and black background, and on subsequent image processing to determine the exact location of the free surface. The photographic technique is complementary in that it provides the spatial variation of liquid film thickness.

The main conclusions of the work are the following:

(i) The most important finding is a new instability mode, which is different from the classical long-wave one. It is well known that film flow over flat substrate

will be first destabilized by disturbances with infinite wavelength. For film along periodically corrugated substrates, it is found that, with increasing inclination angles, an abrupt transition in the instability mode is manifested: the classical long-wave mode was replaced by a mode with finite wavelength, which is referred to as short-wave mode. The new mode is a traveling wave, which is highly regular and persistently two-dimensional. It has an intrinsic frequency insensitive to external excitation, and appears to be a global mode. The wavelength of the short-wave, which is determined by correlation of time signal at two locations along the channel, is found increasing with Re at the first stage of wave evolution. With increasing inclination angles, the onset wavelength is first shrinking and later remain roughly constant at high inclinations ($\varphi > 35^\circ$). The exact shape of the corrugations has a leading-order effect on the inclination on which the new mode appears and on its wavelength at inception.

(ii) Corrugated walls with various wavelengths and amplitudes were studied, in order to investigate the effect of the substrate geometry. As a result, detailed experimental data are presented, which report the critical Reynolds number for the primary threshold and determine the instability mode that occurs first. In the case of sinusoidal walls, the wavelength of the corrugation was varied by almost two orders of magnitude, and thus very different flow regimes were observed. In the case of orthogonal walls, wavelengths were of the same order, and the study focused on the effect of corrugation steepness. It was concluded in general that—with the possible exception of the case discussed in chapter 7—periodically corrugated substrates have a stabilizing effect.

(iii) It is natural to raise the question of how will film flow behave in the important special case of a vertical wall. To investigate this question, a cylindrical set-up was built and commissioned during the project, and measurements of the primary instability were taken for liquid flowing along the cylinder's outer surface. It was found that the first unstable mode is the short-wave one, and that its main characteristics (the critical Reynolds number and the wavelength at inception)

are comparable to those in a highly inclined channel ($\varphi > 35^\circ$). In particular, the existence of a finite (non-zero) critical Re confirms for the first time previous theoretical predictions (Trifonov, 2007).

(iv) Finally, an unexpected oscillatory instability is documented, specific to steep, orthogonal substrates, which appears and intensifies when decreasing the liquid flow rate. The oscillation exhibits a synchronized mode with streamwise coherence, and can be characterized by its dominant frequency, which slightly increases with Re . It is speculated that this counter-intuitive behaviour is related to the specific separation characteristics of the rectangular substrate, and is triggered when the backflow velocity exceeds a percentage of the forward stream.

8.2 Future work

The current work provide an experimental perspective of the effect of substrates on the film flow. The availability of a proper theoretical framework would be very useful in the efficient scrutinization of the effect of substrates with different geometric scales. From experimental point of view, some future work will also be recommended:

The intrinsic frequency and wavelength of the disturbances was determined only for one combination of height and wavelength with varying inclination angles. The effect of wall geometry on the onset wavelength is still unclear, and can be clarified by testing different wall corrugations.

Some preliminary results, varying the liquid viscosity, indicate the potentially important effect of liquid properties on the primary instability. This could be a potential direction for future investigation.

The instabilities investigated in the present work could be better understood if information of the flow field were also available. Thus, it is desirable to implement a PIV system from the side of the channel, and in this way conduct simultaneously a flow visualization study and a documentation of the spatial variation of the film

thickness. Such a technique could also be applied in the case of the cylindrical setup. Flow visualization would be further facilitated by the use of fluorescent particles.

Appendix A

Physical properties of aqueous glycerine solutions

Refractive Index of Glycerine-Water Solutions at 20° C (69° F)

Glycerine % by Weight	Refractive Index n_D^{20}	Difference for 1%	Glycerine % by Weight	Refractive Index n_D^{20}	Difference for 1%
100	1.47399	0.00165	50	1.39809	0.00149
99	1.47234	0.00163	49	1.39660	0.00147
98	1.47071	0.00161	48	1.39513	0.00145
97	1.46909	0.00157	47	1.39368	0.00141
96	1.46752	0.00156	46	1.39227	0.00138
95	1.46597	0.00154	45	1.39089	0.00136
94	1.46443	0.00153	44	1.38953	0.00135
93	1.46290	0.00151	43	1.38818	0.00135
92	1.46139	0.00150	42	1.38683	0.00135
91	1.45989	0.00150	41	1.38548	0.00135
90	1.45839	0.00150	40	1.38413	0.00135
89	1.45689	0.00150	39	1.38278	0.00135
88	1.45539	0.00150	38	1.38143	0.00135
87	1.45389	0.00152	37	1.38008	0.00134
86	1.45237	0.00152	36	1.37874	0.00134
85	1.45085	0.00155	35	1.37740	0.00134
84	1.44930	0.00156	34	1.37606	0.00134
83	1.44770	0.00160	33	1.37472	0.00134
82	1.44612	0.00162	32	1.37338	0.00134
81	1.44450	0.00160	31	1.37204	0.00134
80	1.44290	0.00155	30	1.37070	0.00134
79	1.44135	0.00153	29	1.36936	0.00134
78	1.43982	0.00150	28	1.36802	0.00133
77	1.43832	0.00149	27	1.36669	0.00133
76	1.43683	0.00149	26	1.36536	0.00132
75	1.43534	0.00149	25	1.36404	0.00132
74	1.43385	0.00149	24	1.36272	0.00131
73	1.43236	0.00149	23	1.36141	0.00131
72	1.43087	0.00149	22	1.36010	0.00131
71	1.42938	0.00149	21	1.35879	0.00130
70	1.42789	0.00149	20	1.35749	0.00130
69	1.42640	0.00149	19	1.35619	0.00129
68	1.42491	0.00149	18	1.35490	0.00129
67	1.42342	0.00149	17	1.35361	0.00128
66	1.42193	0.00149	16	1.35233	0.00127
65	1.42044	0.00149	15	1.35106	0.00126
64	1.41895	0.00149	14	1.34980	0.00126
63	1.41746	0.00149	13	1.34854	0.00125
62	1.41597	0.00149	12	1.34729	0.00125
61	1.41448	0.00149	11	1.34604	0.00123
60	1.41299	0.00149	10	1.34481	0.00122
59	1.41150	0.00149	9	1.34359	0.00121
58	1.41001	0.00149	8	1.34238	0.00120
57	1.40852	0.00149	7	1.34118	0.00119
56	1.40703	0.00149	6	1.33999	0.00119
55	1.40554	0.00149	5	1.33880	0.00118
54	1.40405	0.00149	4	1.33762	0.00117
53	1.40256	0.00149	3	1.33645	0.00115
52	1.40107	0.00149	2	1.33530	0.00114
51	1.39958	0.00149	1	1.33416	0.00113
			0	1.33303	—

Density of Glycerine-Water Solutions

Glycerine (%)	Density (g/cm ³)					Glycerine (%)	Density (g/cm ³)				
	15°C	15.5°C	20°C	25°C	30°C		15°C	15.5°C	20°C	25°C	30°C
100	1.26415	1.26381	1.26108	1.25802	1.25495	50	1.12870	1.12845	1.12630	1.12375	1.12110
99	1.26160	1.26125	1.25850	1.25545	1.25235	49	1.12600	1.12575	1.12360	1.12110	1.11845
98	1.25900	1.25865	1.25590	1.25290	1.24975	48	1.12325	1.12305	1.12090	1.11840	1.11580
97	1.25645	1.25610	1.25335	1.25030	1.24710	47	1.12055	1.12030	1.11820	1.11575	1.11320
96	1.25385	1.25350	1.25080	1.24770	1.24450	46	1.11780	1.11760	1.11550	1.11310	1.11055
95	1.25130	1.25095	1.24825	1.24515	1.24190	45	1.11510	1.11490	1.11280	1.11040	1.10795
94	1.24865	1.24830	1.24560	1.24250	1.23930	44	1.11235	1.11215	1.11010	1.10775	1.10530
93	1.24600	1.24565	1.24300	1.23985	1.23670	43	1.10960	1.10945	1.10740	1.10510	1.10265
92	1.24340	1.24305	1.24035	1.23725	1.23410	42	1.10690	1.10670	1.10470	1.10240	1.10005
91	1.24075	1.24040	1.23770	1.23460	1.23150	41	1.10415	1.10400	1.10200	1.09975	1.09740
90	1.23810	1.23775	1.23510	1.23200	1.22890	40	1.10145	1.10130	1.09930	1.09710	1.09475
89	1.23545	1.23510	1.23245	1.22935	1.22625	39	1.09875	1.09860	1.09665	1.09445	1.09215
88	1.23280	1.23245	1.22975	1.22665	1.22360	38	1.09605	1.09590	1.09400	1.09180	1.08955
87	1.23015	1.22980	1.22710	1.22400	1.22095	37	1.09340	1.09320	1.09135	1.08915	1.08690
86	1.22750	1.22710	1.22445	1.22135	1.21830	36	1.09070	1.09050	1.08865	1.08655	1.08430
85	1.22485	1.22445	1.22180	1.21870	1.21565	35	1.08800	1.08780	1.08600	1.08390	1.08165
84	1.22220	1.22180	1.21915	1.21605	1.21300	34	1.08530	1.08515	1.08335	1.08125	1.07905
83	1.21955	1.21915	1.21650	1.21340	1.21035	33	1.08265	1.08245	1.08070	1.07860	1.07645
82	1.21690	1.21650	1.21380	1.21075	1.20770	32	1.07995	1.07975	1.07800	1.07600	1.07380
81	1.21425	1.21385	1.21115	1.20810	1.20505	31	1.07725	1.07705	1.07535	1.07335	1.07120
80	1.21160	1.21120	1.20850	1.20545	1.20240	30	1.07455	1.07435	1.07270	1.07070	1.06855
79	1.20885	1.20845	1.20575	1.20275	1.19970	29	1.07195	1.07175	1.07010	1.06815	1.06605
78	1.20610	1.20570	1.20305	1.20005	1.19705	28	1.06935	1.06915	1.06755	1.06560	1.06355
77	1.20335	1.20300	1.20030	1.19735	1.19435	27	1.06670	1.06655	1.06495	1.06305	1.06105
76	1.20060	1.20025	1.19760	1.19465	1.19170	26	1.06410	1.06390	1.06240	1.06055	1.05855
75	1.19785	1.19750	1.19485	1.19195	1.18900	25	1.06150	1.06130	1.05980	1.05800	1.05605
74	1.19510	1.19480	1.19215	1.18925	1.18635	24	1.05885	1.05870	1.05720	1.05545	1.05350
73	1.19235	1.19205	1.18940	1.18650	1.18365	23	1.05625	1.05610	1.05465	1.05290	1.05100
72	1.18965	1.18930	1.18670	1.18380	1.18100	22	1.05365	1.05350	1.05205	1.05035	1.04850
71	1.18690	1.18655	1.18395	1.18110	1.17830	21	1.05100	1.05090	1.04950	1.04780	1.04600
70	1.18415	1.18385	1.18125	1.17840	1.17565	20	1.04840	1.04825	1.04690	1.04525	1.04350
69	1.18135	1.18105	1.17850	1.17565	1.17290	19	1.04590	1.04575	1.04440	1.04280	1.04105
68	1.17860	1.17830	1.17575	1.17295	1.17020	18	1.04335	1.04325	1.04195	1.04035	1.03860
67	1.17585	1.17555	1.17300	1.17020	1.16745	17	1.04085	1.04075	1.03945	1.03790	1.03615
66	1.17305	1.17275	1.17025	1.16745	1.16470	16	1.03835	1.03825	1.03695	1.03545	1.03370
65	1.17030	1.17000	1.16750	1.16475	1.16195	15	1.03580	1.03570	1.03450	1.03300	1.03130
64	1.16755	1.16725	1.16475	1.16200	1.15925	14	1.03330	1.03320	1.03200	1.03055	1.02885
63	1.16480	1.16445	1.16205	1.15925	1.15650	13	1.03080	1.03070	1.02955	1.02805	1.02640
62	1.16200	1.16170	1.15930	1.15655	1.15375	12	1.02830	1.02820	1.02705	1.02560	1.02395
61	1.15925	1.15895	1.15655	1.15380	1.15100	11	1.02575	1.02565	1.02455	1.02315	1.02150
60	1.15650	1.15615	1.15380	1.15105	1.14830	10	1.02325	1.02315	1.02210	1.02070	1.01905
59	1.15370	1.15340	1.15105	1.14835	1.14555	9	1.02085	1.02075	1.01970	1.01835	1.01670
58	1.15095	1.15065	1.14830	1.14560	1.14285	8	1.01840	1.01835	1.01730	1.01600	1.01440
57	1.14815	1.14785	1.14555	1.14285	1.14010	7	1.01600	1.01590	1.01495	1.01360	1.01205
56	1.14535	1.14510	1.14280	1.14015	1.13740	6	1.01360	1.01350	1.01255	1.01125	1.00970
55	1.14260	1.14230	1.14005	1.13740	1.13470	5	1.01120	1.01110	1.01015	1.00890	1.00735
54	1.13980	1.13955	1.13730	1.13465	1.13195	4	1.00875	1.00870	1.00780	1.00655	1.00505
53	1.13705	1.13680	1.13455	1.13195	1.12925	3	1.00635	1.00630	1.00540	1.00415	1.00270
52	1.13425	1.13400	1.13180	1.12920	1.12650	2	1.00395	1.00385	1.00300	1.00180	1.00035
51	1.13150	1.13125	1.12905	1.12650	1.12380	1	1.00155	1.00145	1.00060	0.99945	0.99800
						0	0.99913	0.99905	0.99823	0.99708	0.99568

Viscosity of Aqueous Glycerine Solutions in Centipoises/mPa s

Glycerine percent weight	Temperatur e (°C)										
	0	10	20	30	40	50	60	70	80	90	100
0 ⁽¹⁾	1.792	1.308	1.005	0.8007	0.6560	0.5494	0.4688	0.4061	0.3565	0.3165	0.2838
10	2.44	1.74	1.31	1.03	0.826	0.680	0.575	0.500	–	–	–
20	3.44	2.41	1.76	1.35	1.07	0.879	0.731	0.635	–	–	–
30	5.14	3.49	2.50	1.87	1.46	1.16	0.956	0.816	0.690	–	–
40	8.25	5.37	3.72	2.72	2.07	1.62	1.30	1.09	0.918	0.763	0.668
50	14.6	9.01	6.00	4.21	3.10	2.37	1.86	1.53	1.25	1.05	0.910
60	29.9	17.4	10.8	7.19	5.08	3.76	2.85	2.29	1.84	1.52	1.28
65	45.7	25.3	15.2	9.85	6.80	4.89	3.66	2.91	2.28	1.86	1.55
67	55.5	29.9	17.7	11.3	7.73	5.50	4.09	3.23	2.50	2.03	1.68
70	76	38.8	22.5	14.1	9.40	6.61	4.86	3.78	2.90	2.34	1.93
75	132	65.2	35.5	21.2	13.6	9.25	6.61	5.01	3.80	3.00	2.43
80	255	116	60.1	33.9	20.8	13.6	9.42	6.94	5.13	4.03	3.18
85	540	223	109	58	33.5	21.2	14.2	10.0	7.28	5.52	4.24
90	1310	498	219	109	60.0	35.5	22.5	15.5	11.0	7.93	6.00
91	1590	592	259	127	68.1	39.8	25.1	17.1	11.9	8.62	6.40
92	1950	729	310	147	78.3	44.8	28.0	19.0	13.1	9.46	6.82
93	2400	860	367	172	89	51.5	31.6	21.2	14.4	10.3	7.54
94	2930	1040	437	202	105	58.4	35.4	23.6	15.8	11.2	8.19
95	3690	1270	523	237	121	67.0	39.9	26.4	17.5	12.4	9.08
96	4600	1580	624	281	142	77.8	45.4	29.7	19.6	13.6	10.1
97	5770	1950	765	340	166	88.9	51.9	33.6	21.9	15.1	10.9
98	7370	2460	939	409	196	104	59.8	38.5	24.8	17.0	12.2
99	9420	3090	1150	500	235	122	69.1	43.6	27.8	19.0	13.3
100	12070	3900	1410	612	284	142	81.3	50.6	31.9	21.3	14.8

⁽¹⁾Viscosity of water taken from "Properties of Ordinary Water-Substance." N.E. Dorsey, p. 184. New York (1940)

Appendix B

List of conditions of experiment runs in Chapter 5

Table 1: Experimental conditions of film over sinusoidal corrugations

No.	Shape	l_b (mm)	a_b (mm)	Inclination ($^{\circ}$)	ρ (kg/m^3)	ν (mm^2/s)	σ ($N \times$ m^{-1})
1	Sinusoidal	50	10	7	1169	9.90	0.067
2	Sinusoidal	50	10	15	1169	9.90	0.067
3	Sinusoidal	50	10	25	1169	10.16	0.067
4	Sinusoidal	50	10	35	1169	10.16	0.067
5	Sinusoidal	2	1	7	1176	10.52	0.067
6	Sinusoidal	2	1	15	1168	9.29	0.067
7	Sinusoidal	2	1	25	1177	12.90	0.067
8	Sinusoidal	2	1	35	1177	12.90	0.067
9	Sinusoidal	12	2	4	1170	9.36	0.067
10	Sinusoidal	12	2	5	1170	10.25	0.067
11	Sinusoidal	12	2	7	1177	10.94	0.067
12	Sinusoidal	12	2	10	1170	10.73	0.067
13	Sinusoidal	12	2	15	1170	10.73	0.067
14	Sinusoidal	12	2	20	1170	11.05	0.067
15	Sinusoidal	12	2	25	1170	10.99	0.067
16	Sinusoidal	12	2	30	1170	10.67	0.067
17	Sinusoidal	12	2	35	1172	10.53	0.067
18	Sinusoidal	12	2	40	1172	10.95	0.067
19	Sinusoidal	12	2	45	1172	10.95	0.067

Table 2: Experimental conditions of film over orthogonal corrugations							
No.	Shape	l_b (mm)	a_b (mm)	Inclination ($^{\circ}$)	ρ (kg/m^3)	ν (mm^2/s)	σ ($N \times m^{-1}$)
1	Orthogonal	24	0.8	3	1193.2	9.30	0.067
2	Orthogonal	24	0.8	37	1193.2	9.30	0.067
3	Orthogonal	24	0.8	10	1193.2	9.35	0.067
4	Orthogonal	24	0.8	15	1193.2	9.60	0.067
5	Orthogonal	24	0.8	20	1193.2	9.60	0.067
6	Orthogonal	24	0.8	25	1193.2	9.60	0.067
7	Orthogonal	24	0.8	30	1193.2	9.50	0.067
8	Orthogonal	24	0.8	35	1193.2	9.50	0.067
9	Orthogonal	24	0.8	3	1193.2	9.31	0.067
10	Orthogonal	24	0.8	7	1193.2	9.31	0.067
11	Orthogonal	24	0.8	10	1193.2	9.58	0.067
12	Orthogonal	24	0.8	15	1193.2	9.58	0.067
13	Orthogonal	24	0.8	20	1193.2	9.92	0.067
14	Orthogonal	24	0.8	25	1193.2	9.57	0.067
15	Orthogonal	24	0.8	30	1193.2	9.57	0.067
16	Orthogonal	24	0.8	35	1193.2	9.09	0.067
17	Orthogonal	24	0.8	40	1193.2	11.70	0.067
18	Orthogonal	24	0.8	45	1193.2	11.70	0.067
19	Orthogonal	12	1.6	3	1153.8	9.36	0.067
20	Orthogonal	12	1.6	7	1153.8	9.36	0.067
21	Orthogonal	12	1.6	10	1189.5	9.00	0.067
22	Orthogonal	12	1.6	15	1153.8	9.36	0.067
23	Orthogonal	12	1.6	20	1189.5	9.13	0.067
24	Orthogonal	12	1.6	25	1189.5	9.10	0.067
25	Orthogonal	12	1.6	30	1189.0	8.80	0.067
26	Orthogonal	12	1.6	35	1189.5	9.13	0.067
27	Orthogonal	12	1.6	40	1189.7	9.13	0.067
28	Orthogonal	12	2	3	1151.4	8.00	0.067
29	Orthogonal	12	2	7	1151.4	8.00	0.067
30	Orthogonal	12	2	10	1189.5	9.00	0.067
31	Orthogonal	12	2	15	1151.5	8.10	0.067
32	Orthogonal	12	2	20	1189.5	9.10	0.067
33	Orthogonal	12	2	25	1189.0	9.00	0.067
34	Orthogonal	12	2	30	1189.0	9.00	0.067
35	Orthogonal	12	2	35	1189.5	9.13	0.067
36	Orthogonal	12	2	40	1189.5	9.13	0.067
37	Orthogonal	12	2	45	1189.5	9.13	0.067

References

- ALEKSEENKO, S.V., NAKORYAKOV, V.E. & POKUSAEV, B.G. (1994). *Wave flow of liquid films*. Begell house, New York. 28, 30, 42
- ANSHUS, B.E. & GOREN, S.L. (1966). A method of getting approximate solutions to the orr-sommerfeld equation for flow on a vertical wall. *AIChE J.*, **12**, 1004–1008. 12
- ARGYRIADI, K., VLACHOGIANNIS, M. & BONTOZOGLOU, V. (2006). Experimental study of inclined film flow along periodic corrugations: The effect of wall steepness. *Phys. Fluids*, **18**, 012102. xiii, 2, 23, 52, 74, 85
- BENJAMIN, T. (1957). Wave formation in laminar flow down an inclined plane. *J. Fluid Mech.*, **2**, 554–573. 12
- BENJAMIN, T. (1961). The development of three-dimensional disturbances in an unstable film of liquid flowing down an inclined plane. *J. Fluid Mech.*, **10**, 401–419. 15
- BENNEY, D.J. (1966). Wave formation in laminar flow down an inclined plane. *J. Math. Phys.*, **45**, 150–155. 13, 15
- BONTOZOGLOU, V. (2000). Laminar film flow along a periodic wall. *Comp. Model. Engng*, **1**, 133–142. 19

REFERENCES

- BONTOZOGLOU, V. & PAPAPOLYMEROU, G. (1997). Laminar film flow down a wavy incline. *Intl J. Multiphase Flow*, **23**, 69 – 79. xii, 18, 19, 22, 52, 77
- BONTOZOGLOU, V. & SERIFI, K. (2008). Falling film flow along steep two-dimensional topography: The effect of inertia. *Intl J. Multiphase Flow*, **34**, 734 – 747. 2
- BREVDO, L., LAURE, P., DIAS, F. & BRIDGES, T.J. (1999). Linear pulse structure and signalling in a film flow on an inclined plane. *J. Fluid Mech.*, **396**, 37–71. 56
- BRIGGS, R.J. (1964). Electron-stream interaction with plasmas. M.I.T. Press. 14
- BROWN, R.C., ANDREUSSI, P. & ZANELLI, S. (1978). The use of wire probes for the measurement of liquid thickness in annular gas-liquid flows. *Can. J. Chem. Eng.*, **15**, 1–21. 31
- CAO, Z., VLACHOGIANNIS, M. & BONTOZOGLOU, V. (2013). Experimental evidence for a short-wave global mode in film flow along periodic corrugations. *J. Fluid Mech.*, **718**, 304–320. 54
- CHANG, H.C. (1994). Wave evolution on a falling film. *Annu. Rev. Fluid Mech.*, **26**, 103–136. xii, 8, 9
- CHANG, H.C. & DEMEKHIN, E.A. (2002). Complex wave dynamics on thin films. Elsevier, Amsterdam. 1
- CHIN, R.W., ABERHATHY, F.F. & BERTSCHY, J.R. (1986). Gravity and shear wave stability of free surface flows. part 1. numerical calculations. *J. Fluid Mech.*, **168**, 501–513. 12
- CHOUDHARI, M. (1993). Boundary-layer receptivity due to distributed surface imperfections of a deterministic or random nature. *Theoret. Comput. Fluid Dyn.*, **4**, 101–117. 75

REFERENCES

- CLARK, W.W. (2002). Liquid film thickness measurement. *Multiphase Science and Technology*, **14**, 1–74. 28
- CONEY, M.W.E. (1973). The theory and application of conductance probes for the measurement of liquid film thickness in two-phase flow. *J. Phys. E: Sci. Instrum.*, **6**, 903. 41
- CRASTER, R.V. & MATAR, O.K. (2009). Dynamics and stability of thin liquid films. *Rev. Mod. Phys.*, **81**, 1131–1198. 1
- D’ALESSIO, S.J.D., PASCAL, J.P. & JASMINE, H.A. (2009). Instability in gravity-driven flow over uneven surfaces. *Phys. Fluids*, **21**, 062105. xiii, 2, 25, 26, 69
- DASSORI, C.G., DEIBER, J.A. & CASSANO, A.E. (1984). Slow two-phase flow through a sinusoidal channel. *Intl J. Multiphase Flow*, **10**, 181 – 193. 17
- DÁVALOS-OROZCO, L.A. (2007). Nonlinear instability of a thin film flowing down a smoothly deformed surface. *Phys. Fluids*, **19**, 074103. 2, 21, 24
- DAVIES, A.G. & HEATHERSHAW, A.D. (1984). Surface-wave propagation over sinusoidally varying topography. *J. Fluid Mech.*, **144**, 419–443. 75
- DE SANTOS, J.M., MELLI, T.R. & SCRIVEN, L.E. (1991). Mechanics of gas-liquid flow in packed-bed contactors. *Annu. Rev. Fluid Mech.*, **23**, 233–260. 1
- DESEVAUX, P., HOMESCU, D., PANDAY, P.K. & PRENEL, J.P. (2002). Interface measurement technique for liquid film flowing inside small grooves by laser induced fluorescence. *Appl. Therm. Eng.*, **22**, 521–534. 33
- DUPRAT, C., RUYER-QUIL, C., KALLIADASIS, S. & GIORGIUTTI-DAUPHINÉ, F. (2007). Absolute and convective instabilities of a viscous film flowing down a vertical fiber. *Phys. Rev. Lett.*, **98**, 244502. 64

REFERENCES

- FOSSA, M. (1998). Design and performance of a conductance probe for measuring the liquid fraction in two-phase gas-liquid flows. *Flow Meas. Instrum.*, **9**, 103–109. 31
- GASKELL, P.H., JIMACK, P.K., SELLIER, M., THOMPSON, H.M. & WILSON, M.C.T. (2004). Gravity-driven flow of continuous thin liquid films on non-porous substrates with topography. *J. Fluid Mech.*, **509**, 253–280. 2
- GEORGANTAKI, A., VATTEVILLE, J., VLACHOGIANNIS, M. & BONTOZOGLOU, V. (2011). Measurements of liquid film flow as a function of fluid properties and channel width: Evidence for surface-tension-induced long-range transverse coherence. *Phys. Rev. E*, **84**, 026325. 13, 53, 80, 84
- GJEVIK, B. (1970). Occurrence of finite-amplitude surface waves on falling liquid films. *Phys. Fluids*, **13**, 1918–1925. 13
- HÄCKER, T. & UECKER, H. (2009). An integral boundary layer equation for film flow over inclined wavy bottoms. *Phys. Fluids*, **21**, 092105. xiii, 2, 27, 28, 69
- HAMMOND, D.A. & REDEKOPP, L.G. (1998). Local and global instability properties of separation bubbles. *Eur. J. Mech., B/Fluids*, **17**, 145–164. 131
- HEINING, C. & AKSEL, N. (2009). Bottom reconstruction in thin-film flow over topography: Steady solution and linear stability. *Phys. Fluids*, **21**, 083605. xiii, 26, 27
- HELBIG, K., NASAREK, R., GAMBARYAN-ROISMAN, T. & STEPHAN, P. (2009). Effect of longitudinal minigrooves on flow stability and wave characteristics of falling liquid films. *J. Heat Transfer*, **131**, 011601. 1
- HEWITT, G.F. (1978). Measurement of two phase flow parameters. Academic. 28

REFERENCES

- HEWITT, G.F. (1982). Liquid gas systems. In G. Hetsroni, ed., *In Handbook of multiphase systems*, 2-3 – 2-136, McGraw-Hill Book Co. 30
- HIDROVO, C.H. & HART, D.P. (2001). Emission reabsorption laser induced fluorescence (erlif) film thickness measurement. *Meas. Sci. Technol.*, **12**, 467–477. 33
- HUERRE, P. & MONKEWITZ, P.A. (1985). Absolute and convective instabilities in free shear layers. *J. Fluid Mech.*, **159**, 151–168. 14, 127
- HUERRE, P. & MONKEWITZ, P.A. (1990). Local and global instabilities in spatially developing flows. *Annu. Rev. Fluid Mech.*, **22**, 473–537. 64
- ISHIGAI, S., NAKANISI, S., KOIZUMI, T. & OYABU, Z. (1972). Hydrodynamics and heat transfer of vertical falling liquid films : Part 1, classification of flow regimes. *Bulletin of JSME*, **15**, 594–602. 30
- JOO, S.W. & DAVIS, S.H. (1992). Instabilities of three-dimensional viscous falling films. *J. Fluid Mech.*, **242**, 529–547. 15
- KALLIADASIS, S. & HOMSY, G.M. (2001). Stability of free-surface thin-film flows over topography. *J. Fluid Mech.*, **448**, 387–410. 2
- KALLIADASIS, S., RUYER-QUIL, C., SCHEID, B. & VELARDE, M. (2012). *Falling liquid films*, vol. 176 of *Applied Mathematical Sciences*. Springer, London. xii, 15
- KANG, F. & CHEN, K. (1995). Gravity-driven two-layer flow down a slightly wavy periodic incline at low reynolds numbers. *Intl J. Multiphase Flow*, **21**, 501 – 513. 17
- KANG, H.C. & KIM, M.H. (1992). The development of a flush wire probes and calibration method for measuring liquid film thickness. *Intl J. Multiphase Flow*, **18**, 423–437. xiv, 31, 41, 42

REFERENCES

- KELLY, R.E., GOUSSIS, D.A., LIN, S.P. & HSU, F.K. (1989). The mechanism for surface wave instability in film flow down an inclined plane. *Phys. Fluids*, **1**, 819–828. 16
- KIM, J., AHN, Y.C. & KIM, M.H. (2009). Measurement of void fraction and bubble speed of slug flow with three-ring conductance probes. *Flow Meas. Instrum.*, **20**, 103–109. 31
- KOSKIE, J.E., MUDAWAR, I. & TIEDERMAN, W.G. (1989). Parallel-wire probes for measurement of thick liquid films. *Int. J. Multiphase Flow*, **15**, 521–530. 41
- KRANTZ, W.B. & GOREN, S.L. (1971). Stability of thin liquid films flowing down a plane. *Ind. Engng Chem. Fundam.*, **10**, 91–101. 12
- LIN, S.P. (1969). Finite-amplitude stability of a parallel flow with a free surface. *J. Fluid Mech.*, **36**, 113–126. 13
- LIU, J. & GOLLUB, J.P. (1994). Solitary wave dynamics of film flows. *Phys. Fluids*, **6**, 1702–1712. 14
- LIU, J., PAUL, E., J. D. AND BANILOWER & GOLLUB, J.P. (1992). Film flows instabilities and spatiotemporal dynamics. 225–239. 15
- LIU, J., PAUL, J.D. & GOLLUB, J.P. (1993). Measurements of the primary instabilities of film flows. *J. Fluid Mech.*, **250**, 69–101. 12, 15, 32, 44, 56
- LUO, H. & POZRIKIDIS, C. (2006). Effect of inertia on film flow over oblique and three-dimensional corrugations. *Phys. Fluids*, **18**, 078107. 19
- MUDUNURI, R.R. & BALAKOTAIAH, V. (2006). Solitary waves on thin falling films in the very low forcing frequency limit. *AIChE J.*, **52**, 3995–4003. 14
- NAKAYA, C. (1975). Long waves on a thin fluid layer flowing down an inclined plane. *Phys. Fluids*, **18**, 1407–1420. 13

REFERENCES

- NEGNY, S., MEYER, M. & PREVOST, M. (2001). Study of a laminar falling film flowing over a wavy wall column: Part II. experimental validation of hydrodynamic model. *Int. J. Heat Mass Transfer*, **44**, 2147–2154. 35, 48
- NGUYEN, C.C. & PLOURDE, F. (2011). Wavy wall influence on the hydrodynamic instability of a liquid film flowing along an inclined plane. *Intl J. Heat and Fluid Flow*, **32**, 698 – 707. 27
- NGUYEN, P.K. & BONTZOGLIOU, V. (2011). Steady solutions of inertial film flow along strongly undulated substrates. *Phys. Fluids*, **23**, 052103. 16, 19, 52, 74
- NOSOKO, T., YOSHIMURA, P., NAGATA, T. & OYAKAWA, K. (1996). Characteristics of two-dimensional waves on a falling liquid film. *Chem. Eng. Sci.*, **51**, 725 – 732. 30
- NUSSELT, W. (1916). Die oberflächen kondensation des wasserdampes. *Ver. Deut. Ing.*, **60**, 541–546. 10
- ORON, A. & GOTTLIEB, O. (2002). Nonlinear dynamics of temporally excited falling liquid films. *Phys. Fluids*, **14**, 2622–2636. 13
- ORON, A. & HEINING, C. (2008). Weighted-residual integral boundary-layer model for the nonlinear dynamics of thin liquid films falling on an undulating vertical wall. *Phys. Fluids*, **20**, 082102. 2, 24, 71
- ORON, A., DAVIS, S.H. & BANKOFF, S.G. (1997). Long-scale evolution of thin liquid films. *Rev. Mod. Phys.*, **69**, 931–980. 1
- ORON, A., GOTTLIEB, O. & NOVBARI, E. (2009). Numerical analysis of a weighted-residual integral boundary-layer model for nonlinear dynamics of falling liquid films. *Eur. J. Mech. B/Fluids*, **28**, 1–36. 14

REFERENCES

- PARK, C.D. & NOSOKO, T. (2003). Three-dimensional wave dynamics on a falling film and associated mass transfer. *AIChE Journal*, **49**, 2715–2727. xii, 7, 8
- PIERSON, F.W. & WHITAKER, S. (1977). Some theoretical and experimental observations of the wave structure of falling liquid films. *Ind. Engng Chem. Fundam.*, **16**, 401–408. 12
- POLLAK, T., HAAS, A. & AKSEL, N. (2011). Side wall effects on the instability of thin gravity-driven films—from long-wave to short-wave instability. *Phys. Fluids*, **23**, 094110. 13, 44
- POZRIKIDIS, C. (1988). The flow of a liquid film along a periodic wall. *J. Fluid Mech.*, **188**, 275–300. 17
- POZRIKIDIS, C. (2003). Effect of surfactants on film flow down a periodic wall. *J. Fluid Mech.*, **496**, 105–127. 21
- PRÄSSER, H.M., BOTTFER, A. & ZSCHAU, J. (1998). A new electrode-mesh tomograph for gas-liquid flows. *Flow Meas. Instrum.*, **9**, 111–119. 31
- PUMIR, A., MANNEVILLE, P. & POMEAU, Y. (1983). On solitary waves running down an inclined plane. *J. Fluid Mech.*, **135**, 27–50. 13
- QUÉRÉ, D. (1999). Fluid coating on a fiber. *Annu. Rev. Fluid Mech.*, **31**, 347–384. 1
- RAJAGOPALAN, S., ZHOU, T. & ANTONIA, R. (1998). Three-component turbulence measurements using a four-wire probe. *Flow Meas. Instrum.*, **9**, 211–216. 31
- RAMASWAMY, B., CHIPPA, S. & JOO, S. (1996). A full-scale numerical study of interfacial instabilities in thin-film flows. *J. Fluid Mech.*, **325**, 163–194. 14

REFERENCES

- ROSENAU, P., ORON, A. & HYMAN, J.M. (1992). Bounded and unbounded patterns of the benney equation. *Phys. Fluids A*, **4**, 1102–1104. 13
- RUBAN, A.I. (1984). On the generation of tollmien-schlichting waves by sound. *Fluid Dyn*, **19**, 709–717. 75
- BUYER-QUIL, C. & MANNEVILLE, P. (2000). Improved modeling of flows down inclined planes. *Eur. Phys. J. B*, **15**, 357–369. 13, 24
- BUYER-QUIL, C. & MANNEVILLE, P. (2002). Further accuracy and convergence results on the modeling of flows down inclined planes by weighted-residual approximations. *Phys. Fluids*, **14**, 170–183. 13
- SCHEID, B., BUYER-QUIL, C., THIELE, U., KABOV, O.A., LEGROS, J.C. & COLINET, P. (2005). Validity domain of the benney equation including the marangoni effect for closed and open flows. *J. Fluid Mech.*, **527**, 303–335. 13, 14
- SCHOLLE, M., WIERSCHEM, A. & AKSEL, N. (2004). Creeping films with vortices over strongly undulated bottoms. *Acta Mechanica*, **168**, 167–193. 19
- SCHOLLE, M., HAAS, A., AKSEL, N., WILSON, M.C.T., THOMPSON, H.M. & GASKELL, P.H. (2008). Competing geometric and inertial effects on local flow structure in thick gravity-driven fluid films. *Phys. Fluids*, **20**, 123101. 19
- SCHUBRING, D., ASHWOOD, A., SHEDD, T. & HURLBURT, E. (2010). Planar laser-induced fluorescence (plif) measurements of liquid film thickness in annular flow. part i: Methods and data. *Intl J. Multiphase Flow*, **36**, 815 – 824. xiii, 33, 34
- SHETTY, S. & CERRO, R.L. (1993). Flow of a thin film over a periodic surface. *Intl J. Multiphase Flow*, **19**, 1013 – 1027. 17

REFERENCES

- SHKADOV, V.Y. (1967). Wave flow regimes of a thin layer of a viscous fluid subject to gravity. *Izv. Akad. Nauk. SSSR, Mekh. Zhid. Gaza*, **No. 1**, 43–51. (English translation: *Fluid Dyn.* 2, 29–34.). 13
- SMITH, M.K. (1990). The mechanism for the long-wave instability in thin liquid films. *J. Fluid Mech.*, **217**, 469–485. 16
- TAKAHAMA, H. & KATO, S. (1980). Longitudinal flow characteristics of vertically falling liquid films without concurrent gas flow. *Intl J. Multiphase Flow*, **6**, 203 – 215. 30
- TRIFONOV, Y.Y. (1998). Viscous liquid film flow over a vertical corrugated surface and waves formation on the film free surface. In *Third Intl Conf. on Multiphase Flow*, Lyon, France. 22, 77
- TRIFONOV, Y.Y. (1999). Viscous liquid film flows over a periodic surface. *Intl J. Multiphase Flow*, **24**, 1139 – 1161. 19, 52
- TRIFONOV, Y.Y. (2007). Stability of a viscous liquid film flowing down a periodic surface. *Intl J. Multiphase Flow*, **33**, 1186 – 1204. 2, 16, 24, 52, 71, 74, 96, 111, 134
- TSELUIKO, D. & BLYTH, M. (2009). Effect of inertia on electrified film flow over a wavy wall. *J. Eng. Math.*, **65**, 229–242. 21
- TSELUIKO, D., BLYTH, M.G., PAPAGEORGIOU, D.T. & VANDEN-BROECK, J.M. (2008). Effect of an electric field on film flow down a corrugated wall at zero reynolds number. *Phys. Fluids*, **20**, 042103. 21
- VALLURI, P., MATAR, O.K., HEWITT, G.F. & MENDES, M. (2005). Thin film flow over structured packings at moderate reynolds numbers. *Chem. Eng. Sci.*, **60**, 1965 – 1975. 1

REFERENCES

- VLACHOGIANNIS, M. & BONTOZOGLOU, V. (2001). Observations of solitary wave dynamics of film flows. *J. Fluid Mech.*, **435**, 191–215. 32
- VLACHOGIANNIS, M. & BONTOZOGLOU, V. (2002). Experiments on laminar film flow along a periodic wall. *J. Fluid Mech.*, **457**, 133–156. xiii, 2, 19, 21, 22, 32, 33, 52, 74, 85
- VLACHOGIANNIS, M., SAMANDAS, A., LEONTIDIS, V. & BONTOZOGLOU, V. (2010). Effect of channel width on the primary instability of inclined film flow. *Phys. Fluids*, **22**, 012106. 12, 43, 45, 47, 56
- WANG, C.Y. (1981). Liquid film flowing slowly down a wavy incline. *AIChE Journal*, **27**, 207–212. 17
- WEINSTEIN, S.J. & RUSCHAK, K.J. (2004). Coating flows. *Annu. Rev. Fluid Mech.*, **36**, 29–53. 1
- WHITAKER, S. (1964). Effect of surface active agents on stability of falling liquid films. *Ind. Engng Chem. Fundam.*, **3**, 132–142. 12
- WIERSCHEM, A. & AKSEL, N. (2004). Influence of inertia on eddies created in films creeping over strongly undulated substrates. *Phys. Fluids*, **16**, 4566–4574. 19, 74, 85
- WIERSCHEM, A., SCHOLLE, M. & AKSEL, N. (2002). Comparison of different theoretical approaches to experiments on film flow down an inclined wavy channel. *Exp. Fluids*, **33**, 429–442. xiii, 35
- WIERSCHEM, A., SCHOLLE, M. & AKSEL, N. (2003). Vortices in film flow over strongly undulated bottom profiles at low reynolds numbers. *Phys. Fluids*, **15**, 426–435. 19, 22, 35
- WIERSCHEM, A., LEPSKI, C. & AKSEL, N. (2005). Effect of long undulated bottoms on thin gravity-driven films. *Acta Mech.*, **179**, 41–66. xiii, xvi, 22, 44, 52, 71

REFERENCES

- WIERSCHEM, A., BONTOZOGLOU, V., HEINING, C., UECKER, H. & AKSEL, N. (2008). Linear resonance in viscous films on inclined wavy planes. *Intl J. Multiphase Flow*, **34**, 580 – 589. 19
- WIERSCHEM, A., POLLAK, T., HEINING, C. & AKSEL, N. (2010). Suppression of eddies in films over topography. *Phys. Fluids*, **22**, 113603. xii, 20
- YIH, C. (1963). Stability of liquid flow down an inclined plane. *Phys. Fluids*, **6**, 321–330. 12
- YIH, C. (1967). Instability due to viscosity stratification. *J. Fluid Mech.*, **27**, 337–352. 12
- ZIOULIS, A. (2011). *Measurements of liquid film flow in a vertical cylindrical wavy wall*. diploma thesis, University of Thessaly. xviii, 97